Process-based morphological and hydrological modelling of a glacially sculptured tidal inlet system, Vestvågøy, Lofoten

Nil Sarper

Master of Science Thesis

Department of Earth Science

University of Bergen

October 2021

Abstract

This thesis investigates the decadal-scale morphological developments of a glacially sculptured tidal inlet system at the Lofoten archipelago in Norway. The tidal inlet system consists of three interconnected basins with small and shallow tidal inlets that allow seawater to enter the basins. The most seaward basin is connected to the sea with two channels. The easterly channel is closed off by man-made barriers. The question is what happens with the morphology and tides if those barriers are removed. The grain size analysis reveals that the study area consists of fine sand around the channels (inlets). Further, water level measurements show that tidal choking is the dominant process in the system. For example, at present, the tidal amplitude is 79% reduced in the basin closest to the sea compared to the tidal amplitude in the sea.

To investigate future scenarios, a process-based hydro-morphological model is used. First, the model is calibrated on reproducing the measured tidal water levels as good as possible, using the depth and roughness as calibration parameters. Two future scenario cases are investigated with the calibrated model. The first scenario represents a continuation of the present situation 10 years into the future, where one of the channels is closed with man-made barriers (T1), while the second scenario represents a future state where the barriers are removed (T2). In T1, the bed level changes are limited. Removal of the barriers in scenario T2 causes rapid erosion of the eastern channel (~months-few years). Large erosion of the eastern channel causes the tidal wave to penetrate more into the system. Tidal choking is reduced from 79% in T1 to 29% in T2 in the first basin. In this case, the bedrock is assumed at -3 m in the eastern channel. The erosion is only limited by the unknown depth of the bedrock of the easterly channel. This is also the largest uncertainty of the model. The question is not if the channel will erode in scenario T2, but how much. Measuring the bedrock as a future work can greatly contribute to more accuracy of the results. The system is expected to be (more) inundated in the future due to the expected sea-level rise. This would give similar conditions as the Viking age.

Acknowledgements

Firstly, I would like to express my deepest gratitude to my main supervisor Professor William Helland-Hansen (University of Bergen) for providing this interesting project and for guiding and supporting me in the best possible way. During the last 2 years, he has always helped me with my questions, believed in me and always motivated me.

I owe a big thanks to Professor Haflidi Haflidason (University of Bergen) for his great contributions to my thesis. He always steered me in the right direction and the door to his office was always open to me, whenever I ran into a trouble spot or had a question about my research or writing.

I cannot express enough thanks to Gerard Dam, for his continued support and valuable contributions, especially throughout the modelling part of this thesis. He never stopped tracking my work and was always there whenever I needed him. The compilation of my thesis wouldn't have been that satisfying without his unlimited support and passion.

I would also like to extend my gratitude to Professor Tor Arne Johansen (University of Bergen) for his valuable contributions to my thesis, as well as hosting me in his house during the fieldwork and providing me with everything I needed at Lofoten.

I would also like to thank Associate Professor Henriette Linge (University of Bergen), who has been and will continue to be a role model for me since I knew her, for her valuable contributions.

I must express my very profound gratitude to my family for being very encouraging and believing in me as they always do. Feeling your support, even from a long distance, has always been the greatest motivation for me. Finally, I am very grateful to my friends for making me always smile, for supporting and encouraging me during these very stressful days, and for always helping me. Thank you.

Nil Sarper, October 2021

Table of contents

1. Introduction

Since the Stone Age, coastal areas have been important to humans for reasons such as secure access to food (fish, birds, etc.) and stable temperature conditions (e.g., Wickler, 2004; Glørstad et al., 2020). Therefore, these areas have witnessed many historical settlements and have served various ecological (e.g., marine life, birds) and socio-economic (e.g., boathouses, harbours, agriculture) functions. However, the coastal areas especially with the large ice sheet impact remained vulnerable to changing sea levels due to the rebound of the ice dominated land areas. Research on coastal processes in lowland areas such as The Netherlands and Denmark has a long tradition, but in Norway where the coastal area is generally steep and rocky, research has focused more on archaeological and general sea-level studies.

Norway's landscape is dominantly formed by the glaciations (e.g., Nesje & Whillans, 1994; Mangerud et al., 2011; Olsen et al., 2013) and experienced a glacio-isostatic rebound and an increase in sea levels (Hafsten, 1960; Hafsten & Tallantire, 1978; Møller, 1984, 1986, 1989; Svendsen & Mangerud, 1987; Romundset et al., 2011). According to studies by Møller (1986) and Vorren & Moe (1986) in the Lofoten-Vesterålen area, the relative sea level was 1.2 - 1.7 m higher during the Viking age (800-1050 AD) than today. These sea-level changes have had in general only a minor effect in most coastal areas of Norway, but; in some areas where the 'inland' of the coastal area has a low topography, the sea-level that rise the last *c.* 1000 years had a major influence.

One example of the area where the sea level during the Viking period was 1.2 - 1.7 m higher than it is today is Innerpollen, a lake is located on Vestvågøy (Fig. 1). During the Viking Age, this area was a stronghold where the longboats had a natural passage at the coast but could be transported ~8 km through the small lakes to the Viking Longhouse (Balascio & Wickler, 2018; Balascio et al., 2011). In recent times the Innerpollen has been mainly isolated from the sea due to the rebound of Scandinavia and has become a lake with a shallow connection to the sea (Fig. 1). The depth of the channels became so shallow that it acted as a barrier between Innerpollen and the open sea. This emerged barrier was dredged out in 1991 to allow (Viking) ships to sail again between Innerpollen and the open ocean. The removal of the barrier had, however, a major influence on both the water exchange and the sediment transport. Faster land uplift also resulted in an isolated

marine fish strain in one or two lakes when the inlet became nearly isolated from the marine area. With the predicted sea-level rise for the coming years, the current situation probably represents a period of relative lowest sea level (Simpson et al., 2015).

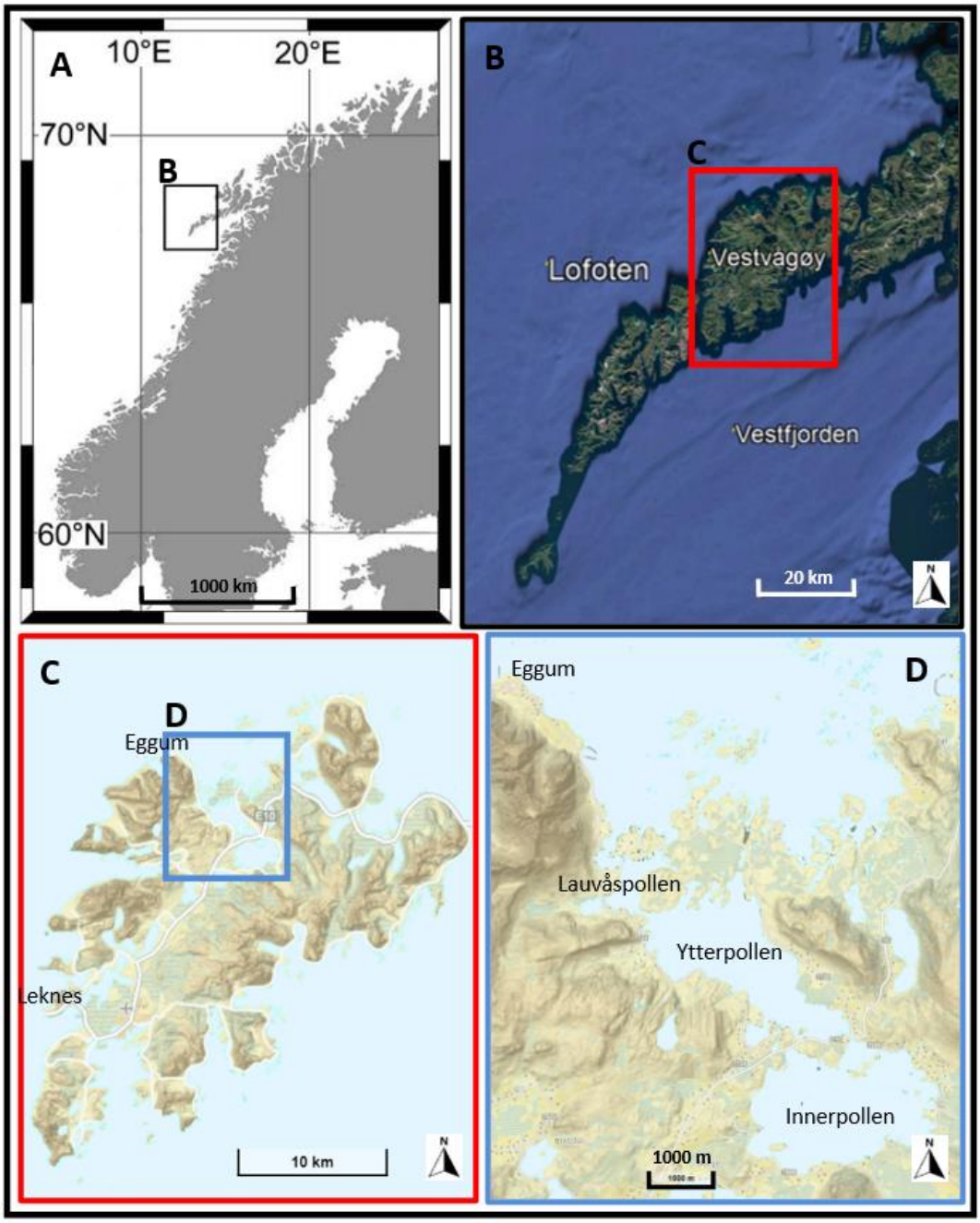

Fig. 1. Location of: (A) The Lofoten archipelago off the northwest coast of Norway, showing B, (B) Lofoten islands, showing C, and (C) Vestvågøy island, showing D. (D) The site map of the innermost Mjåsundet and connected basins (the study area).

This coastal area of Vestvågøy is due to the low topography very exposed for both sea-level changes and anthropogenic intervention. As the relationship between the hydro- and the

morphodynamic processes on the one hand and the geological/environmental setting, on the other hand, is very integrated, the consequences of changing one of these parameters can be damaging. The consequences of dredging out and opening the channel need to be investigated. For these purposes, the geological, hydrological, and morphological conditions of the study area should be examined in terms of past, present, and future situations. The development of numerical modelling and its introduction to computers has made it more effective to explore the range of system dynamics at varying spatial and temporal scales. Once the boundary conditions and other variables are defined, the model can run with different scenario cases, which is a great benefit, especially in terms of quality and cost. However, reliability and the accuracy of the morphological modelling for the long term is debated in the literature and remain questionable (Haff, 1996).

In this thesis, the integration of field methods and computational methods is used to define hydro- and the morphodynamic processes. Firstly, the five geological field studies are conducted in the study area and the data is gathered from echosounder, drone images, sediment samples, current meter, and water level loggers. This gathered geological data from the field is integrated with the computational method. As a computational method, the process-based hydro- and morphodynamic model FINEL2d is used to calculate the long-term changes in the morphology, sediment transport and water flow. For details and the governing equations of the FINEL2d model Dam et al. (2005, 2007, 2009) and Dam and Bliek (2013) is referred.

1.1 Study area

Lofoten is an archipelago located in Nordland county, in northern Norway (Fig. 1). The archipelago is separated from the mainland by Vestfjorden, which is a glacially eroded trough (Rise et al., 2013). It includes the following islands listed from NE to SW; Austvågøy, Gimsøy, Vestvågøy, Flakstadøy, Moskenesøy, Værøy and Røst. The Lofoten-Vesterålen area is characterized by alpine landscapes with steep (sharp) peaks and narrow edges, strandflats, deep cirques, as a result of prolonged and repeated glacial erosion (e.g., Mangerud et al., 1996; Fredin et al., 2013). The mountains have steep sides that in several places go straight into the sea (Nygård et al., 2019).

Vestvågøy is the second-largest island in the archipelago. It is located between 68° 03' and 68° 21' N latitude and 13° 28' and 14° 10' E longitude. In Vestvågøy, the highest peak is 965 m.a.s.l., and

peaks are commonly found around 500-600 m high all over the island. The climate on Vestvågøy is Atlantic, which is typical for the west coasts in higher middle latitudes. Atlantic climate represents humid air, relatively high temperatures in the winter and relatively cool summers with much precipitation.

The study area is located in the area of Eggum, a small village on the seaside of Vestvågøy (Fig.1). Because the entire system is under influence of the oceanic tidal waters that extend to the innermost tidal basin, the study area is defined as a tidal inlet system in this thesis. Moreover, the hydrodynamic and morphodynamic processes of the system are dominantly affected by the tidal waters. At flood tide, oceanic waters passing through the Mjåsundet strait move along the

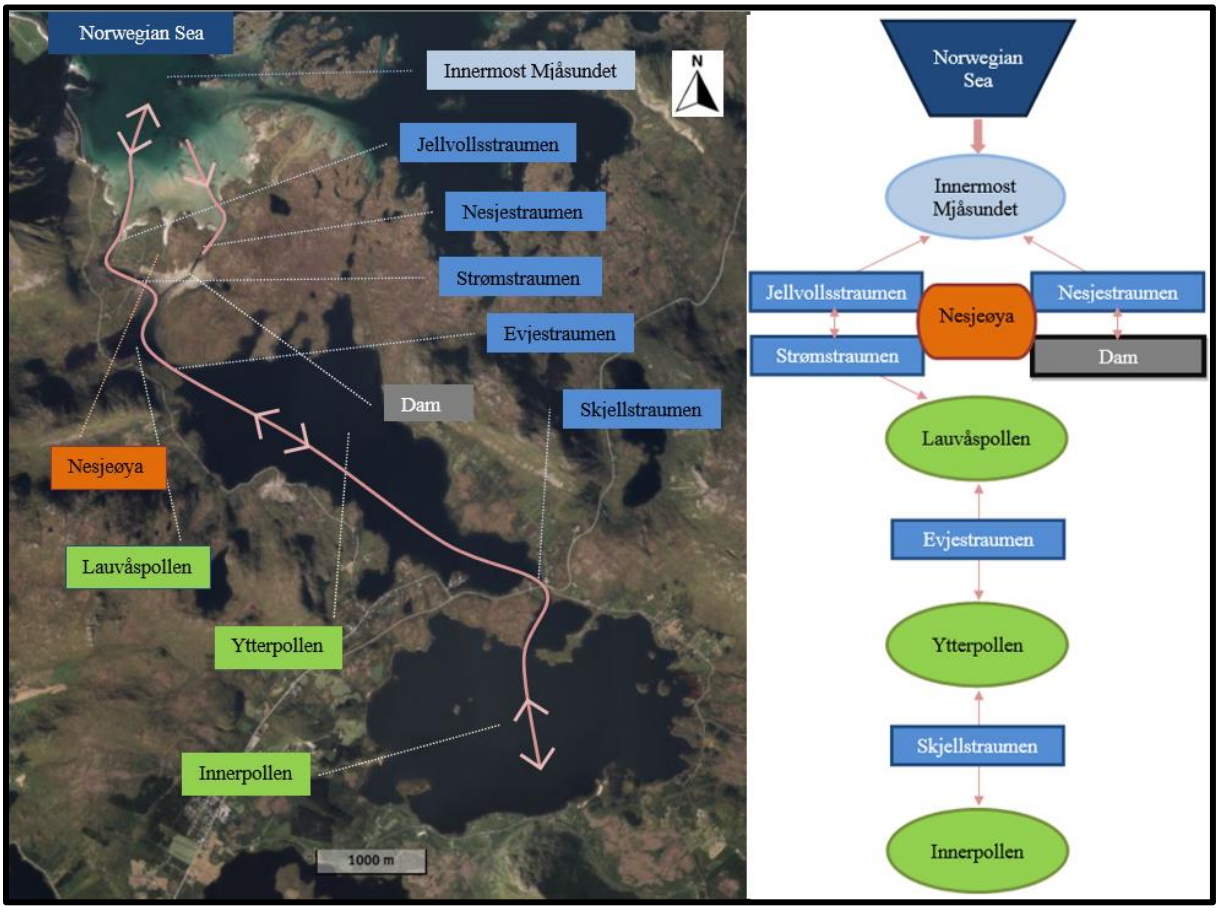

Fig. 2. Left: Pathways of water from open sea to the inner basins (pink line). Right: Schematized version of water pathway. Blue rectangles indicate the streams, whereas the green ellipses show the basins. Man-made dams are indicated with black rectangle.

Jellvollsstraumen to reach the inner basins (Fig. 2). As the Nesjestraumen is enclosed by a barrier at its southern end, there is a negligible amount of water moves in and out. The water continues to the Lauvåspollen passing under the ~18 m long bridge over Strømstraumen, then penetrates into

Ytterpollen by passing through the Evjestraumen, which is a bedrock-based channel. Finally, the water passes under the ~11 m long bridge over Skjellstraumen and reaches the innermost basin, the Innerpollen. During the ebb phase of the tide, the water follows the opposite path to reach the sea.

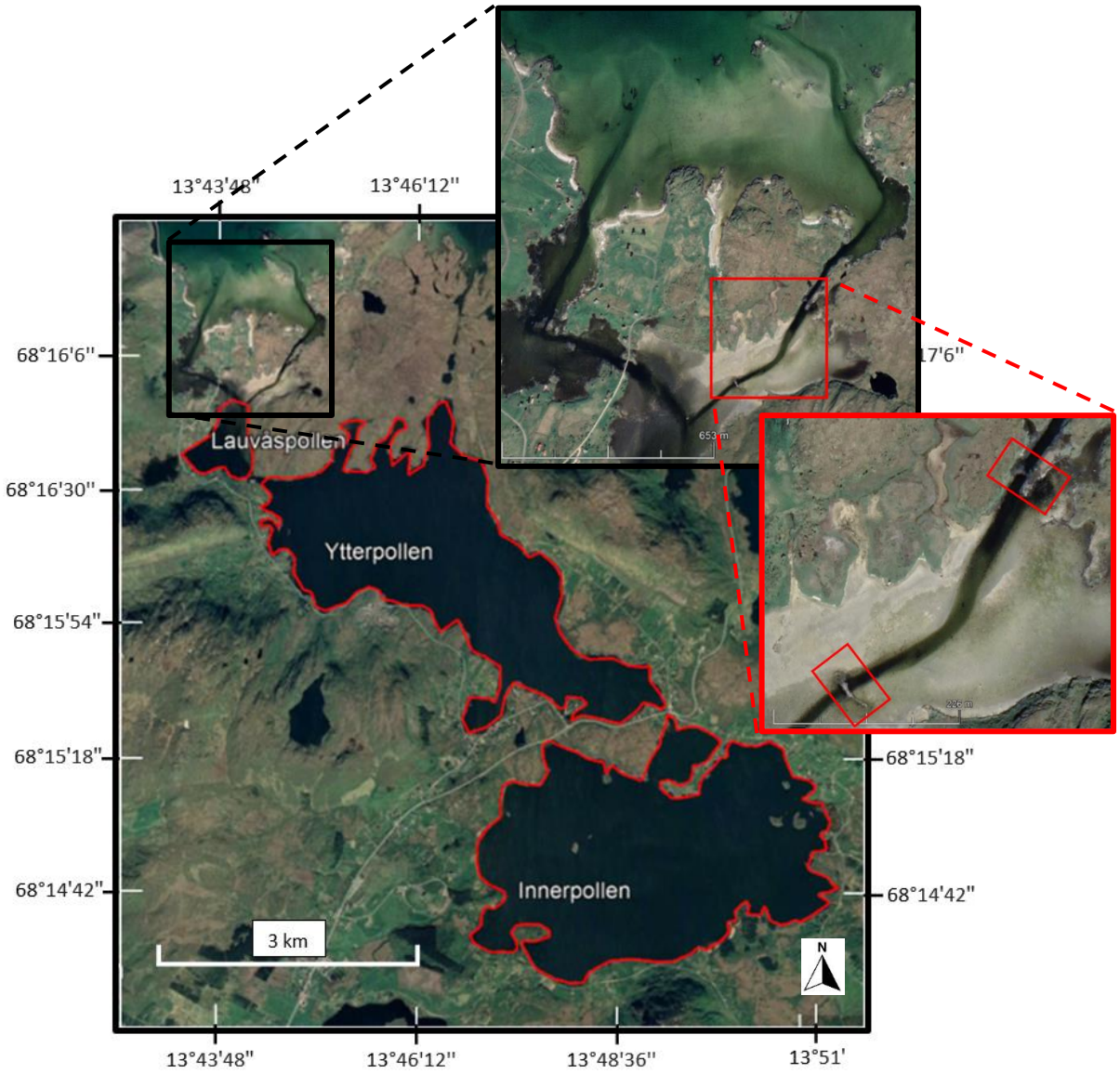

Fig. 3. Location of Innerpollen, Ytterpollen and Lauvåspollen. The current (2020) landscape of the channels between lakes and sea are indicated in the figure. Locations of man-made barriers are shown in the red box.

Nesjestraumen, one of the two channels located between the Mjåsundet and the basins, was already closed in natural conditions due to its topography (Figs 2 and 3). The natural structure was dug down in 1991 to create a passageway for boats to serve touristic purposes. Following this opening, complaints arose about water levels got lower during the ebb tide inside the basins. While most of

the water was circulating along the western channel under natural conditions, it was observed by the locals that after this opening, the water started to use Nesjestraumen more and its influence in Jellvollsstraumen decreased drastically (Fig. 2). In addition, excessive erosion in the eastern channel and different forms of sand deposition leading to changes in bathymetry have been noticed by the local people. Later, the channel was permanently closed with two barriers (Fig. 3) in 1996 by the decision of the authorities. The original closed state of the eastern channel and its state after opening can be seen from the aerial pictures shown in Figure 4.

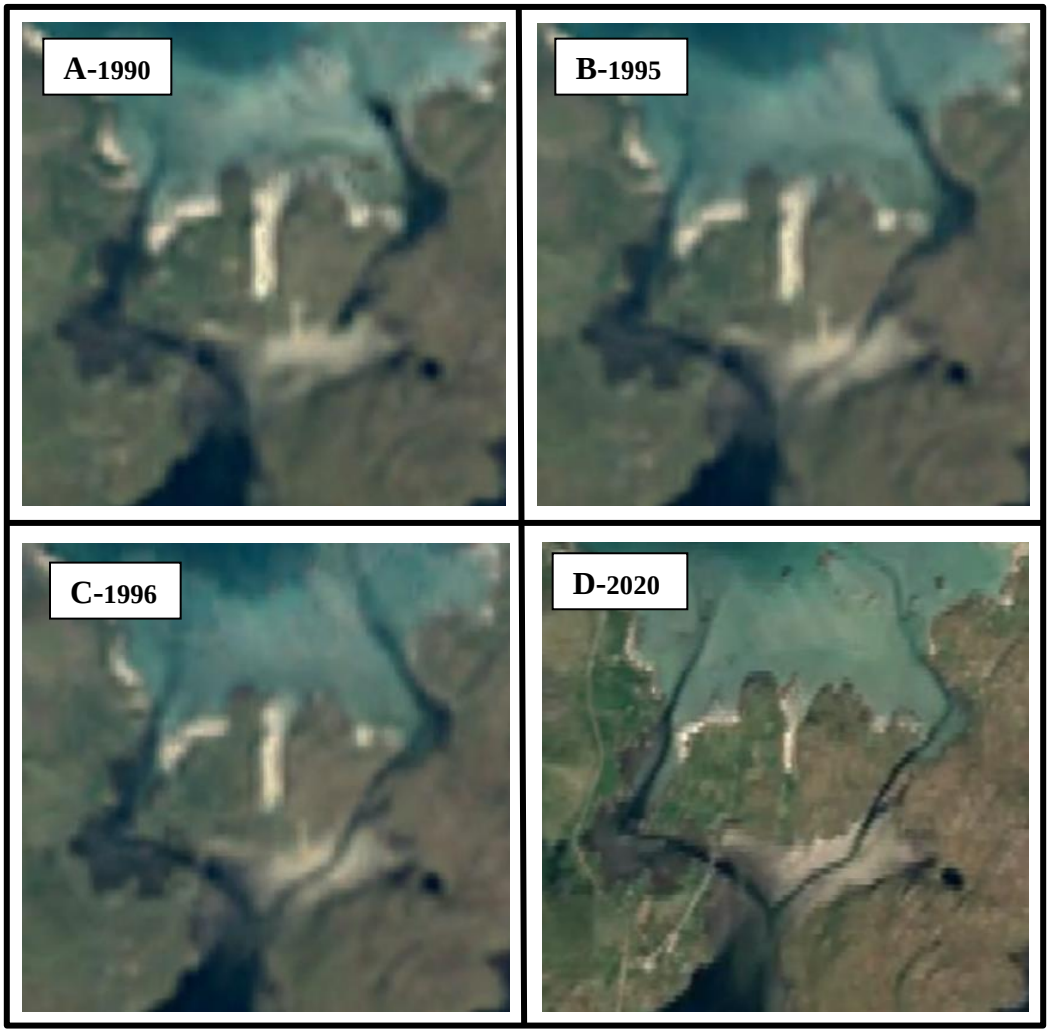

Fig. 4. The natural state of the channel (closed) on the eastern side A (at the year 1990). After the opening of channel B (in the year 1995). Reclosing of the channel C (at yeat 1996). The current state of channel D (at the year 2020) (Timelapse, n.d.).

1.2 Objectives of study

The main focus of the study is to understand the long-term (10 years) sedimentological and morphodynamic changes in the tidal inlet system after human influence. For the short term, it is possible to interpret the observations in a field, but to be able to understand the decadal-scale changes, process-based morphological modelling is applied. Possible further studies on the subject of this thesis will be pointed out in the recommendation chapter.

This thesis attempt to discuss and try to find an answer to the following specific questions:

- *How the system will respond morphologically and hydrologically to the removal of the barrier 10 years into the future, and how the tidal water components will be affected?*

- *What is the dominant tidal phenomenon in the study area today, and what effect does the formation of the system have on this phenomenon?*

- *How has the system responded to relative sea-level changes since the Late Iron Age, and what are the possible consequences of rising sea levels in the future?*

- *What are the uncertainties in the model and what are their possible implications for the results?*

2. Background

2.1 Geological background

The geological history of the Lofoten-Vesterålen terrain is summarized by Griffin et al. (1978) as mainly a repeated vertical movement (minimum 30 km), possibly accompanied by deep erosion. Although there are some mountains with smooth undulating paleo-surfaces formed before glaciations, the landscape is generally characterized by landforms of moraines in the Lofoten archipelago. The marine landscape includes the strandflat crystalline platform on the Lofoten coast, shallow marine valleys on the narrow continental shelf with sedimentary rocks, and fjords and valleys that are the result of intense (concentrated) glacial erosion during repeated glaciations (Bøe et al., 2020; Mokhtari & Pegrum, 1992; Møller, 1984).

The geologic history of Vestvågøy is a complex sequence of metamorphic, structural, and magmatic events (Tull, 1973). The bedrock in our study area is predominantly mangerite defined as highly weathered bedrock (Olesen et al., 2012). In addition to this rock group, gabbro and granitic gneiss is dominating the bedrock around the basins in the study area.

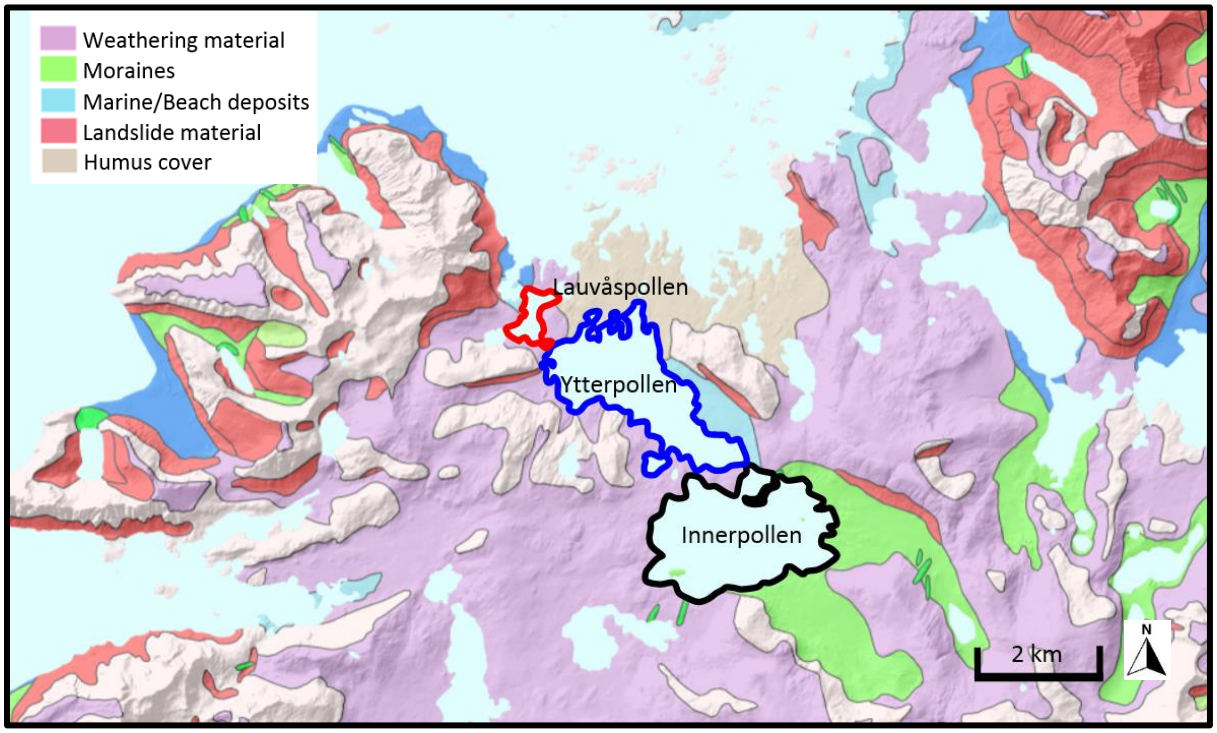

Fig. 5. The landscape around the study area with the main classes of the deposits prevailing in the area (NGU, n.d.)

Superficial deposits around the study area are mainly represented by weathering loose material formed on-site by the physical or chemical decomposition of the bedrock (Fig. 5). At the entrance of the tidal inlet, humus covers are seen directly on the bedrock. Bare mountains are reaching up to 950 m in height (Fig. 6), and on the foothills of these mountains, there are deposits mainly originating from landslides from steep valley sides. Moraine materials are mostly dominant around Innerpollen. Fjord, marine and beach deposits are present around Ytterpollen as a thin cover over the bedrock.

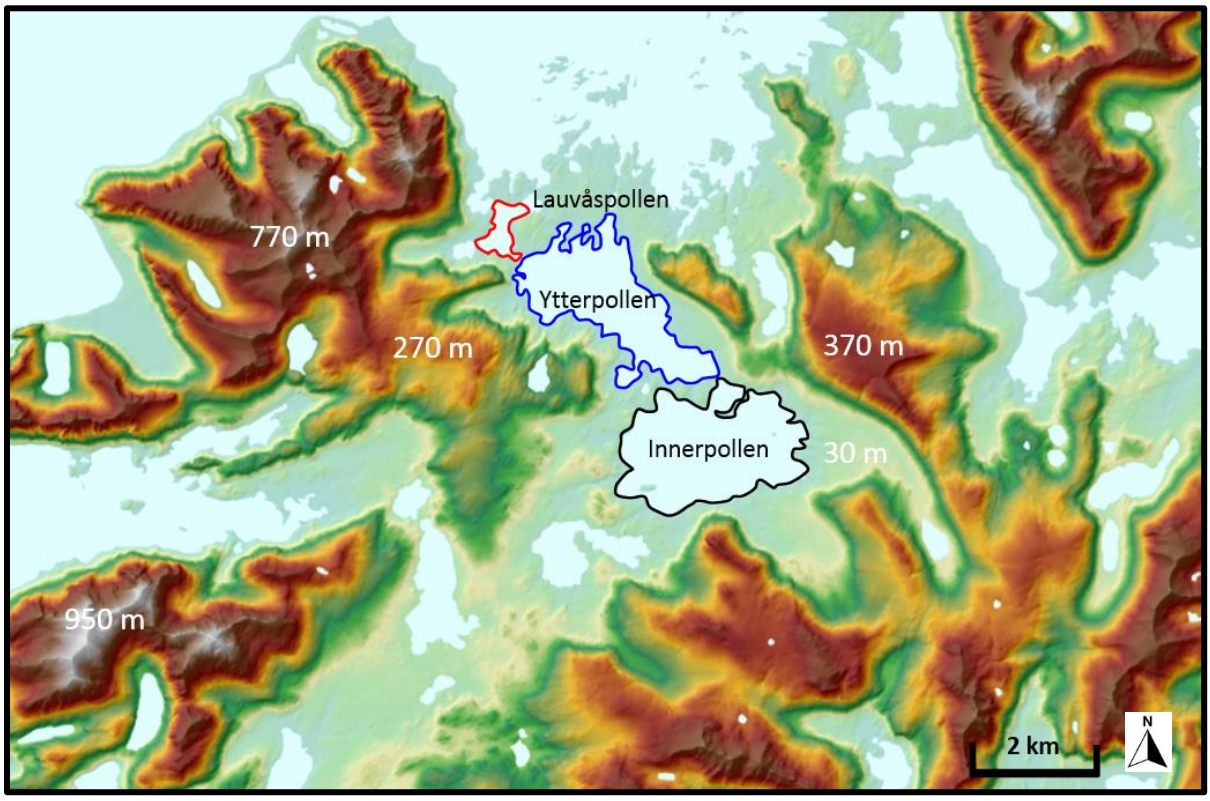

Fig. 6. Colour shaded topographical map showing the main characteristic patterns of the study area (Høydedata, n.d.)

During the Last Glacial Maximum (LGM) (18-22 ka B.P.), the ice sheet extended to the shelf edge off Vestvågøy followed by full deglaciation at around 15 ka B.P. (Olsen et al., 2013). Being close to our study area, the large Vestfjorden – Trænadjupet troughs acted as a drainage route for Scandinavian ice sheets and played an important role in the ice sheet pattern and dynamics of this area (Ottesen et al., 2005; Vorren et al., 2015). During deglaciation, grounding zone wedge (GZW) and end moraines were deposited, and relative sea-level dropped due to isostatic rebound at about 16.2 ka with ~15 m (Vorren et al., 1988, 2015).

2.2 Sea level changes

It is suggested by Møller (1984) that the highest shoreline during the Holocene was formed in the early to mid-Holocene at *c.* 6530 cal. yr BP with 9 m, before it regressed because of the glacio-isostatic uplift. Innerpollen, which is the innermost basin in our study area, responded to the effects of both land uplift and changing climatic conditions related to neoglacial cooling and warming trends over the last 4600 years (Mills et al., 2009). Diatom analysis from Innerpollen also revealed that as a result of the glacio-isostatic rebound, isolation of the basin from the North Atlantic started after *c.* 560 cal. yr BP, relative sea levels dropped almost 0 m at *c.* 450 cal. yr BP and the basin reached full isolation by *c.* 230 cal. yr BP (Mills et al., 2009). The reconstructed shoreline displacement curve by Møller (1986) and Marthinussen (1962) suggests that the relative sea levels were 1.2-1.7 m higher than today during the Viking Age (800-1050 AD) (Fig. 7).

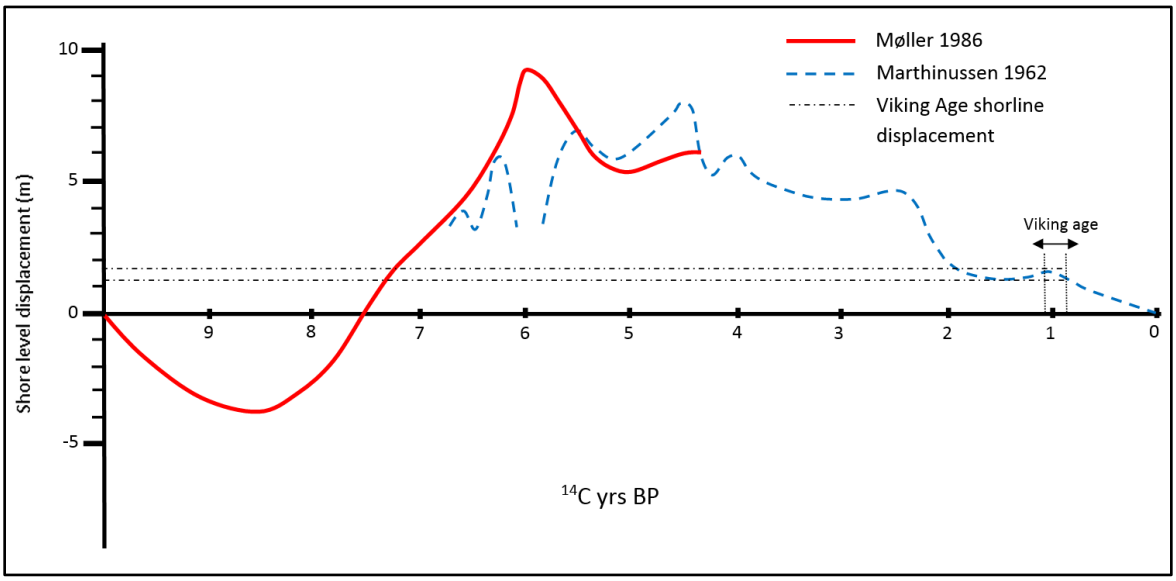

Fig. 7. Shoreline displacement curve, North Norway. After Møller (1986) and Marthinussen (1962). Shoreline displacement levels during the Viking age is indicated with dashed lines.

2.3 Tidal inlet systems

Tides are representing the short-term fluctuations in the water level caused by the deformation of the ocean surface by the gravitational attraction of the moon and the sun (Wahr, 1995). Tides create tidal currents due to differences in tidal water elevation. Tidal currents are capable of eroding, transporting, and accumulating soft sediments. Local conditions such as the bathymetry and the

geographical location (Coriolis effect) also influence the magnitude and the timing of the tidal cycle (Gornitz, 2013).

Tidal inlet systems are complex hydraulic systems where saline water from the open sea penetrates the land through a long and narrow channel (tidal inlet), and the system consists of one or more tidal basins, flood and ebb-tidal deltas and most of the time, freshwater input from the rivers (Ren & Zhang, 1985). Tidal oscillations leading to the flood velocities of the basin are the main supplier of water to tidal inlet systems from the open sea. Tidal waters are mainly governed by the interaction between tidal currents, waves, wind effects, and sedimentological and morphological features of the basin (Dastgheib et al., 2008). Morphodynamic behaviours of the tidal inlet systems (de Swart & Zimmerman, 2009) are affected by factors such as flood-ebb durations, bathymetry, discharge of freshwater and sediment transport through the tidal inlets in addition to the tidal prism (volume of exchanged water) (Jia & Gao, 2008; Gao & Collins, 1994; Xie et al., 2010). Tidal morphology in the long term is largely related to net sediment exchange between the adjacent seas and the enclosed tidal basins (D'Alpaos et al., 2010).

There are a wide variety of tidal inlet systems due to different morphological and geological settings and diversity in sedimentological, hydrological and meteorological controls (FitzGerald & Miner, 2013; Hayes & FitzGerald, 2013). Different coastal systems such as estuaries are exposed to complex hydrodynamic processes by the tidal currents which are responsible for most of the morphological and sedimentological features in those environments (Martin, 2009).

Due to their complexity as outlined above, it is important to understand the tidal inlet systems. Since there is limited information about long-term (decadal) processes, developing a numerical morphodynamic model would significantly help to understand the physical processes around tidal inlets (Xie et al., 2010). Thanks to the engineering work, hydrodynamics and morphological equations, and their introduction to computers, these long-term changes can be estimated, although there is a significant degree of uncertainty. Moreover, with the modern developments of computational powers and smart morphological updating techniques, it is possible to generate high-resolution (~100m) morphological models over decades to millennia in broad areas (~100km) with running time of days to weeks on a standard computer (Dam et al., 2016).

3. Geological field/lab methods and data gathering

3.1 Introduction to methods

In this study, a combination of field/laboratory methods and computational methods is used. In this chapter, the methods applied during the fieldwork of the study are explained and presented together with the gathered data from each method. In the following chapter, Chapter 4, the computational method is described. The data gathered from the field methods are used as the input of the computational method as well as used for calibrating the model in parameters such as bathymetry. Both the gathered field data, and the computational methods are integrated, and the results are displayed in Chapter 5.

Data for investigating the decadal-scale morphological development of the innermost Mjåsundet and connected inland basins were retrieved by using a range of data and methods.

- Bathymetry was recorded with an echosounder (Chapter 3.2);
- Surface topography was determined using a photogrammetric compilation of drone pictures (Chapter 3.3);
- Sediment samples were collected at selected locations (Chapter 3.4);
- The current meter was deployed to record current strengths (Chapter 3.5);
- Water level loggers were used to measure the water pressure (Chapter 3.6).

Data of the echosounder, drone pictures, sediment samples and current meter were collected in a total of 10 days in August 2020. Water level loggers were deployed for a longer period from 07.01.2021 to 23.03.2021.

3.2 Bathymetric mapping with echosounder

To map the bathymetry, the LOWRANCE Elite-7 Ti echosounder was used across the two tidal basins (Lauvåspollen and Ytterpollen; Fig. 8). The echosounder has a GPS, medium/high CHIRP (Compressed High-Intensity Radar Pulse) sonar system, and Structure Scan system with side scan and down scan imaging which allows covering bed topography both beneath and to the sides of the

device. The frequency of the transducer was automatically adjusted by the echosounder between 200-50 kHz. Three longitudinal (along the basin long axis - from the one channel entrance to another) and many transverse trackways were followed, and the depths were recorded from a total of 1794 points. The longest trackway was 3.5 km longitudinally and 1.65 km transversally from Innerpollen and 0.60 km longitudinally and 0.54 km transversally from Ytterpollen (Fig. 8).

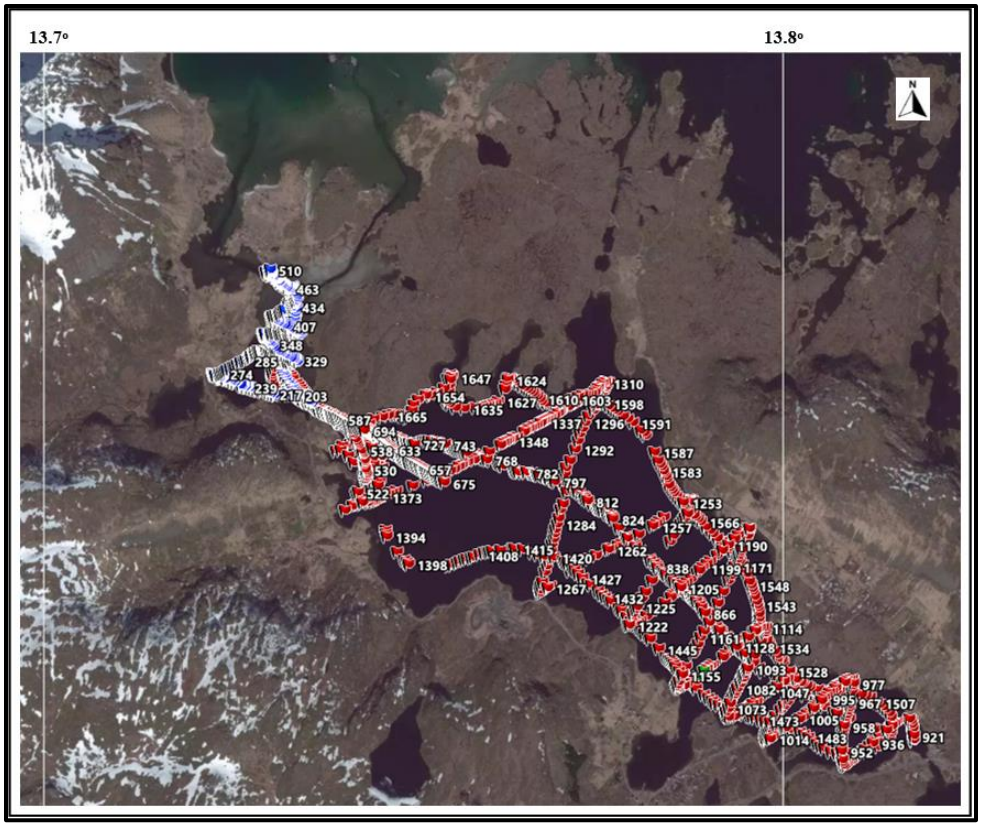

Fig. 8. Track ways of the echosounder survey and the depth recording points. The colours of the flags indicate different basins. Lauvåspollen is shown with the blue flags and Ytterpollen with the red flags.

The bathymetric map of the Lauvåspollen and Ytterpollen is shown in Figure 9. The deepest point at Lauvåspollen was recorded as 4.9 m and at Ytterpollen as 65.7 m. The depth values from the measurements are used as the input for the manual adjustment of the bathymetric map in the grid model (Chapter 4).

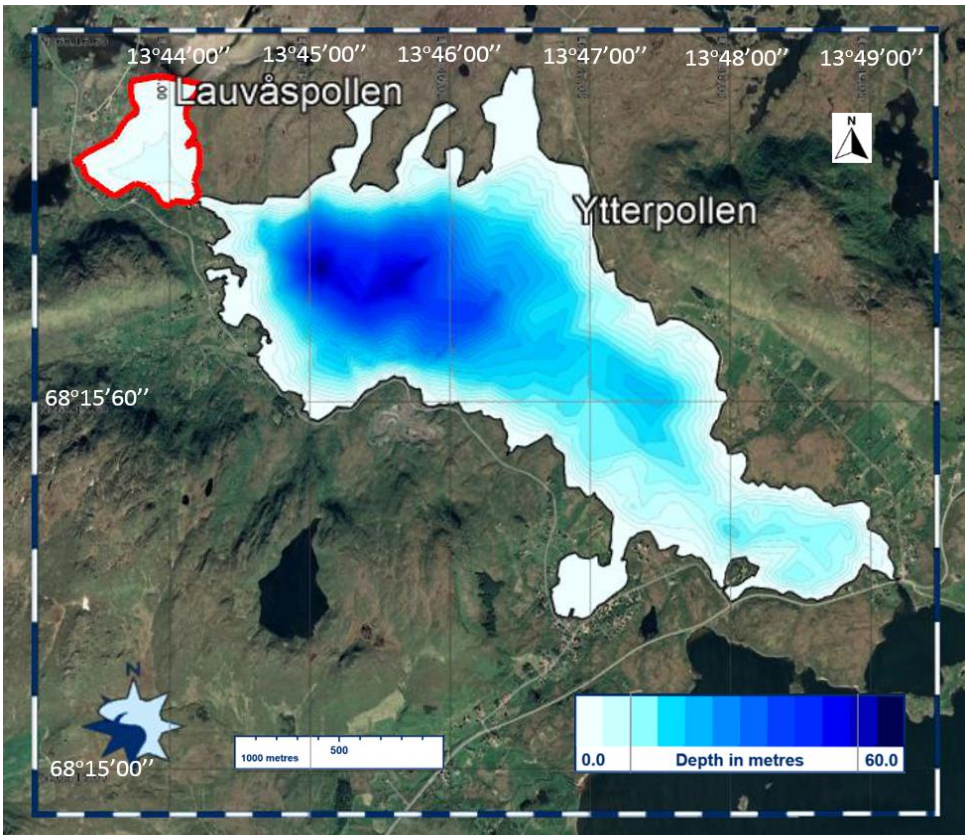

Fig. 9. Bathymetric survey results from Lauvåspollen and Ytterpollen. Lauvåspollen is outlined with red colour.

3.3 Photogrammetric compilation of done images

Drone survey with DJI MavicPro was conducted above the two channels (Jellvollsstraumen and Nesjestraumen) between the Innermost Mjåsundet and Lauvåspollen. This survey aimed to study the changes in geomorphology and sedimentology by comparing this bird's eye view with the older aerial photos and satellite images (cf. Fig. 4). The data is used for further modelling purposes, as well as to decide the locations of the sediment samples collected for interpreting the tidal current effects across the tidal inlets. The area was separated into four grids and the surveys were acquired separately (Fig. 10). For each grid, the drone was flown from a height of 120 m for about 16 minutes and around 260 photos were recorded.

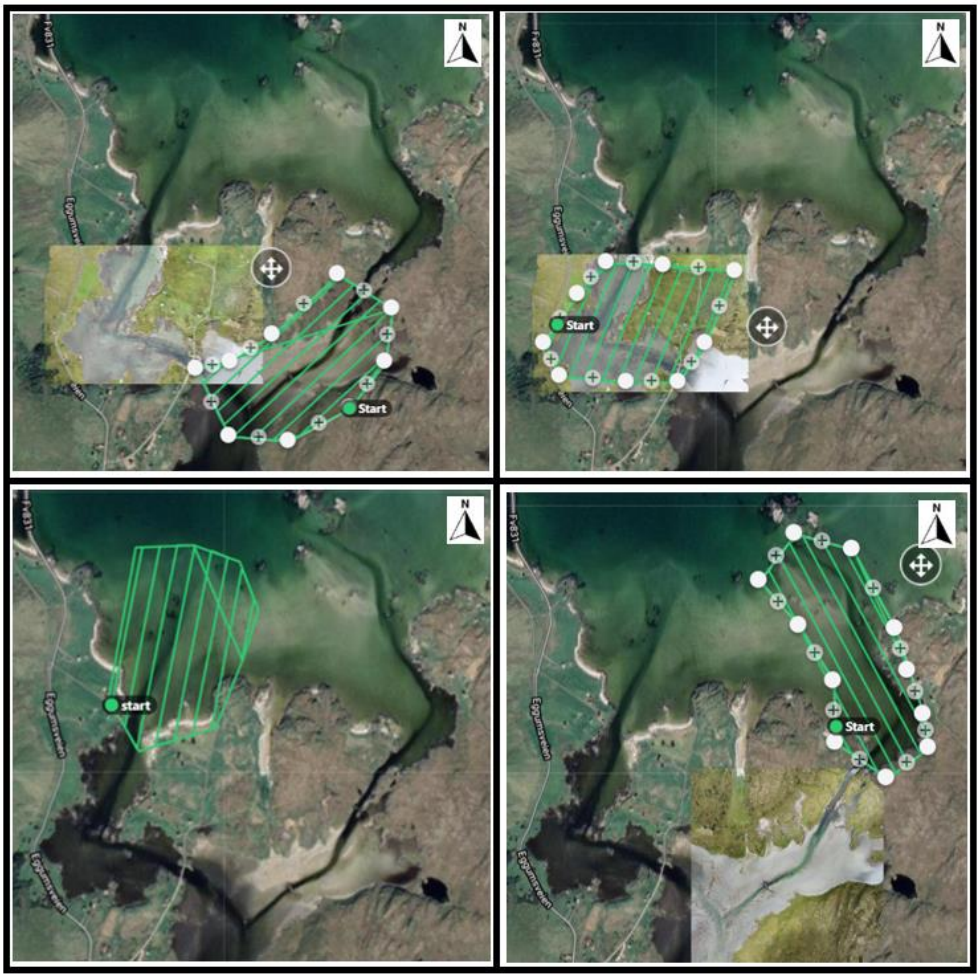

Fig. 10. The four designated different flight paths (green lines) for the drone survey. The starting point of drone is indicated in the figure with green point.

Figure 11 (right) shows images compiled from the drone study adapted to a map image by DroneDeploy (drone mapping software). The changes in the dynamics of the channels can be obtained by comparing the two images from 1985 (Kartverket, n.d.-a) and 2020 (Fig. 11). The currents in both channels, especially in the part towards the sea, were caused a new flow path to be formed as a result of the channel that was opened in 1991 (Fig. 4). It can be seen from the pictures that the extent of the channel was decreased, which is more evident in the extension of the western channel towards the open sea. This could be an effect of flow-weakening caused by the opening of the channel.

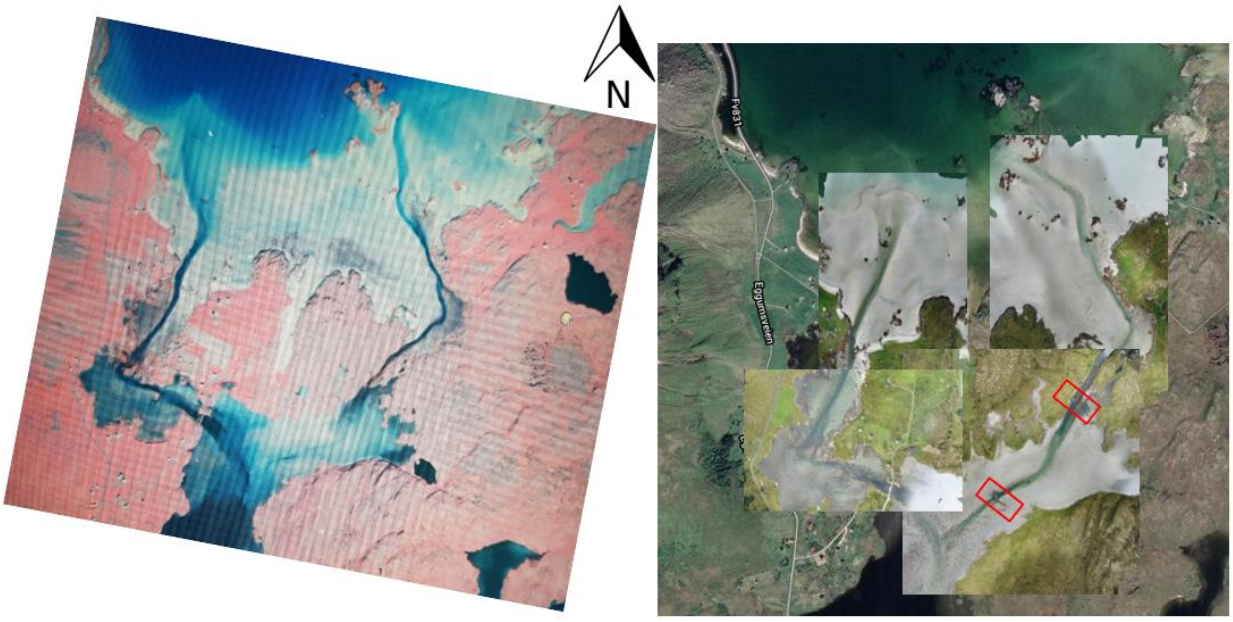

Fig. 11. Map view of the study area from 1985 (Kartverket, n.d.-a) (left) and merged view of four separate drone surveys (2020) (right). Two bridges are shown on the map with red rectangles.

3.4 Sediment sample analysis

In total, 50 sediment samples were collected around the Nesjeøya during the low tide phase (Fig. 12). The location of the sample sites was decided by considering field observations as well as the comparison of the aerial photographs taken both in 1985 (Kartverket, n.d.-a) and in 2020. The samples furthest from land (e.g., Ner42) were collected at the low tide from approximately 450 m north of the seaward border of the Nesjeøya.

A total of 17 sediment samples (Fig. 12) were chosen among the 50 collected samples for further laboratory investigations to analyse the grain size distribution as well as the terrestrial/carbonate ratio. These 17 samples were selected considering the places where the sediment properties are likely to be affected the most, according to the changing direction of the flow from the past to the present.

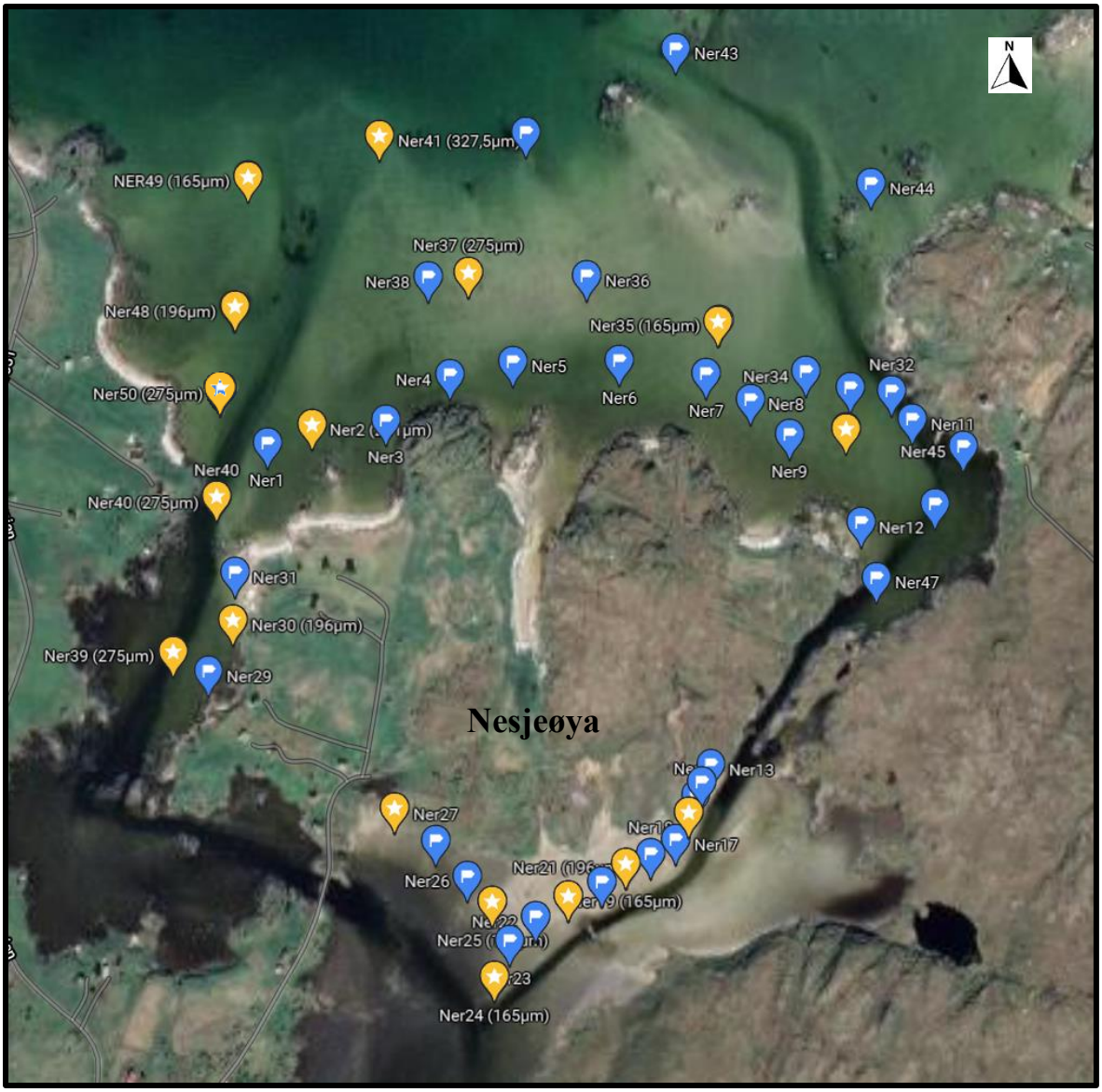

Fig. 12. Locations of the 50 samples collected around Nesjeøya. Yellow markers illustrate the investigated 17 samples and the blue markers shows the unanalysed samples. Peak values from the grain size graphs are also indicated next to the yellow markers.

Both wet and dry sieving methods were used for documenting the grain size distributions and terrestrial to carbonate ratio by using the following mesh sizes: <50 µm, 63 µm, 125 µm, 150 µm, 180 µm, 212 µm, 250 µm, 300 µm, 355 µm, 425 µm, 500 µ, 1000 µm and >1000 µm (Table 1). Following the sieving process, the samples in each interval were analysed under the microscope to determine the terrestrial-to-carbonate ratio (Table 1).

Table 1. Results for sediment sample analysis after wet and dry mesh sieving. The first column indicates the mesh sizes. The uppermost table is showing the grain sizes in grams, and the middle table in percentage. The lower table indicates the terrestrial-to-carbonate ratio for each mesh size. In the middle table, the highest values are highlighted in grey colour. In the lower table, equal values of the T:C ratio of each sample are highlighted in orange colour. Sediments collected along the western channel are indicated by the red box above the sample names. Others, without red boxes, represent samples collected along the eastern channel. The colour code is given at the bottom of the table.

gram	NER41	NER49	NER37	NER48	NER35	NER50	NER2	NER10	NER40	NER30	NER39	NER28	NER16	NER19	NER25	NER21	NER24
50	0,01	0,01	0,01	0,03	0,11	0,01	0,02	0,04	0,01	0,25	0,04	0,33	0,42	0,21	0,09	0,1	0,07
63	0,27	2,29	0,61	0,68	5,17	0,18	1,16	3,07	0,57	1,52	0,70	2,19	1,96	4,04	3,31	2,72	2,14
125	0,72	3,25	1,55	1,29	6,61	0,43	1,46	3,94	1,78	1,53	1,37	2,74	2,63	4,40	3,04	2,89	3,91
150	1,94	11,60	3,96	3,77	11,94	1,01	3,24	4,63	4,26	3,99	2,71	5,02	4,44	8,58	6,63	4,34	10,97
180	3,61	8,31	7,15	8,33	5,95	3,00	5,39	3,19	5,03	7,62	3,75	5,24	6,33	5,69	11,27	4,23	6,94
212	5,41	6,49	8,25	7,69	4,06	6,71	8,09	2,60	4,37	6,92	5,01	6,20	3,35	4,45	5,18	3,18	5,14
250	4,32	4,88	13,84	4,6	3,17	9,56	5,01	1,47	12,00	6,22	6,31	4,43	2,01	5,09	2,31	1,54	5,73
300	6,57	2,11	2,24	2,84	0,74	6,11	3,27	0,88	3,19	3,85	2,49	3,44	1,1	1,64	0,87	0,93	0,53
355	6,06	2,01	2,04	1,3	0,44	5,52	2,71	0,55	1,96	2,81	1,49	2,77	0,57	1,32	0,69	0,78	0,46
425	1,99	0,92	0,60	0,54	0,30	2,63	1,42	0,29	0,86	1,45	0,72	1,64	0,25	0,58	0,5	0,43	0,16
500	2,22	1,48	0,64	0,58	0,23	2,08	2,04	0,38	0,90	1,71	1,38	2,88	0,42	0,59	0,7	0,65	0,54
1 000	0,34	0,19	0,12	0,02	0,02	0,04	0,09	0,41	0,11	2,38	0,10	0,69	0,08	0,08	0,02	0,05	0,02
Total	33,46	43,54	41,01	31,67	38,73	37,28	33,90	21,45	35,04	40,25	26,07	37,57	23,56	36,67	34,61	21,84	36,61

%	NER41	NER49	NER37	NER48	NER35	NER50	NER2	NER10	NER40	NER30	NER39	NER28	NER16	NER19	NER25	NER21	NER24
50	0,03 %	0,02 %	0,03 %	0,09 %	0,27 %	0,03 %	0,06 %	0,17 %	0,02 %	0,62 %	0,15 %	0,88 %	1,78 %	0,56 %	0,26 %	0,46 %	0,19 %
63	0,81 %	5,26 %	1,49 %	2,15 %	13,35 %	0,48 %	3,42 %	14,32 %	1,63 %	3,78 %	2,68 %	5,83 %	8,32 %	11,02 %	9,56 %	12,45 %	5,85 %
125	2,15 %	7,47 %	3,78 %	4,07 %	17,07 %	1,15 %	4,31 %	18,37 %	5,08 %	3,80 %	5,25 %	7,29 %	11,16 %	12,00 %	8,78 %	13,23 %	10,68 %
150	5,80 %	26,64 %	9,66 %	11,90 %	30,83 %	2,71 %	9,56 %	21,59 %	12,16 %	9,91 %	10,39 %	13,36 %	18,85 %	23,40 %	19,16 %	19,87 %	29,96 %
180	10,79 %	19,09 %	17,43 %	26,30 %	15,36 %	8,05 %	15,90 %	14,87 %	14,36 %	18,93 %	14,38 %	13,95 %	26,87 %	15,52 %	32,56 %	19,37 %	18,96 %
212	16,17 %	14,91 %	20,12 %	24,28 %	10,48 %	18,00 %	23,86 %	12,12 %	12,47 %	17,19 %	19,22 %	16,50 %	14,22 %	12,14 %	14,97 %	14,56 %	14,04 %
250	12,91 %	11,21 %	33,75 %	14,52 %	8,18 %	25,64 %	14,78 %	6,85 %	34,25 %	15,45 %	24,20 %	11,79 %	8,53 %	13,88 %	6,67 %	7,05 %	15,65 %
300	19,64 %	4,85 %	5,46 %	8,97 %	1,91 %	16,39 %	9,65 %	4,10 %	9,10 %	9,57 %	9,55 %	9,16 %	4,67 %	4,47 %	2,51 %	4,26 %	1,45 %
355	18,11 %	4,62 %	4,97 %	4,10 %	1,14 %	14,81 %	7,99 %	2,56 %	5,59 %	6,98 %	5,71 %	7,37 %	2,42 %	3,60 %	1,99 %	3,57 %	1,26 %
425	5,95 %	2,11 %	1,46 %	1,71 %	0,77 %	7,05 %	4,19 %	1,35 %	2,45 %	3,60 %	2,76 %	4,37 %	1,06 %	1,58 %	1,44 %	1,97 %	0,44 %
500	6,63 %	3,40 %	1,56 %	1,83 %	0,59 %	5,58 %	6,02 %	1,77 %	2,57 %	4,25 %	5,29 %	7,67 %	1,78 %	1,61 %	2,02 %	2,98 %	1,47 %
1 000	1,02 %	0,43 %	0,29 %	0,06 %	0,04 %	0,11 %	0,27 %	1,91 %	0,32 %	5,91 %	0,40 %	1,84 %	0,34 %	0,23 %	0,06 %	0,23 %	0,05 %

Ratio(T:C)	NER41	NER49	NER37	NER48	NER35	NER50	NER2	NER10	NER40	NER30	NER39	NER28	NER16	NER19	NER25	NER21	NER24
50																	
63																	
125	95:5		95:5	95:5		85:25	95:5			90:10			90:10	95:5	90:10	90:10	
150	95:5			95:5	95:5	70:30	90:10	95:5	95:5	75:25			75:25	95:5	85:15	90:10	95:5
180	90:10	95:5		90:10	70:30	60:40	85:15	90:10	90:10	60:40			50:50	90:10	80:20	60:40	
212	80:20	90:10	70:30	80:20	50:50	60:40	80:20	90:10	70:30	50:50	90:10	50:50	40:60	50:50	70:30	50:50	90:10
250	50:50	60:40	50:50	70:30	40:60	50:50	50:50	80:20	50:50	50:50	90:10	40:60	30:70	40:60	50:50	30:70	70:30
300	30:70	50:50	40:60	50:50	30:70	20:80	20:80	50:50	30:70	30:70	60:40	30:70	20:80	30:70	40:60	20:80	50:50
355	30:70	30:70	20:80	30:70	20:80	10:90	20:80	30:70	10:90	20:80	50:50	20:80		20:80	30:70		50:50
425	20:80		20:80	20:80	10:90						30:70	20:80		10:90			50:50
500			5:95								5:95			5:90			10:90
1 000																	

colour code

seaward landward

Grain size statistics were calculated by using Gradistat Version 9.1 (Blott & Pye, 2001). According to single sample statistics (Appendix), the grain size distribution for all samples is classified as moderately well-sorted fine sand. For most of the samples, the ratio of terrestrial dominant environment changes to carbonate dominant environment after 250µm (Table 1). The majority of the samples show a terrestrial dominant environment.

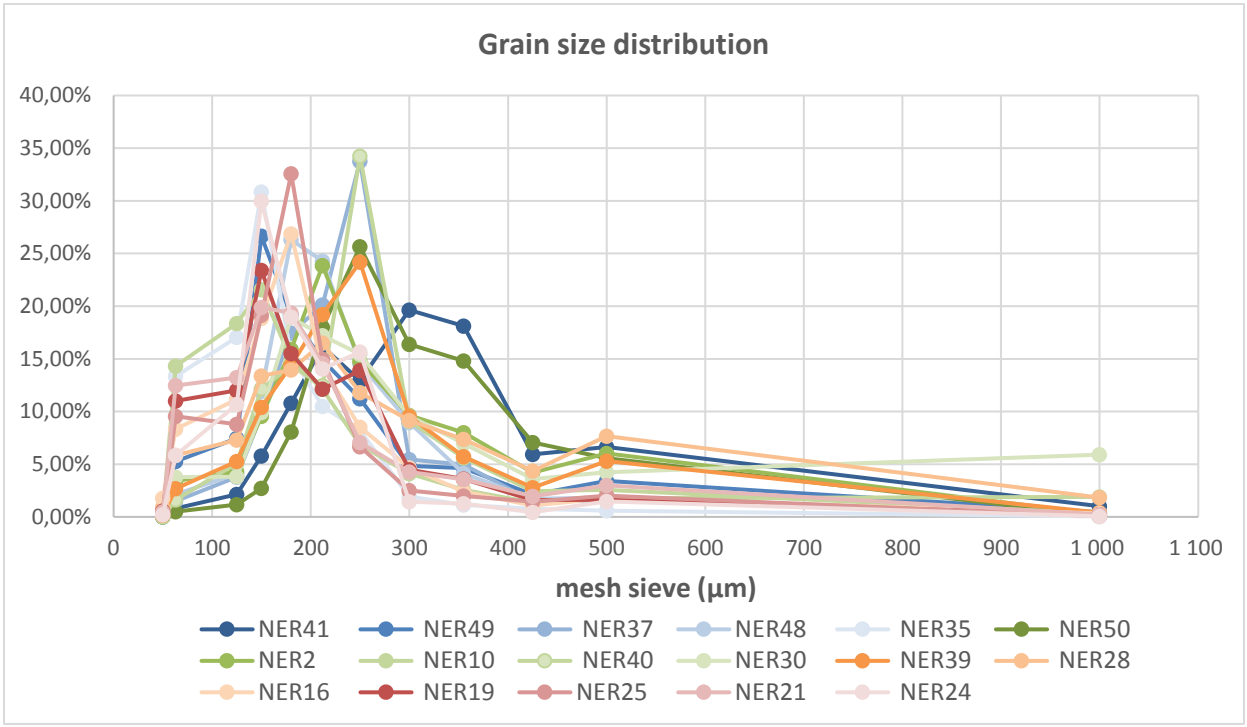

Fig. 13. Line/scatter plot for the results of the grain size analysis.

The grain size distribution for all samples is plotted in Figure 13. Distribution plots are divided into four groups according to the similarity of the peak values (Fig. 14). Six samples from the first group with a peak of 150 µm are located along the eastern channel (see Figure 12 for locations), except one (Ner49) taken from one of the furthest points to the seaside (Fig. 12). Within the second group, which represents the second finest sediment size in our study with a peak of 180 µm, there are three samples from the western channel and one sample (Ner16) from the eastern channel. All the samples from the third group with a peak at 250 µm grain size are distributed along the eastern channel. Three samples with two different grain sizes that cannot be included in other groups are represented in a separate group. This group consists of Ner2 and Ner28 (212 µm) samples peaking in between the second and third group, and Ner41 (300 µm) samples representing the coarsest grain size. As in the third group, all samples of the fourth group belong to the western channel.

Considering the locations and grain size distribution tables of the samples taken from the study area, it was concluded that the eastern channel is represented by finer-grained sediments and the western channel is represented by relatively coarser-grained sand sediments.

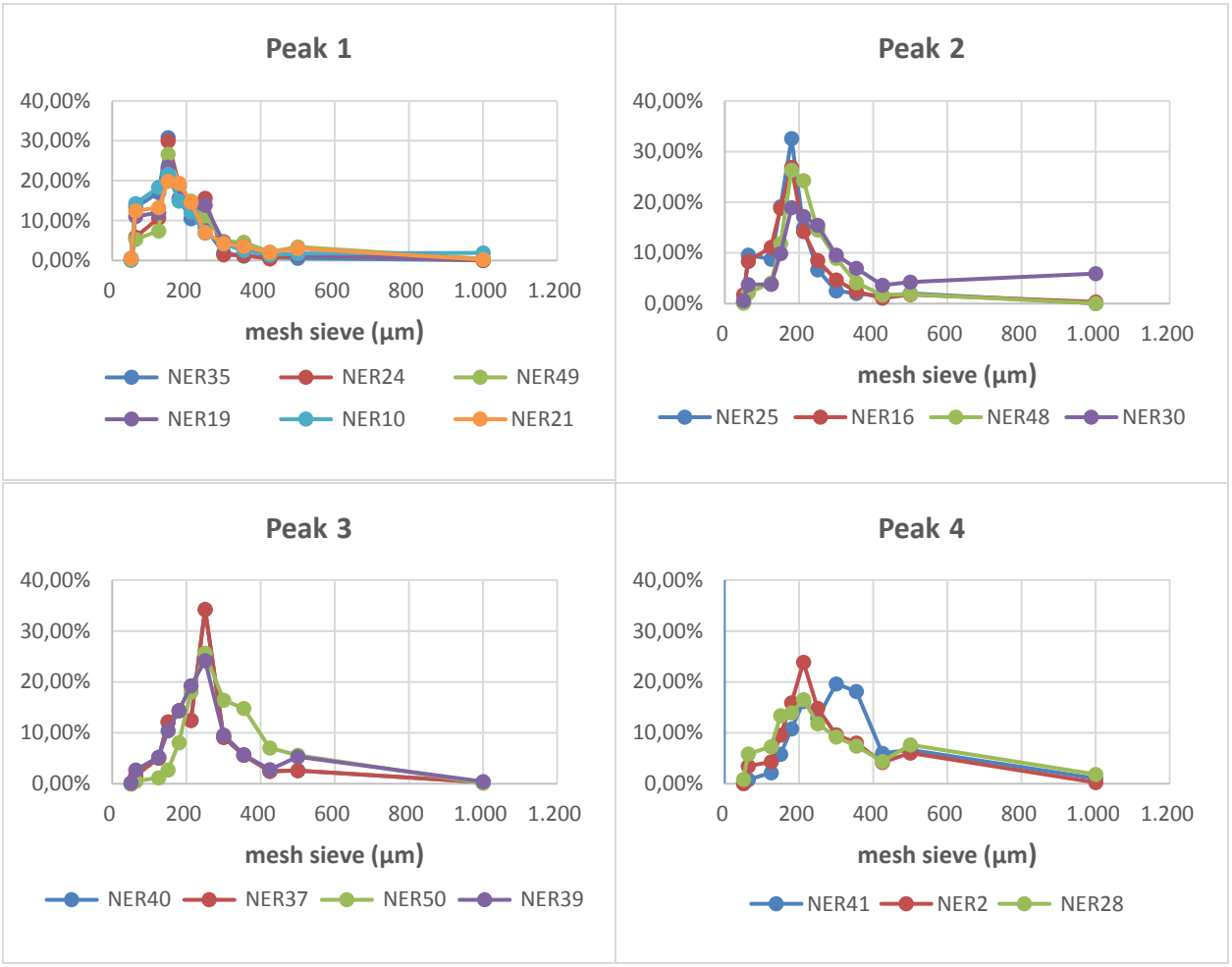

Fig. 14. Four different peak groups of the sediment samples. The first, second, third sediment groups peak at 150 µm, 180 µm, 250 µm respectively. In the fourth group, Ner41 peaks at 300 µm, Ner2 and Ner28 peak at 212 µm.

3.5 Current meter measurements

The current meter is an instrument that measures and calculates underwater parameters such as current speed, temperature, tide pressure and tide levels. In this study, SeaGuard recording current meter (AADI, Norway) consisting of the main unit (with an SD card), and a Doppler current sensor was used. More additional sensors can be implemented to the instrument to get more information about the water properties. In our case, a CTD (conductivity-salinity, temperature, and depth) and a tide sensor (measures the tide level) was implemented to the current meter.

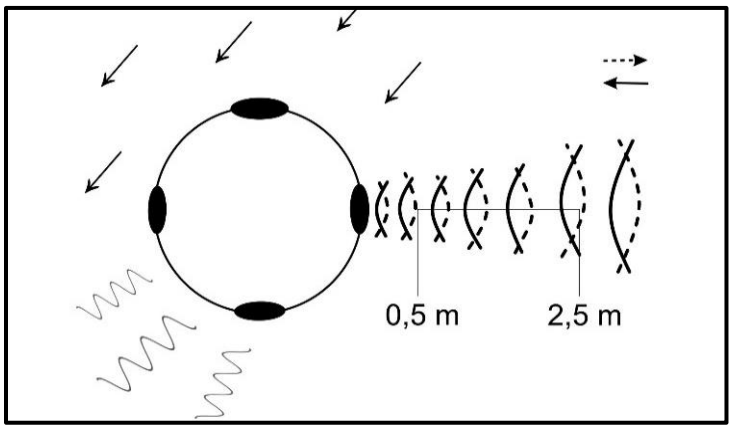

Fig. 15. Arrows show the current direction, the big circle illustrates the top view of the doppler current sensor. Turbulence is demonstrated with freeform (scribble) on the backside of the instrument. Four dots are illustrating the positions of the transducers/receivers. Dashed and straight lines indicate the direction of the transmitted and received signals, respectively.

The current sensors are based on the backscatter acoustic Doppler principle (Merckelbach, 2006) The sensor has four acoustic transducers (beams), and it sends out acoustic pulses with a 2 MHz frequency as a default value. Ideally, only the front two are activated to minimize turbulence that might occur behind the transducers (Fig. 15). Before the acoustic waves are transmitted, the travel time, travel distance, and strength values of the pulses are calibrated by pre-setting the values in the main unit.

The device allows parameters to be presented directly in engineering units without the need for external calculations, as raw data and calibrations are stored within algorithm-coded sensors. The current speed and direction are calculated by transmitting the acoustic pulses and sampling the number and strength of the backscattering signal at a specific distance from the sensor. Backscattering gives information about the reduction of the signal received compared to the intensity of the signal transmitted which allows the residual concentration to be measured. Tide levels above the sensor are calculated by measuring the absolute pressure (hydrostatic pressure - atmospheric pressure) at installation depth.

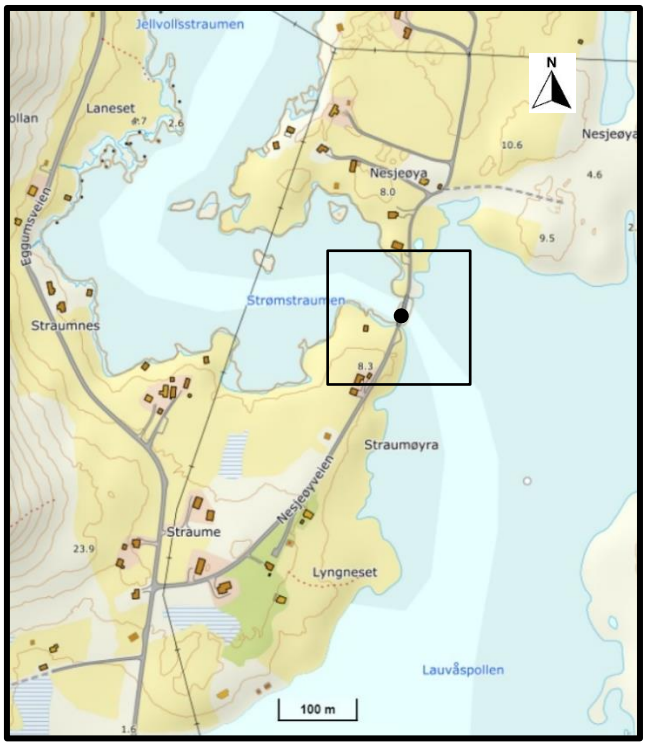

Fig. 16. Deployment location of the current meter is indicated with black dot inside the box.

To capture the changes in the water parameters, the instrument was hung down by a rope from the bridge, at the narrowest area of (9 m) (68°16'57.5" N 13°43'46.4" E) the Strømstraumen (Fig. 16), where the changes in current speed were most significant between Jellvollsstraumen and Lauvåspollen. Acoustic signals with a 2 MHz frequency were set to be recorded with a proximity of ~0.5-2.5 m to the instrument. The water depth was ~1,5 m (± 0.5m high and low tide) and the current meter was deployed ~0.3 m above the bottom. ~20 kg of weight was attached to the bottom of the current meter to stabilize it and to prevent possible tilting errors. The current meter was deployed for a total of six days between 16.08.2020-22.08.2020 and received 8795 records during this period.

Results from the current meter between 16.08.20 17:00 and 18.08.20 17:00 are displayed in Figures 17 and 18. According to average values from the instrument, water flows in the southeast direction at an angle of ~120° at flood tide and in the northwest direction at an angle of ~300° at ebb tide (Fig. 17). Absolute speed values are maximum in flood tide with 170 cms^{-1} and minimum in ebb tide with around 90 cms^{-1} in the specified period.

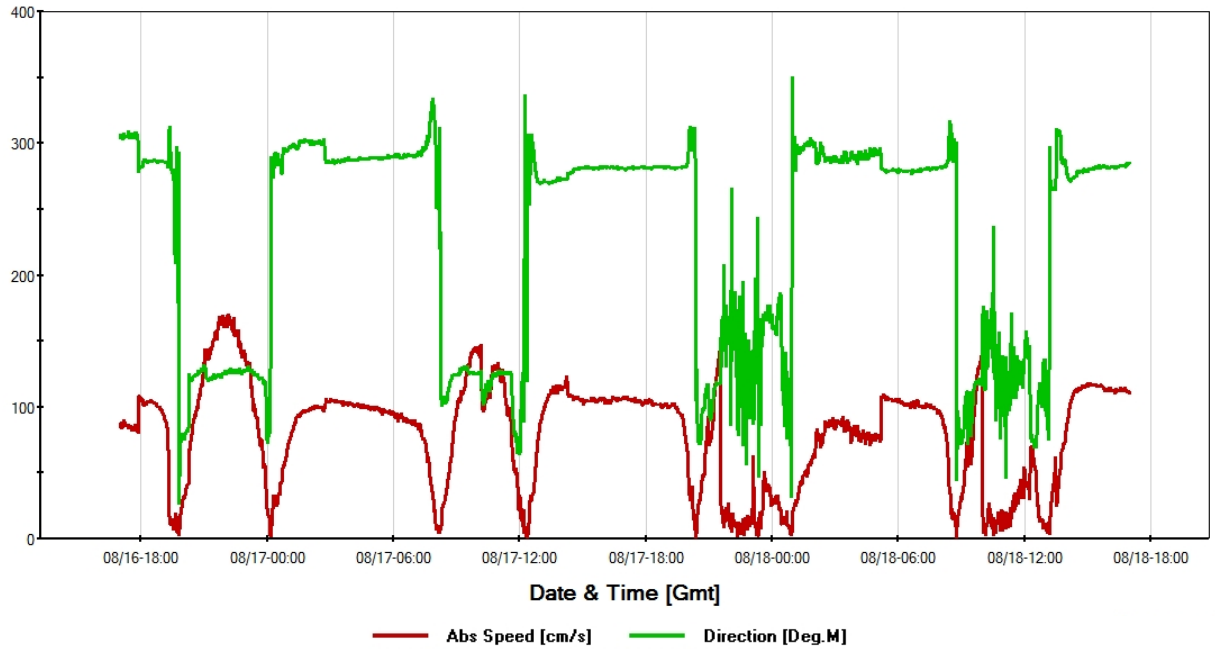

Fig. 17. Absolute speed and direction values from the current meter.

Salinity measurements are consistent with the absolute speed values and water directions. As the salty tidal seawater moves inland, the salinity continues to increase at the point where the current meter was deployed and peaks at 33 ppt (Fig. 18). Salinity is measured around 24 ppt and shows a small decrease during ebb tide.

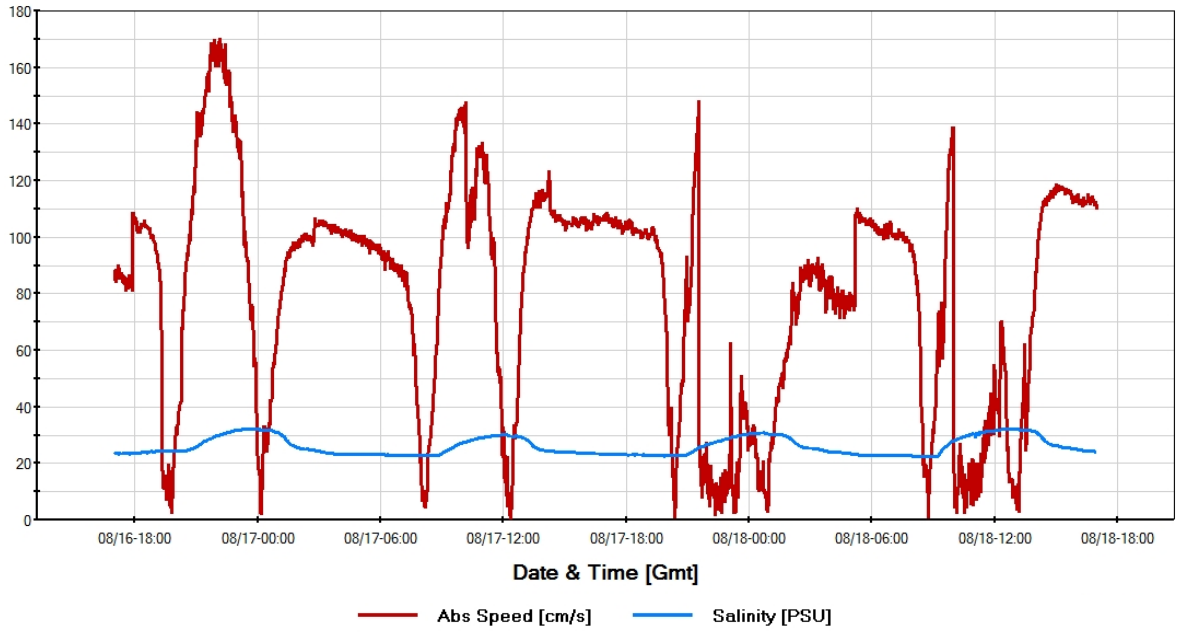

Fig. 18. Absolute speed and salinity values from the current meter.

3.6 Water level measurements

HOBO U20L-02 automatic water level logger was deployed in Lauvåspollen, Ytterpollen, and Innerpollen to monitor the water level changes in the tidal basins. This instrument, which has a highly durable housing system and a protective end cap, has pressure sensors made of ceramic (Onset Computer Corp., n.d.). The measurement was started on 07.01.2021 and stopped on 23.03.2021 due to full memory. The loggers were set to measure every 5 minutes which allowed them to operate for 75 days. The locations of the deployment points and the logging times are indicated in Table 2.

Table 2 Position, deployment time, and water level measurement at the time of deployment of the pressure sensors.

Place	Approximate coordinates (Land-point)	Time (GMT+1)	The water level at the time of deployment
Lauvåspollen	68º 16.64' N 13º 43.39' E	15:27	0.6 m
Ytterpollen	68º 15.57' N 13º 48.01' E	15:48	1.0 m
Innerpollen	68º 16.63' N 13º 51.08' E	18:34	0.8 m

For configuring and analysing the pressure sensor recordings, the HOBOware program is used. Absolute pressure (kPa), temperature (°C) and density (kgm^{-3}) data were retrieved from the loggers. To calculate the water level, the formula below was used.

$$Water\ level\ pressure\ =\ absolute\ pressure\ -\ air\ pressure$$

$$Water\ level\ =\ \frac{(water\ level\ pressure\ (kPa)\ *\ \rho_{avr})}{(1000\ *\ g)}$$

Where:

Air pressure	:	101.325	[kPa]
g	:	9,81	[ms^{-2}]
ρ_{avr}	:	1018,848	[kgm^{-3}]

The water levels calculated from the pressure sensor measurements of the three tidal basins and the calculated tide values for the sea from the Andenes (closest station to the study area) are shown in Figure 19. Calculated tide from Andenes which is adjusted by -5 minutes and altitude factor of 1.01 (Kartverket, n.d.-b) are included in Figure 19 to better understand the changes in water levels as they move from the sea to the inner basins.

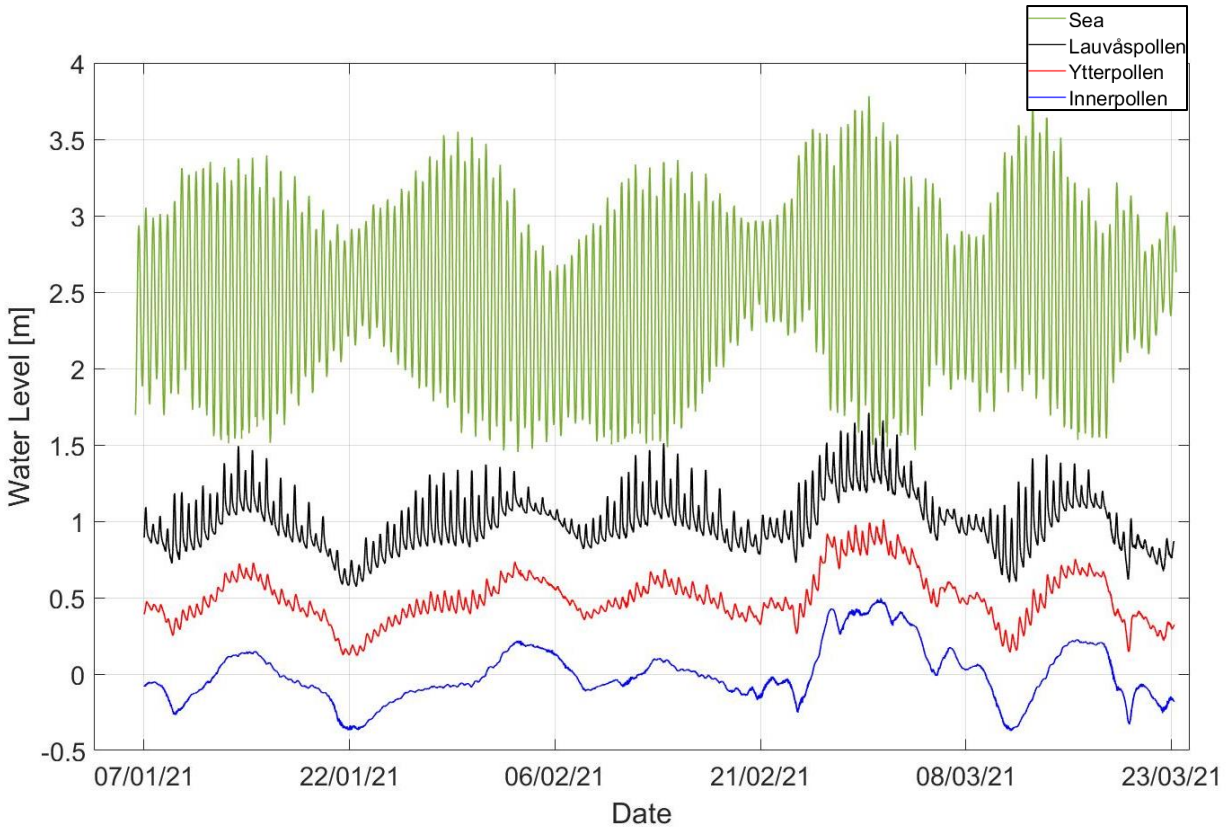

Fig. 19. Tide values from Andenes (Kartverket, n.d.-b) and water level measurements from Lauvåspollen, Ytterpollen, and Innerpollen. For the measurements from three basins, the water level is averaged for each location and plotted to the zero line. At the vertical reference level, the time series are separated by 0.5 m to see the changes more clearly. The time series of sea observations are separated by 1.5 m from Lauvåspollen on the vertical axis.

Figure 19 shows that the daily tidal level variations are diminishing from the sea to Innerpollen. The highest reduction occurs when the tides enter Lauvåspollen from the open sea. Based on the water level measurements it can be concluded that water transport capacity is limited in the channels. Short-term daily changes are blocked by the narrow and shallow channels, and only the longer time scale variations (>10 day period) with a low amplitude travel to Innerpollen without tidal choking. Therefore, 14 days of large-scale water transport capacity is sufficient in the channels to fill and empty the basins, while the daily tidal capacity is limited due to tidal chocking in small-scale channels.

Water levels are illustrated for three days from Lauvåspollen to understand how tidal waters are affected as they move through the system (Fig. 20). Tidal waters show an asymmetrical curve with sharply rising levels of the flood tide, and slowly decreasing levels during the ebb tide. This deformation of tidal waters can be explained by the bottom friction that develops due to the very shallow and narrow geometry of the channels. Sediment transport is an exponential function of water velocity indicating that more sediment moves in during flood tide than what moves out during ebb tide. Therefore, the pattern of flood velocities being much higher than ebb velocities makes the system flood dominated. One tidal cycle lasts approximately 12 hours 41 minutes where the flood period takes ≅ 3 hours 48 minutes and the ebb period takes ≅ 8 hours 34 minutes (Fig. 20). This means that the ebb duration is more than double the flood duration, and measured flood velocities are more than double the measured ebb velocities (Fig. 20).

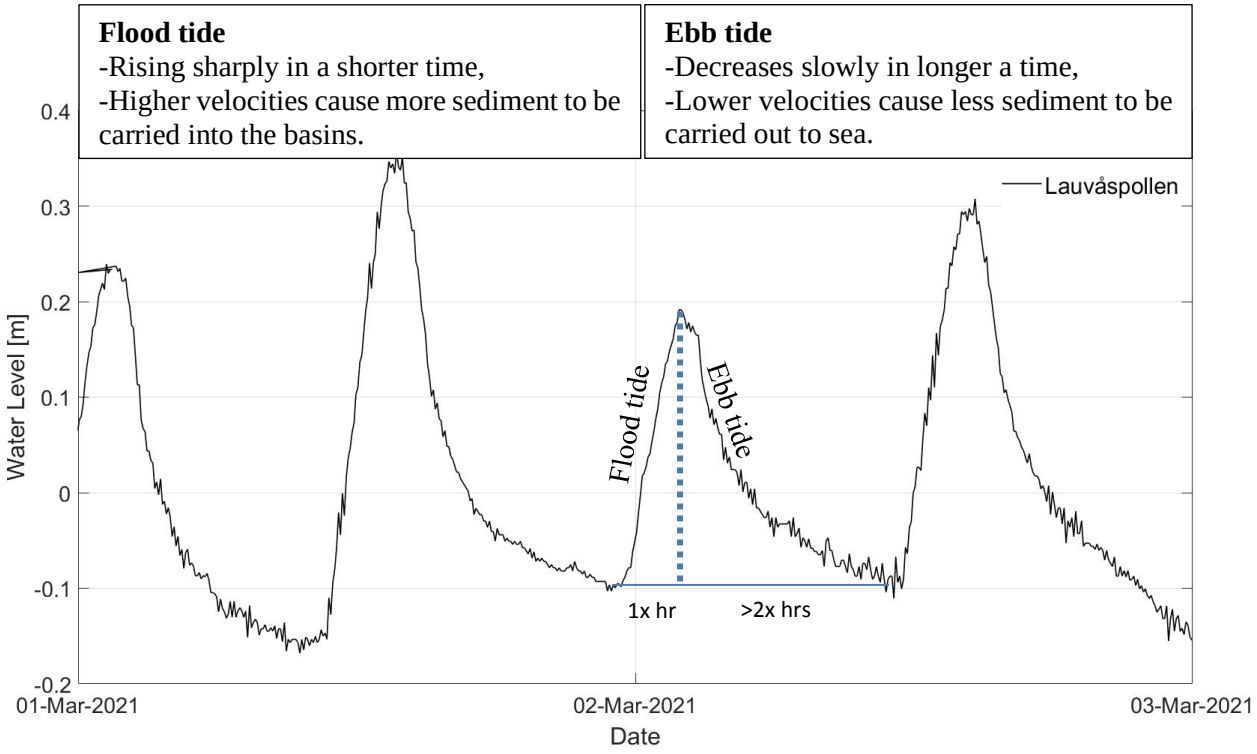

Fig. 20 Water level records from Lauvåspollen for three days. The averaged water level values are drawn on the zero line on the vertical axis.

4. Computational method

The computational method, as introduced in Chapter 3.1, is the second method used in this thesis. A computational process-based morphodynamic model is used to numerically study the behaviour of the tidal system. In this chapter, the model is described, and parameters are introduced.

4.1 Model description and setup

In this research, the numerical model FINEL2d which is developed by Dutch company Svašek Hydraulics is used to be able to understand the long-term morphologic and hydrodynamic changes in the tidal system. The long-term is defined here as a scale of 10 years based on the reaction time of the system to possible effects/changes. There are different types of morphological models based on different model approaches such as observation-based models (data-based models, empirical relationships), and process-based ones (de Vriend, 1996). Observation-based models use an underlying assumption that the determining processes will remain constant, and the modelling is based on the measurements (de Vriend, 1996). In process-based modelling, the physical principles such as energy and mass conservation are calculated with mathematical equations to describe flow conditions, water level, sediment transport, bed level changes, etc. (de Vriend, 1996). Process-based modelling is also called bottom-up modelling as it starts with small processes in water, such as small currents, in every part of the model. Based on this information, it calculates the sediment transport in each cell and then uses this information to calculate the larger morphology. This type of modelling, which goes from small to larger scales with small time steps, is used in this thesis. The reason behind choosing the process-based modelling is that in the range of available models, it is the only model which can potentially describe morphological changes in a real case study with sufficient spatial details. In addition, the model can be run with different scenarios, e.g., to look at the effects of dam (barrier) removal.

The 2D depth-averaged numerical model is based on the finite element method, which is a method of spatial discretization of the domain into a set of finite elements (Vreugdenhil, 1994; Dam et al., 2013). The benefit of such a model is that the effect of measures can be modelled by systematically turning the human interventions on and off in the model. The region is divided into several basic elements in an unstructured triangular shape, called finite elements, to be able to systematically

generate the approximation functions. The reason behind the choice of an ‘unstructured triangular grid’ structure is that it can provide more accurate solutions, especially in complex regions since the resolution can be adjusted in desired locations. The triangular grid generation in the finite element method allows applying high resolution in the focused study area and low resolution in further, less important areas (Kroon et al., 2016). The unknowns in any point are approximated linearly by calculating the values at the centre of the triangles which allows defining the unknowns in the entire region by a sum of piecewise continuous linear functions.

Water motion, sediment transport, and bed evolution can be seen as a coupled system that forms the basis of process-based modelling (Fig. 21). The program calculates the flow conditions as a first step, then determines the sediment transport accordingly. The flow speed is the determining factor for the amount of sediment transport according to the used sediment transport formula. Faster water flows provide an exponential increase in sediment transport. Before the next time-step calculation of the new flow conditions, the bed level of each computational cell is updated by the program. The numerical time step of the model is chosen automatically by the model to ensure numerical stability.

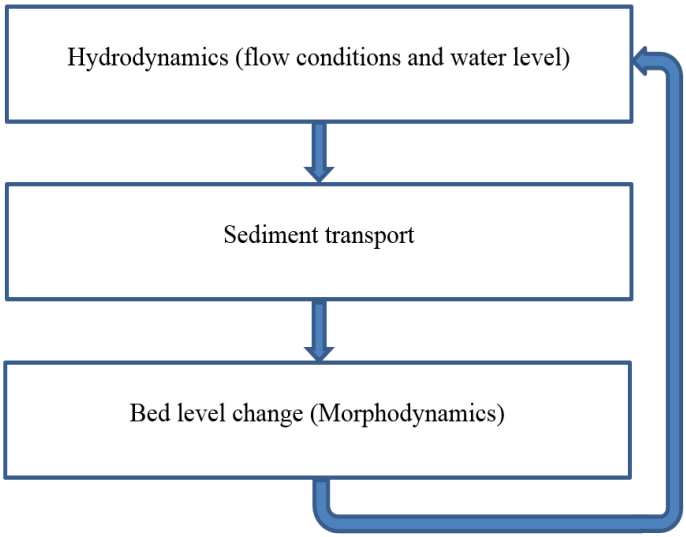

Fig. 21: Illustration of model flowchart.

Governing equations for the hydrodynamic conditions are described with ‘depth-averaged shallow water equations that form the basis of the flow module (Dam et al., 2007). According to Vreugdenhil (1994), shallow-water flows are characterized by a much smaller vertical dimension than typical horizontal scales; flows are nearly horizontal, therefore, the mathematical formulation

and numerical solution in shallow-water flows can be simplified by assuming the pressure distribution to be hydrostatic. Therefore, the equations can be averaged over depth and shown as a 2-dimensional model which can provide the essential information with much lower costs (Vreugdenhil, 1994). The depth-integrated shallow water equations are derived from Navier-Stokes equations which describe the conservation of mass and momentum (Vreugdenhil, 1994; Dam et al., 2007).

The model equations are continuity equations:

$$\frac{\partial h}{\partial t} + \frac{\partial uH}{\partial x} + \frac{\partial vH}{\partial y} = 0$$

The momentum balance in x-direction:

$$\frac{\partial Hu}{\partial t} + \frac{\partial Hu^2}{\partial x} + \frac{\partial Huv}{\partial y} - fHv + gH\frac{\partial h}{\partial x} - \frac{1}{\rho}\tau_{x,b} + \frac{1}{\rho}\tau_{x,w} + \frac{1}{\rho}\tau_{x,r} = 0$$

The momentum balance in y-direction:

$$\frac{\partial Hv}{\partial t} + \frac{\partial Huv}{\partial x} + \frac{\partial Hv^2}{\partial y} + fHu + gH\frac{\partial h}{\partial y} - \frac{1}{\rho}\tau_{y,b} + \frac{1}{\rho}\tau_{y,w} + \frac{1}{\rho}\tau_{y,r} = 0$$

In which:

$$H = h + z_b$$

Where:

u	=	depth-integrated velocity in x-direction	[m/s]
v	=	depth-integrated velocity in y-direction	[m/s]
h	=	water level	[m]
z_b	=	bottom level (positive downwards)	[m]
H	=	water depth	[m]
f	=	Coriolis coefficient	[1/s]
g	=	gravitational acceleration	[m/s^2]
ρ	=	density of water	[kg/m^3]

τ_b	=	bottom shear stress	[N/m^2]
τ_w	=	wind shear stress	[N/m^2]
τ_r	=	radiation stress	[N/m^2]

In addition to the hydrodynamic module, the sediment transport module is used as a second step to find the tidal morphodynamic development over time. The Engelund and Hansen (1967) sediment transport formula for the sand bed rivers is assigned for the sediment transport module. In this module, the amount of transported sediment is calculated per grid cell based on the velocity.

Sediment balance formulation for the evolution of the bed level used in the model:

$$\frac{\partial z_b}{\partial t} + \frac{\partial q_x}{\partial x} + \frac{\partial q_y}{\partial y} = 0$$

Where:

z_b	=	bed level	[m]
q_x	=	components of the sediment flux in x direction	[m^2/s]
q_y	=	components of the sediment flux in y direction	[m^2/s]

Since it is assumed that most of the sediment transport is suspended transport, the method of Galappatti and Vreugdenhil (Galappatti & Vreugdenhil, 1985) is used in the model which is a calculation of dimensionless equilibrium concentration:

$$c_e = \frac{S_s}{H\sqrt{u^2 + v^2}}$$

Where:

c_e	=	equilibrium concentration	[-]
S_s	=	the magnitude of suspended equilibrium sand transport	[m^2/s]

The depth-integrated suspended sediment concentration is then calculated from:

$$\left(\frac{\partial c}{\partial t} + u\frac{\partial c}{\partial x} + v\frac{\partial c}{\partial y}\right) = \frac{1}{T_c}[c_e - c]$$

In which:

$$T_c = \frac{H}{w_s}$$

Where:

c	=	the depth averaged suspended sediment concentration	[-]
u, v	=	horizontal velocities	[m/s]
c_e	=	the equilibrium sediment concentration	[-]
T_c	=	characteristic time scale	[s]
H	=	the water depth	[m]
w_s	=	sediment settling velocity	[m/s]

Several phenomena affect the distortion of the tidal wave and have an effect on net sediment transport. While tidal waves propagate from the open sea into shallow waters, the sinusoidal shape of the wave can be distorted by the effect of shoaling (due to narrowing of the channel cross-section), reflection (due to the sudden obstacle), damping (due to bottom friction), and deformation when they enter systems such as tidal inlets (van Rijn, 2010; Dronkers, 1986). In this case, the frictional effect is dominating since the tide is very asymmetrical and tidal choking is the most dominant process here. With the effect of friction in narrowing channels, flood velocities become higher and ebb velocities lower. This results in more transported sediments during flood tide since the sediment transport is an exponential function of the velocities. This effect of tidal asymmetry on residual sediment transport is also simulated by the simulating software.

In the morphodynamics module, erosion, sedimentation, and bed elevation are dynamically updated on each computational time-step according to the Exner equations (Paola & Voller, 2005). The bed is dynamically updated by calculating the mass change of the bottom sediment, resulting from the sediment gradients, then, mass change is translated into bed elevation change (Elias, 2006).

$$\frac{\partial \eta}{\partial t} = -\frac{1}{1-\lambda_p}\frac{\partial q_s}{\partial x}$$

Where:

η	= bed elevation	[m]
t	= time	[s]

λ_p	= bed porosity	[1]
q_s	= sediment flux	[m^2/s]
x	= downstream distance	[m]

In this coupled system which forms the basis of process-based modelling, the morphological acceleration factor is used. The model calculates each time step of erosion/sedimentation (morphodynamics) then multiplies it by the acceleration factor to speed up the calculation (Roelvink, 2006). When the acceleration factor is low (e.g., 10), the results would be more accurate, however, it would take a longer time to complete the run. In that project 100 is applied as a morphological acceleration factor, which is seen as a reasonable number.

4.2 Model input

To create the model, input is needed for the boundaries, grids, depth, and height. Sea, land, and island boundaries are retrieved from Google Earth Pro (Fig. 22), and the computational grid is generated with a grid-generating script. Tides are defined as the driving force for the model. The model is using astronomical tide from the global TPXO tidal model (Egbert & Svetlana, 2002). Triangles with different resolutions are adjusted on the grid using smaller triangles with greater computational accuracy in more relevant regions, especially in the tidal inlets (Fig. 23). The resolution of the triangles is set to 5000 m^2 at the seaward boundaries and 5 m^2 inside the channels for a higher degree of resolution.

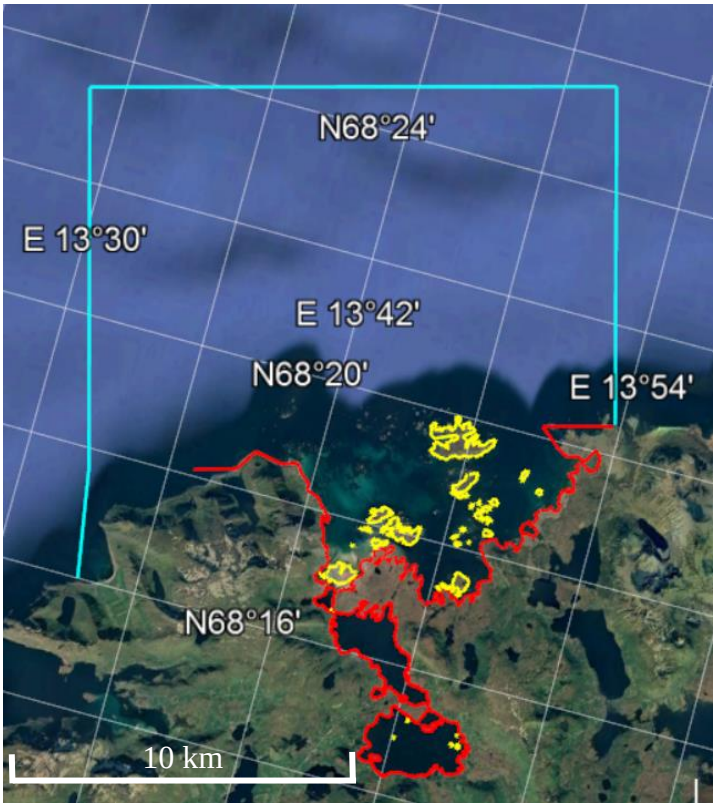

Fig. 22. Grid boundaries. Blue: sea boundary, red: land and yellow: islands.

The areas of triangles between different resolutions are interpolated for a smoother grid by the script. The grid has 18,092 elements (triangles) and the model runtime of 3 days for 10 years on an

Intel Xeon CPU E3-1240 v5 3.50GHz 3.50 GHz processor (1 processor). To make the bottom file, the depth (Dybdedata, n.d.) and the altitude (Høydedata, n.d.) data are used. Moreover, since the LIDAR data (light detection and ranging) from Høydedata (n.d.) cannot see through the water surface, values from Tagged Image File Format (TIFF) are implemented manually for the underwater bathymetry inside the land. Finally, field observations are manually adjusted, and all the bottom files are interpolated in the model grid. The computational grid with bathymetric data is presented in Figure 23.

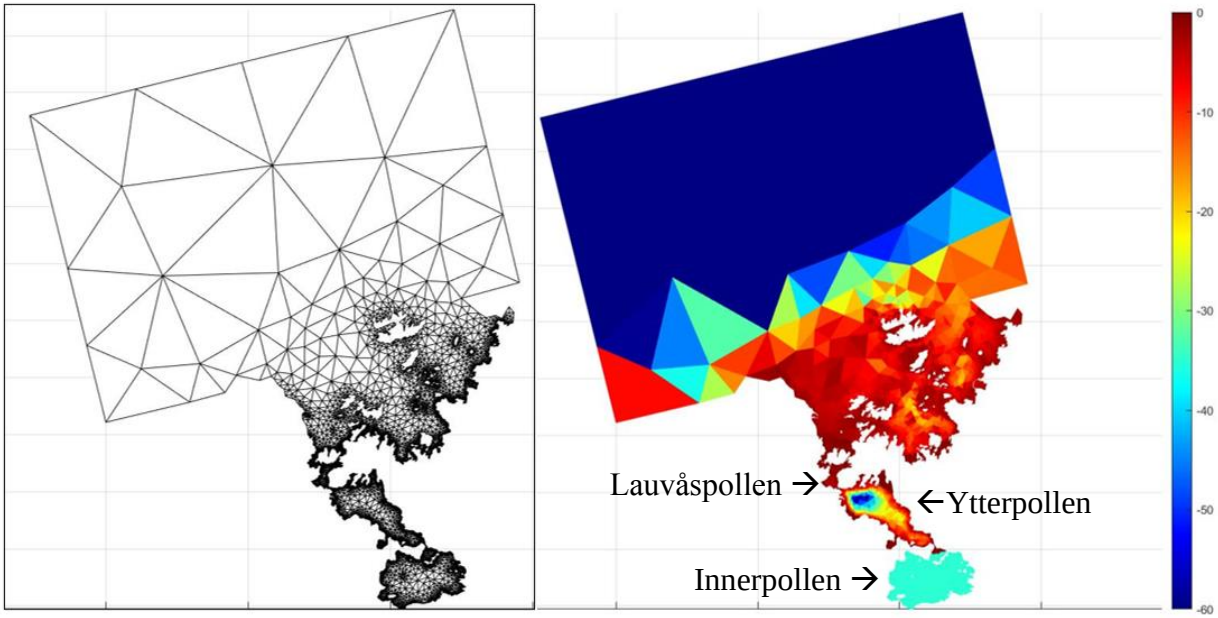

Fig. 23. Computational grid (left) bathymetry (meters) (right)

The change in the depth of the innermost basin, the Innerpollen has a negligible effect on results for the decadal scale (will be discussed in Chapter 6.2). Therefore, the depth of the Innerpollen is assumed to have the same depth everywhere with -30 m.

4.3 Calibration

After all the available data has been inserted, the program needs to be calibrated on the observed water levels. The calibration method of trial and error is used by comparing the simulation output with the measured (observed) data from water level loggers. Each run after various calibrations took between 9 to 18 hours. 16 runs were conducted until the realistic values were reached in the program.

According to the tide values calculated from Andenes adjusted by -5 minutes and altitude factor of 1.01 (Kartverket, n.d.-b), the 1st of March displays the spring tide (maximal tidal range) values during the period covering the deployment time of the water level loggers. Tide values calculated from Andenes showed that the tidal range on the 1st of March was 262 cm where the high-water level reached 244 cm, and the low water level was 18 cm. The model is run for three days (28th of February, 1st and 2nd of March) using the 28th of February as a spin-up time of the model. These dates are used for calibrating the vertical tide and optimizing the global roughness and the depth of the channels. As the model needs one day to spin up the model, only the results of the 1st and 2nd of March will be shown. Multiple runs with different model settings are required for calibration purposes to find the optimal model settings. Calibration is done until the model results are within acceptable accuracy ranges.

4.3.1 Vertical tide

Astronomical tides are the driving force of the model, however, there are external factors that affect the measurements. These external factors such as air pressure and wind can cause a surge in tidal water levels. The wind factor usually has a small effect as the sea is very deep in Norway. Other factors such as air pressure, usually have a greater effect on the tidal water levels in Norway.

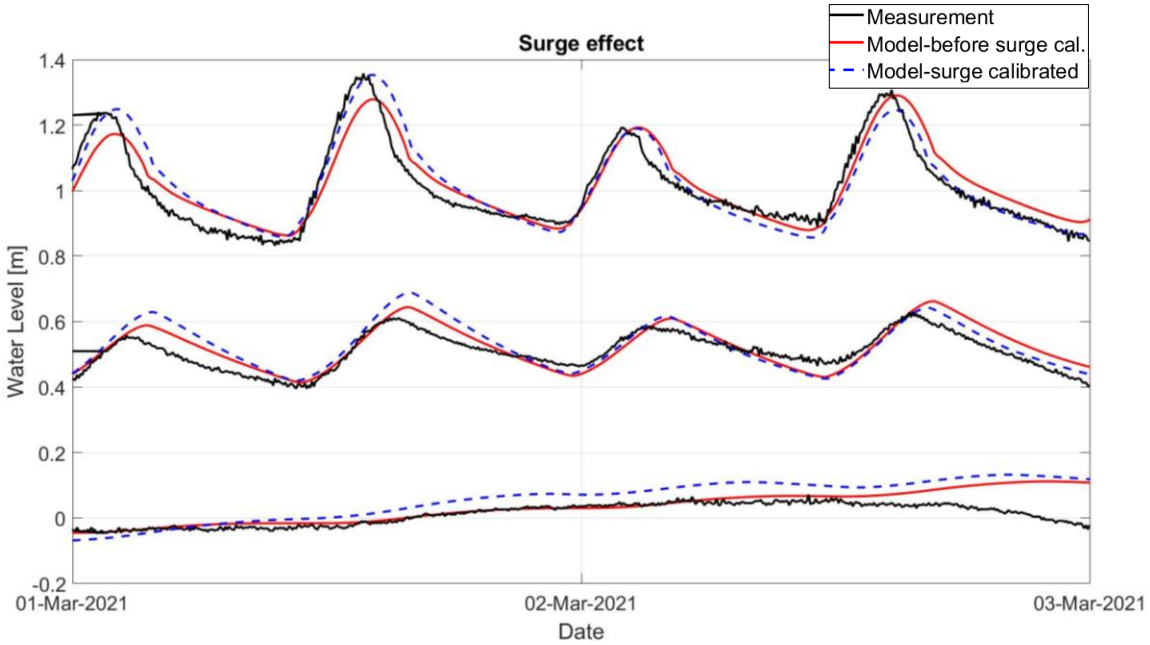

Fig. 24. Surge correction. Water levels from the measurements (black lines), model results before surge correction (red lines) and the calibrated model results (blue dashed lines). The uppermost, middle and lower group of the water levels displays the results from Lauvåspollen, Ytterpollen, and Innerpollen, respectively. At the vertical reference level, averaged water levels are plotted on the zero line and the time series are separated by 0.5 m to see the differences more clearly.

To compensate for the effect of external factors on sea boundaries, the model is run by including the surge values (difference between observed and astronomical tides). The tide values calculated from Andenes (Kartverket, n.d.-b) are subtracted from the astronomical tide and the results are used as an input to calibrate the model on the sea boundary (Fig. 24).

4.3.2 Depth

The results are highly sensitive to changes in depth in the narrow and shallow channels, and it affects the dynamics of the system (Chapter 6.2). The depth is calibrated where the water passes through the western channel (Jellvollsstraumen) and continues over Lauvåspollen via Strømstraumen (Fig. 25). According to different runs with varying depths, the decrease in the depth results in lower water level amplitudes (tidal ranges), while the increase results in higher amplitudes (Fig. 26).

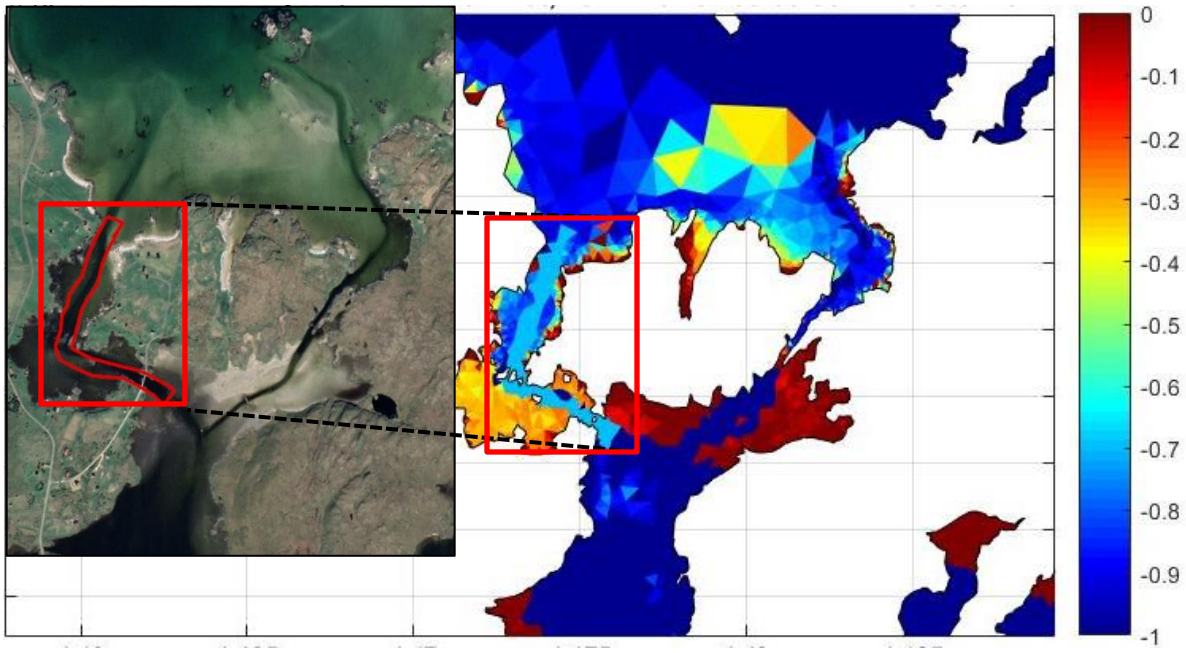

Fig. 25. Location of the deined depth calibration.

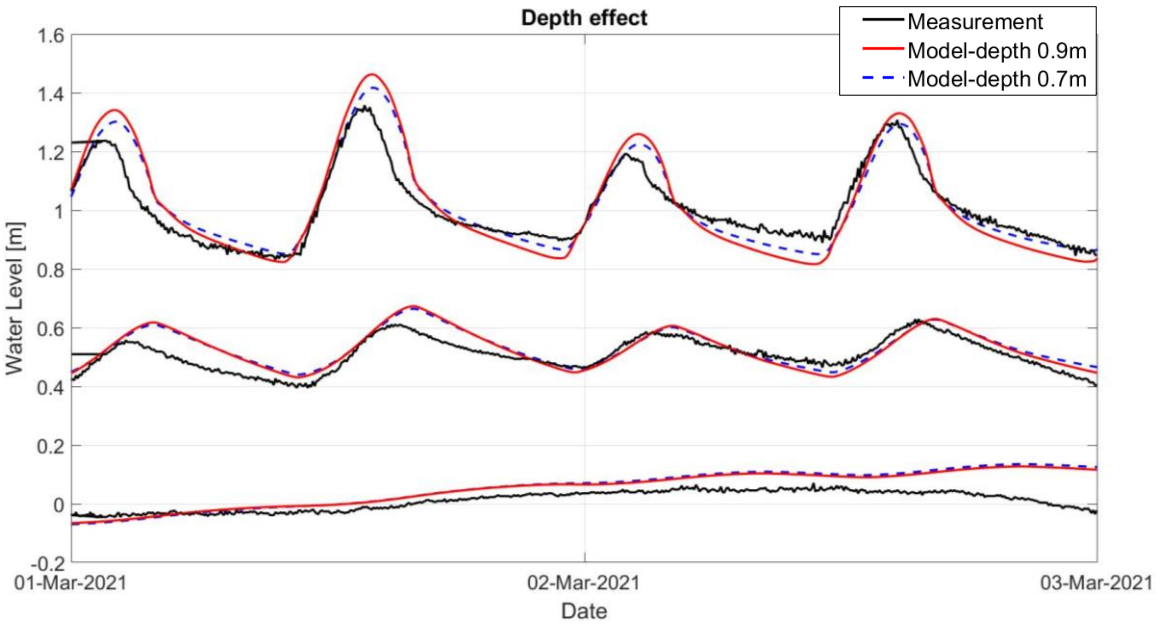

Fig. 26. Depth calibration. Water levels from the measurements (black lines), model results with 0.9 m depth (before; red lines) and the calibrated model with 0.7 m (blue dashed lines). The uppermost, middle and lower group of the water levels displays the results from Lauvåspollen, Ytterpollen, and Innerpollen, respectively. At the vertical reference level, the averaged water levels are plotted on the zero line and the time series are separated by 0.5 m to see the differences more clearly.

Since the exact depth of the channels is largely unknown, the optimal depths in the channels are calibrated in the model. To get the closest results with the measurements from the pressure sensors, multiple depths are adjusted over the channels. This adjustment is done by comparing the water level graphs at the different control points until they aligned as good as possible with the water level measurements.

4.3.3 Global roughness

Another parameter for the calibration is the roughness of the seabed, which is the resistance of the seabed to flowing water. Seabed roughness is relatively unimportant in deeper water than shallow-water coastal regions (Johns & Oguz, 1987) and velocities at the intertidal areas are highly sensitive to the hydraulic bed roughness (Dam et al., 2005). This friction effect between the flowing water and the bottom causes energy loss in tidal waters. An increase in global roughness results in slower water flow and a decrease in wave height (Fig. 27). During calibration runs with different values, an optimal global roughness of 0.1 m is used in the model.

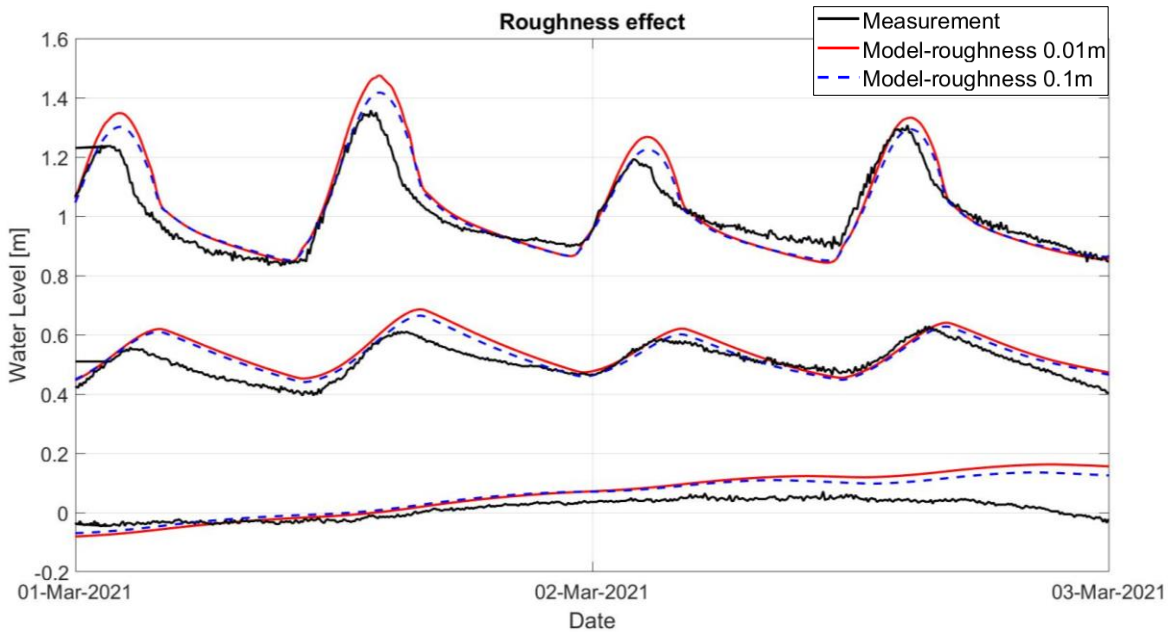

Fig. 27. Global roughness calibration. Water levels from the measurements (black lines), model results with 0.01 m roughness (before; red lines) and the calibrated model with 0.1 m (blue dashed lines). The uppermost, middle and lower group of the water levels displays the results from Lauvåspollen, Ytterpollen, and Innerpollen, respectively. At the vertical reference level, the averaged water levels are plotted on the zero line and the time series are separated by 0.5 m to see the differences more clearly.

5. Scenario runs

With the available calibrated model, it is now possible to do scenario runs. Two different scenarios are defined to investigate the effect of dam removal:

T1: Scenario run with dams (barriers) in place on the eastern side of the channel (current state). This scenario shows how the morphology possibly will be affected in 10 years if the water flow between the open sea and inner tidal basins is blocked by dams. This is a continuation of the present state.

T2: Scenario run without dams in the eastern channel. This scenario shows the changes that can occur in 10 years when the eastern channel is allowed to erode after the dams are removed. It is assumed that the channel can be eroded up to 3 m before hitting a non-erodible layer.

Results of the T1 and T2 scenario runs are presented in the next sections.

5.1 Morphodynamic feedbacks

Figure 28 shows the erosion/sedimentation pattern after 10 years for different conditions for both scenarios. Scenario 1 (T1, present situation) shows limited erosion/sedimentation in both channels after 10 years (Fig. 28A). The highest erosion rate is in the western channel with a depth of 3 m, and the highest sedimentation rate is in the eastern channel with a sediment accumulation of 1 m (Table 3).

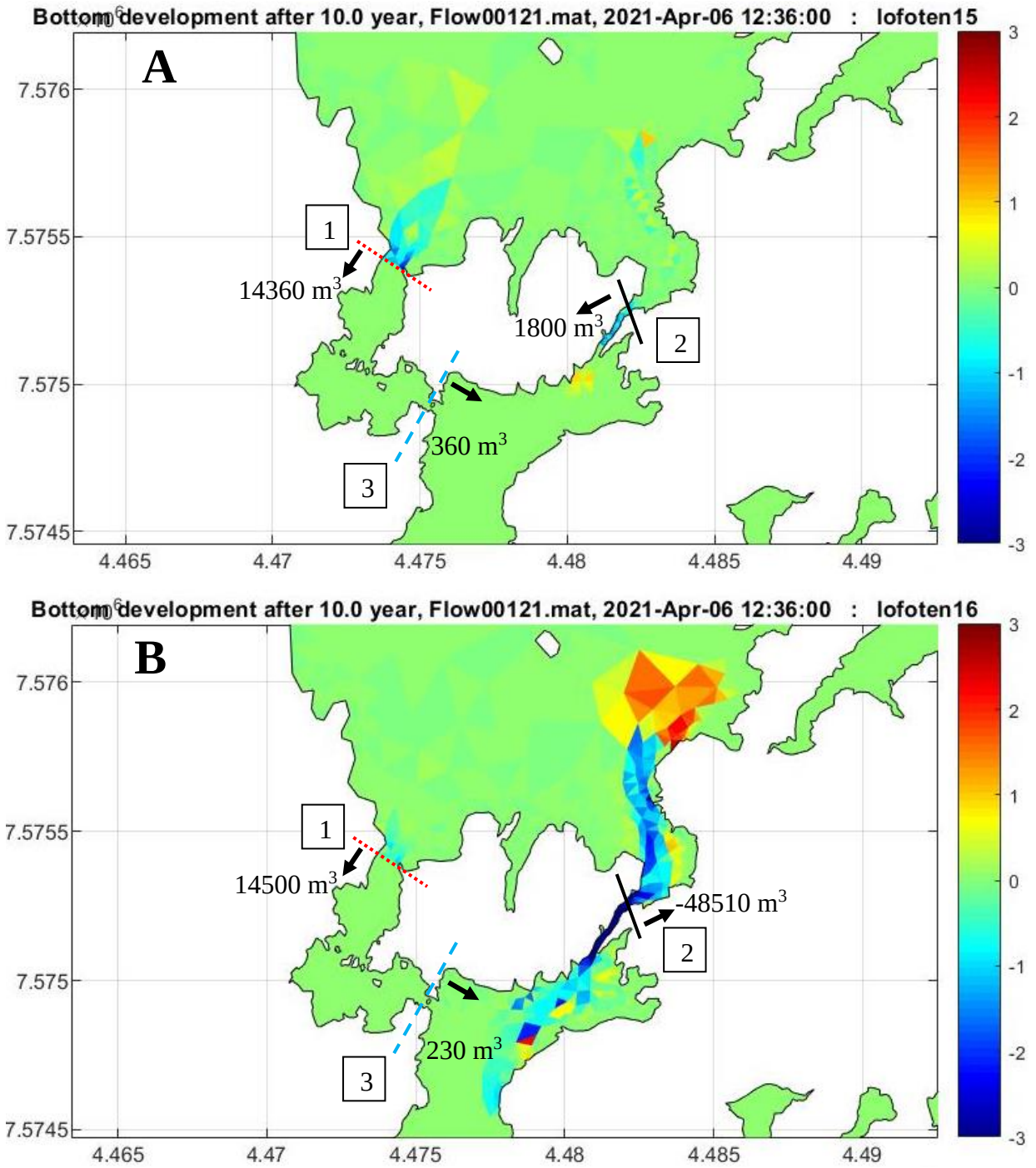

Fig. 28. Sea-bottom difference maps: A. for T1; after 10 years with the current state (with the dams on the eastern channel). B. for T2; after 10 years without dams. Blue colours indicate deepening, red colours shallowing. The dashed red line, black straight line, dashed blue line represents the cross-sections 1, 2 and 3, respectively. Since mass balance is maintained, the volume of erosion equals the volume of deposition across the modelled area. The direction (black arrows) and the volume (m^3) of the cumulative net sediment discharge are indicated in the figure.

In T2, large morphodynamic changes occur as seen from Figure 28 (B). Sedimentation and erosion occur along both channels, with higher rates in the eastern channel. After 10 years, the western

channel is eroded by 1.2 m at the deepest point, and sediment accretion only shallows the sea bottom with a maximum of 0.25 m in a limited area. In the eastern channel, the erosion reaches 3 m (the maximum depth of erosion that can be reached). The eroded sand is moved largely seaward due to ebb currents (Figure 28B), where the deposition (red colour) forms an ebb-tidal delta.

Table 3. Highest values of erosion and sedimentation from the east and west channels. The negative values show the erosion and positive values show the accumulation.

	Simulation 1 (T1)		**Simulation 2 (T2)**	
	Erosion	Sedimentation	Erosion	Sedimentation
Western channel	-3 m	0.5 m	-1.2 m	0.25 m
Eastern channel	-1.5 m	1 m	-3 m	2.5 m

Cumulative sand discharge directions and volumes are indicated in Figure 28 and cumulative sediment discharge plots over 10 years for section 1 and section 2 are represented in Figure 29. For T1, both channels in the east and west predominantly import sediments landward, with higher volumes in section 1 (western channel) (Table 4). The amount of sediment carried in the western channel is higher due to limited erosion in both channels, more sediment presence in larger areas, and lower friction at the bottom.

Table 4. Cumulative sand discharge volumes. Positive values show the net sediment import into the system, and a negative value indicates net sediment export towards the sea.

	Simulation 1 (T1)	**Simulation 2 (T2)**
Section 1 (western channel)	14360 m^3	14500 m^3
Section 2 (eastern channel)	1800 m^3	-48510 m^3
Section 3 (Strømstraumen)	360 m^3	230 m^3

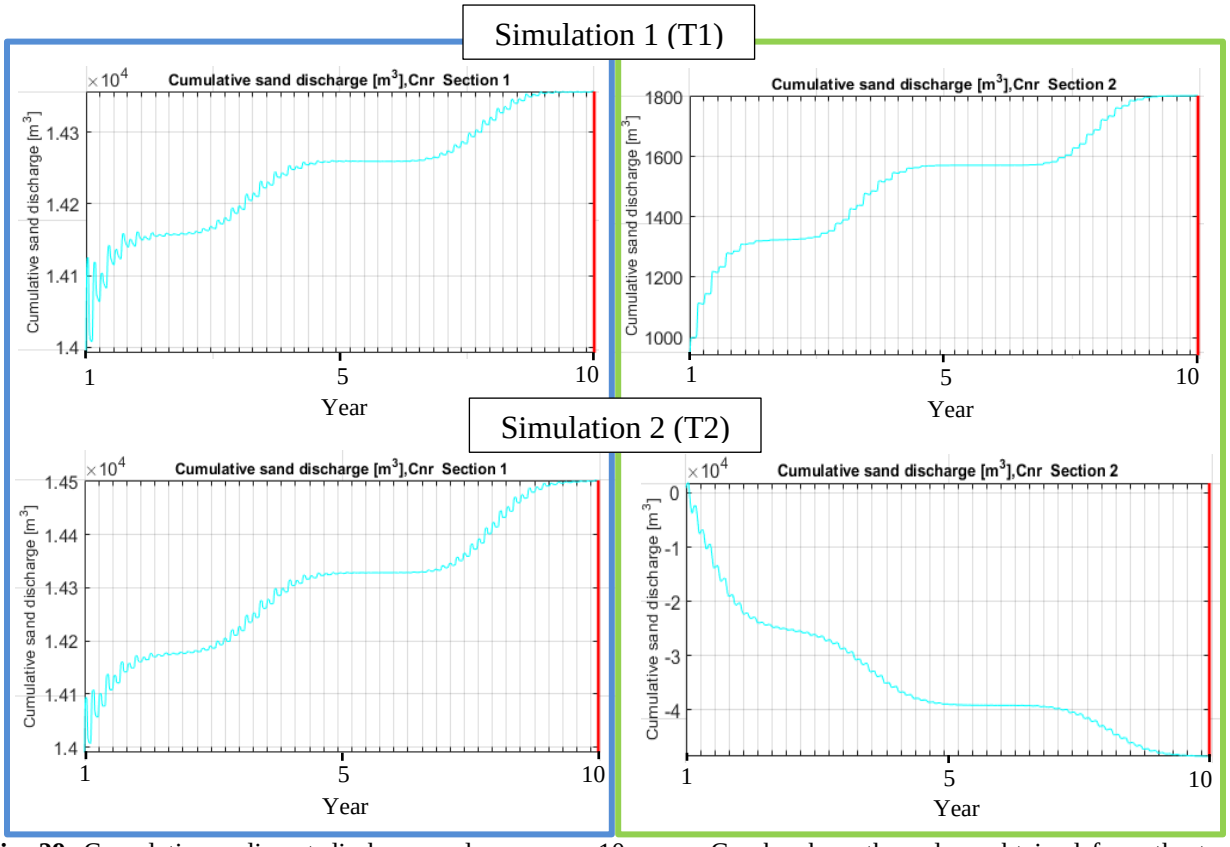

Fig. 29. Cumulative sediment discharge volumes over 10 years. Graphs show the values obtained from the two simulations (T1-T2) for the western channel (blue box; section 1) and eastern channel (green box; section 2). Positive values indicate the net sediment import (to landward) and negative value shows the net sediment export (seaward). The final values after 10 years are indicated in Table 4.

While there was 1800 m^3 of import before, the removal of the dams from the eastern channel has led to a net export of -48510 m^3 of sand in 10 years (Table 4). Section 1 continued to import net sediment into the basin and remained almost with the same value after opening the channel. Figure 28 and Table 4 show that the removal of the dams has a minor morphological effect on section 3.

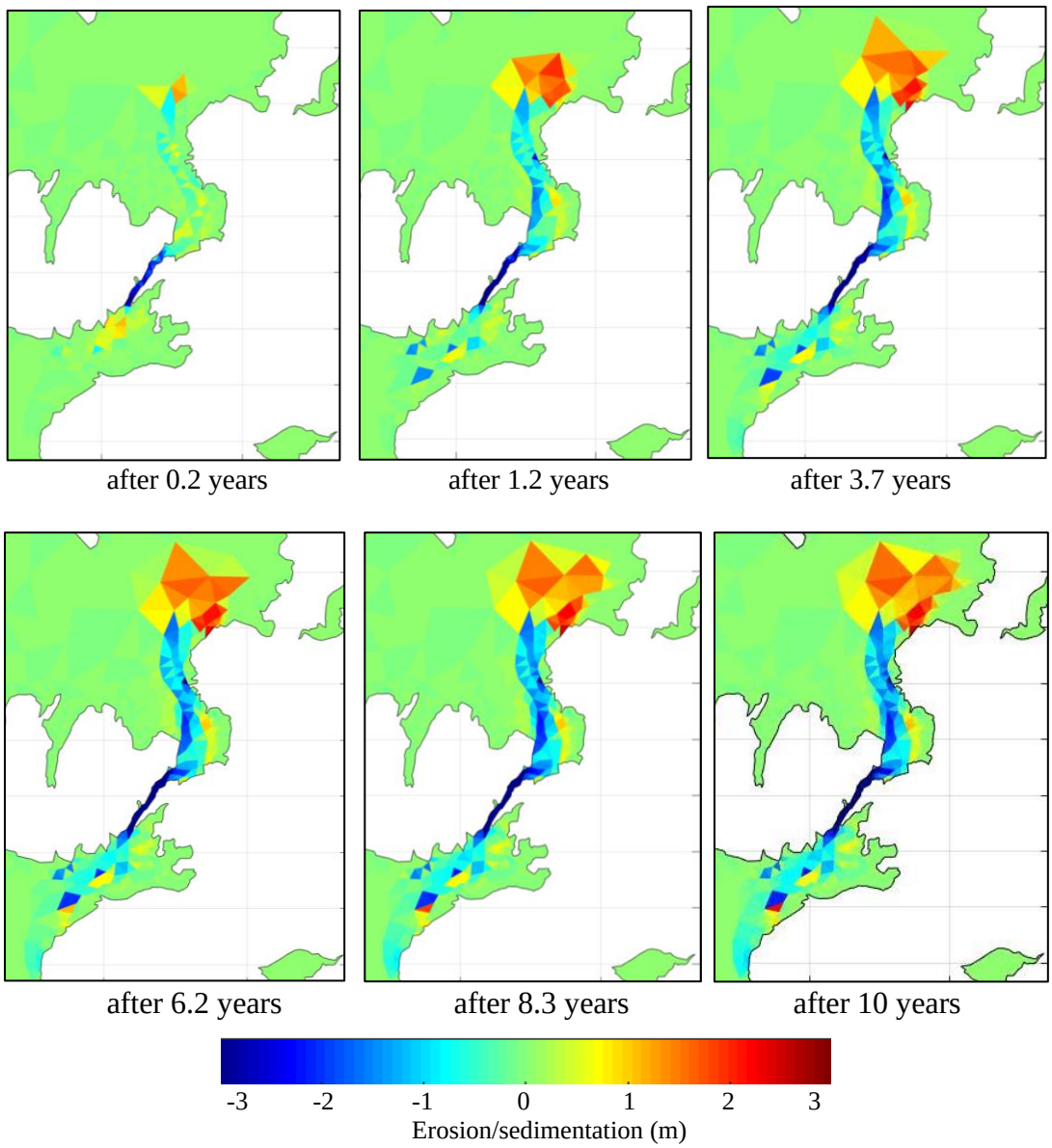

Fig. 30. Morphodynamic processes (sea-bottom difference maps) of the eastern channel for T2 at discrete time-steps over a ten-year period. Erosion/sedimentation (meters); negative values depict erosion; positive values depict sedimentation.

Figure 30 shows that the eastern channel starts to erode quickly right after simulation begins. A large part of the channel reaches its maximum depth (3 m) in a short time (1.2 years) and small flood and ebb-tidal deltas appear on both sides of the channel. After 3.7 years, the deepening almost reaches its final state, while the sedimentation continues at relatively high rates. Sediments continue to accrete and starting to achieve their final shape, but with diminishing rates after 8.3 years. Over time the flood and ebb deltas are enlarged gradually. Especially the ebb tidal delta has grown remarkably due to net seaward transport of sand (Fig 30). However, due to the inaccuracies

in the model settings and processes (Chapter 6.2), there is mainly uncertainty in how fast the eastern channel will erode, but not about the erosion itself. Therefore, after the removal of the dams, the channel is expected to reach it is maximum depth in the order of months to a few years, and the sedimentation is expected to take its final shape, not before 5-10 years.

5.2 Hydrodynamic feedbacks

The comparison of the water level variations in Lauvåspollen and Ytterpollen for both simulation runs (T1, T2) is shown in Figure 31 and Figure 32, respectively. The results from Lauvåspollen and Ytterpollen are chosen to illustrate the hydrodynamic effects because they are the most affected part of the system, and the changes are more distinct compared to Innerpollen. Since the acceleration factor of 100 (which corresponds to 10 years) is used only for the morphological module, the hydrodynamic module runs 100 times slower than the morphodynamic module. Therefore, the hydrodynamic module shows the results for 37 days which covers approximately two neap-spring cycles with a period of 14 days.

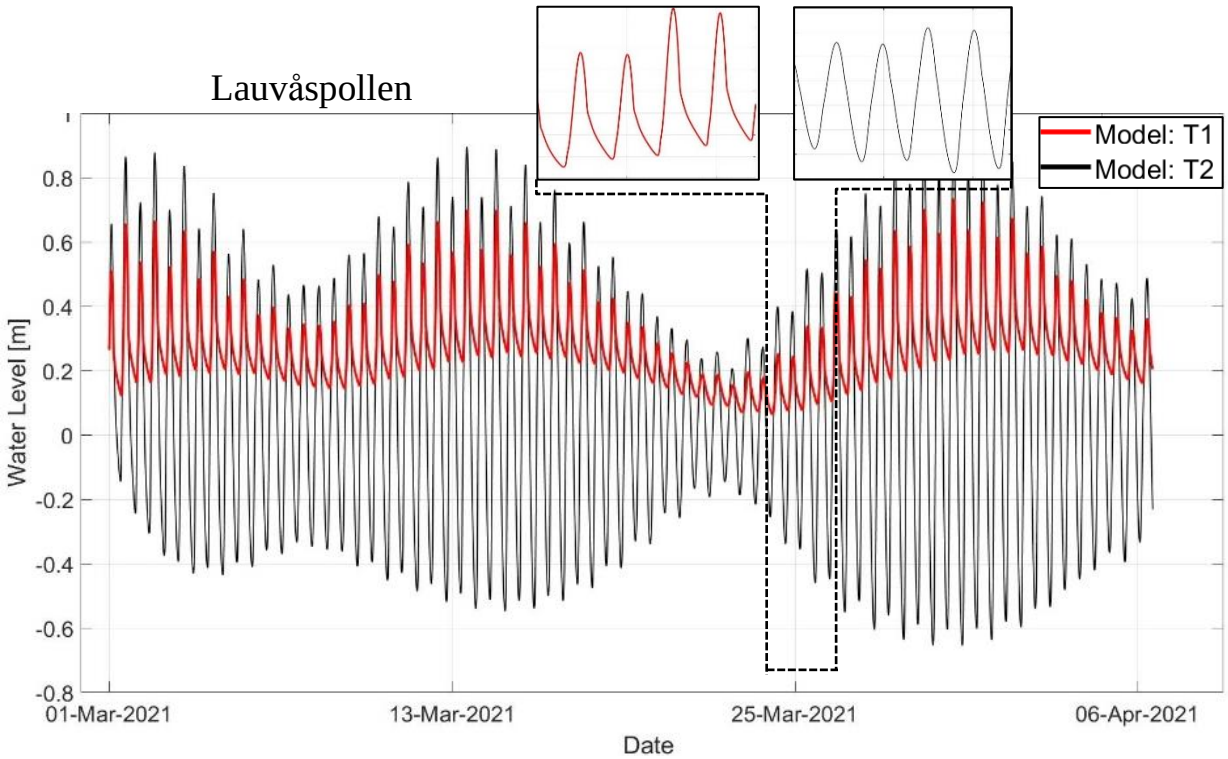

Fig. 31. Variations in tidal amplitudes at Lauvåspollen covers approx. 2 neap-spring cycles with a period of 14 days. The red line shows the amplitudes from simulation 1 (T1) in the presence of dams located in the east channel, and the black line shows simulation 2 (T2) after dams are removed. A section between the 24th of March and 26th of March for both runs is indicated in the figure to show the tidal asymmetry. The averaged water level values are drawn on the zero line on the vertical axis.

In simulation 1 (T1), as the lunar cycle approaches the spring tide, low- and high-water levels rise, and the flood tides become stronger (Fig. 31). The opposite happens when the lunar cycle approaches the neap tide where the high and low waters decrease. Tidal asymmetry is visible from the graph for the whole period (see the insets of Figure 31). Friction at the bottom of the shallow and narrow tidal inlet slows down the tidal current, reduces the amplitudes and delays the current speed, therefore causing a tidal choking (Guo et al., 2018) for T1.

In the second scenario (T2), the eastern channel is quickly eroded, causing less friction at the bottom. This results in an increased exchange of water between the basins and the sea (Fig. 31). Comparing the T2 results to T1 results (Fig. 31), high water levels become higher and low waters become lower during spring tide. The tidal range becomes higher, and the asymmetry is reduced due to less friction in the system (see the insets of Figure 31). Reduction of friction leads to more water moving in and out at the eastern channel with less tidal choking.

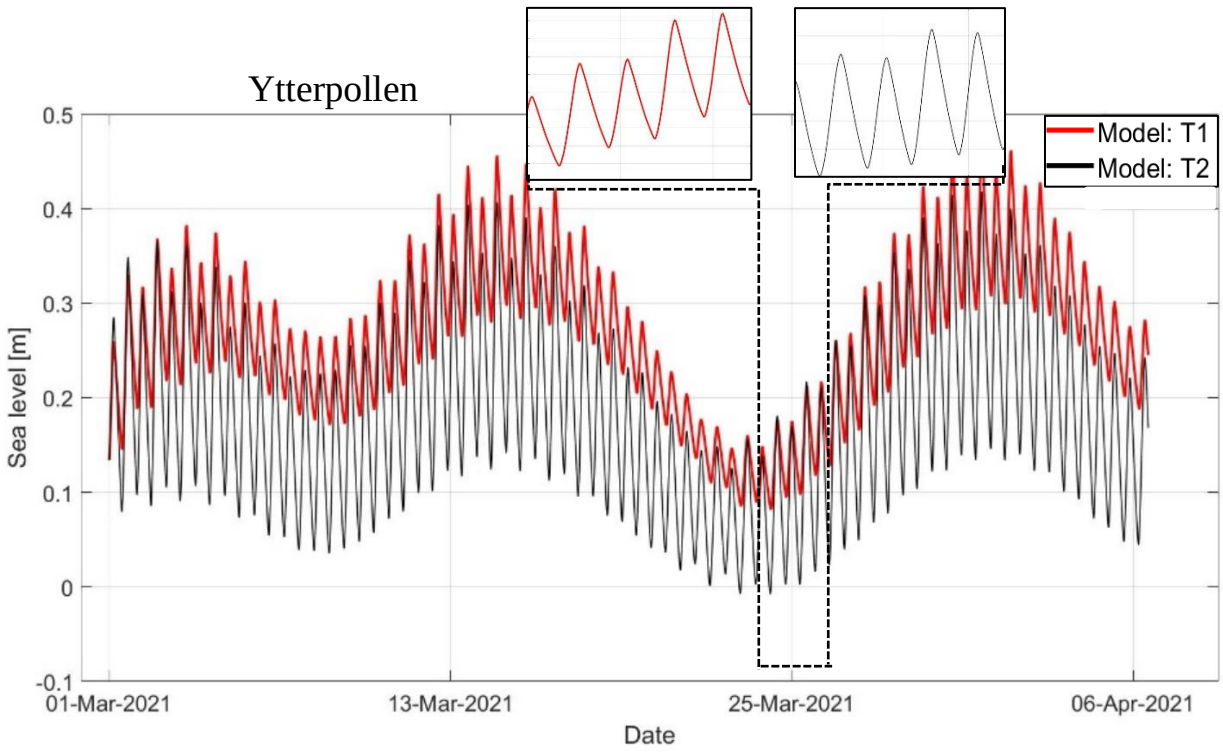

Fig. 32. Variations in tidal amplitudes from Ytterpollen The red line shows the amplitudes from simulation 1 (T1), and the black line shows simulation 2 (T2). A section between the 24th of March and 26th of March for both runs is indicated in the figure to show the tidal asymmetry. The averaged water level values are drawn on the zero line on the vertical axis.

Tidal amplitudes from Ytterpollen are illustrated in Figure 32. In Ytterpollen, the tidal range is further reduced from Lauvåspollen towards Ytterpollen, due to the shallow channel between Lauvåspollen and Ytterpollen (Evjestraumen). Erosion is not expected here as bedrock is visible at the surface in places. Tidal asymmetry in T1 not as strong in Ytterpollen as in Lauvåspollen. The channel between Lauvåspollen and Ytterpollen is cancelling out the strong asymmetry (see the insets of Figure 32). In the model, the bed level is assumed to be non-erodible. Comparing the reduction in water levels from Innerpollen and Lauvåspollen will provide an understanding of the tidal choking phenomenon as water moves towards the inner basins. Figure 33 shows how much the tidal range is decreased due to this phenomenon. In T1, the tidal range drops 79% as the water moves along a narrow and shallow eastern channel towards Lauvåspollen. The model results show that when the dams are removed (T2), this number decreases to 29% as the water can erode the channel (Fig. 33). Therefore, if the barriers are removed, the tidal range in Lauvåspollen will be a factor 3.3 larger than the current situation (42 cm tidal range versus 140 cm tidal range) according to the model results.

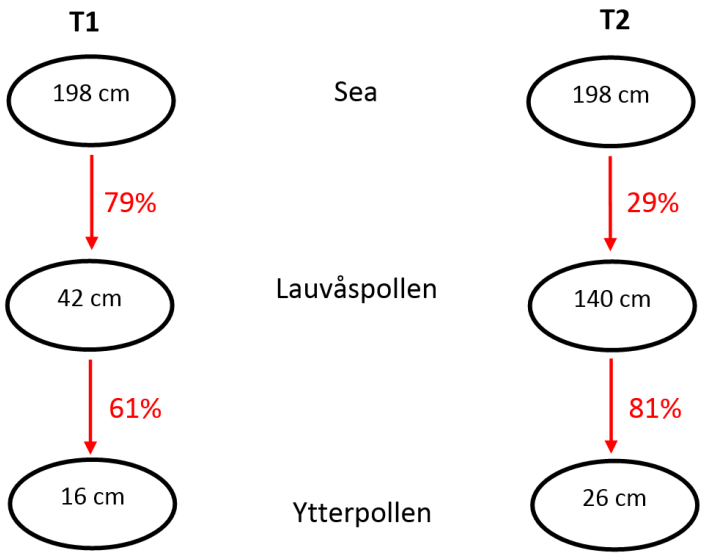

Fig. 33. Tidal range (high tide - low tide) indicating the tidal choking for T1 and T2 scenarios. The observed highest tidal range (13th of March) from the sea (Fig. 19) is used for the calculations. Red values in percentage show the percentage of tidal choking for 'Sea - Lauvåspollen' and 'Lauvåspollen – Ytterpollen'.

The reduction of the amplitude range between the Lauvåspollen and Ytterpollen is showing the opposite pattern where the reduction of the water is higher in T2. Since most of the water is blocked by the first channel, the reduction level is lower in T1 with 61% and much higher amounts of water are blocked by the second channel (Evjestraumen). The tidal range increases here a factor of 1.6 (16 cm versus 26 cm) according to the model results.

6. Discussion

The tidal basin system is like a bathtub with two drains through (channels) which fills (flood-tide) and empties (ebb-tide). When one of the drains (east channel) is blocked, water circulates through the other channel (west channel), filling the bathtub faster than the drain. However, when the second drain is opened, water starts to be exchanged more easily (with less tidal asymmetry) and with much higher amplitudes.

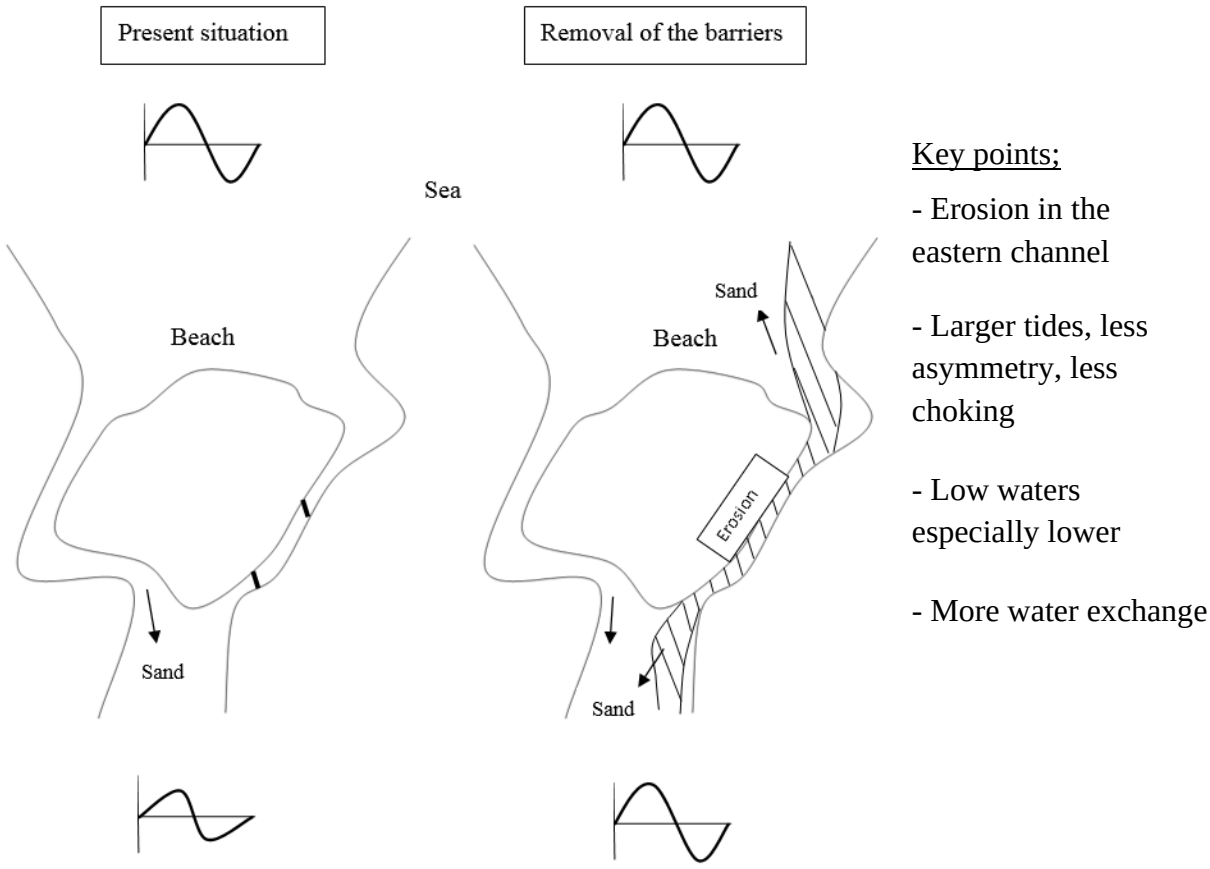

Fig. 34. Simplified sketch for current situation of the dams (left) and after removing the barriers (right). Tidal waves are represented on the seaside (top) and in the basin, after passing the channel (bottom). The main developments that took place after the dam was removed are outlined in the figure.

In a tidal basin, the amount of inflow and outflow volumes is the same (ignoring freshwater input), and the water moves faster at the flood tide due to the geometry and friction of the basin, resulting in an asymmetry in water level and velocity (Fig. 20). With the removal of the dams, the water predominantly uses the eastern channel, where the channel can deepen (Fig. 34). The friction is decreased with the eroding eastern channel, and this decreases the asymmetry. There is a dramatic

increase in the amount of water exchanged between the sea and Lauvåspollen, and a significant decrease at low water levels.

According to aerial pictures and personal interviews with people living there, after the dams had been removed in 1991, the channels quickly eroded and the bottom almost completely dried up during low tide, especially at Jellvollsstraumen. This indicates that the model is capable of producing what was observed in the ’90s when the channel was opened. Therefore, the model is believed to be trustworthy. The largest uncertainty is how deep the eastern channel can be eroded, as the depth of the non-eroded layer is unknown.

In order to project towards the future as attempted in this study, the past and, to a large extent, today's conditions must be studied and understood. The accuracy of predictions and interpretations for the future increases in direct proportionality to this knowledge. There is a lack of studies in the literature on such a glacially sculptured tidal inlet system, and this thesis attempts to introduce new insight to the literature. Resources have also been limited to develop knowledge of the system or compare this study area with other systems. However, as explained in the previous paragraph, obtaining similar results in the model with observational knowledge of dam removal effects in the ‘90s provide robustness to the results. This thesis has provided an established basis for future predictions. To be able to improve the basis, more data will be needed.

6.1 Dominant morphological processes in the study area

Tidal inlets and basins are important and serve many functions for humans, such as having touristic potential, hosting valuable fish ecosystems, and being important as maritime passageways. Because of their value, these areas have often been subject to human intervention through processes such as construction, channel expansion/closure works and mining. In addition to human interventions, tidal basins can be exposed to natural disturbances such as sea-level changes, landslides, avalanches, and flooding. Consequently, the morphology of the tidal basin can be affected, and this will lead to changes in the environmental and socio-economical value of the basin. Therefore, natural disturbances and human interventions must be studied to better understand the morphological development of tidal basins.

Since there are few accessible studies for glacially sculptured tidal inlet systems, morphological processes after human interventions at Wadden sea tidal inlets, where tidal basins are separated by barrier islands, are used as an example case and outlined in the following paragraph.

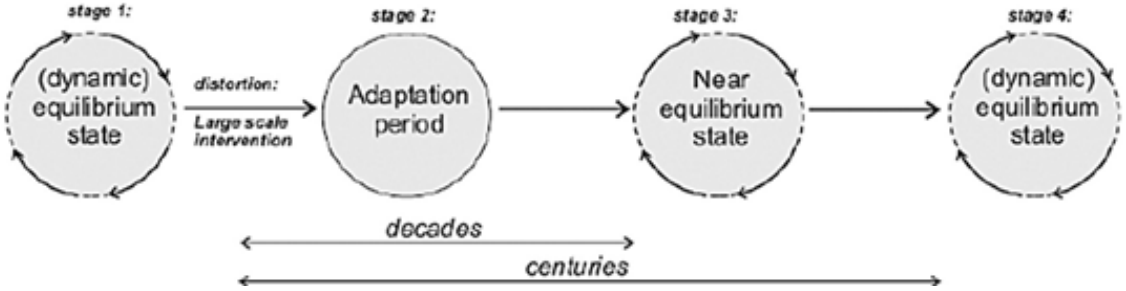

Fig. 35. Four morphological development stages of the Wadden Sea tidal basin (Elias et al., 2003; Dastgheib et al., 2008).

The morphological development of the Wadden Sea tidal basin is explained in four stages (Fig. 35) by Elias et al. (2003) and Dastgheib et al. (2008). In the first stage, before human interferences, the whole system was in dynamic equilibrium and empirical relations can be used to describe the morphology of the tidal basin. The second stage, the 'adaptation period', indicates significant changes after human interferences affected the dynamic equilibrium. In this stage, empirical relations of equilibrium cannot describe morphological developments. Stage 3 which is called the near-equilibrium stage, occurs after several decades where the adaptation continues in the long term. In the last stage, stage 4, the whole system will reach a new and different equilibrium state (Elias et al., 2003; Dastgheib et al., 2008).

In our study area, the environment of the tidal inlet system is different and therefore the stages explained above cannot be directly adapted. If we compare the stages with the Wadden Sea, there are two major key points: limited erosional potential in the channels and large space for sediment deposition behind the channels.

A morphological system strives for zero gradients in velocity between the basins, channels and the sea, and for reach an equilibrium by eroding the channels. In a system that has unlimited soft-sediment available to erode, achieving zero gradients is possible by eroding the channels and filling the basins. However, in our system erosion is limited in the channels due to bedrock being close to the surface and the geometry of the channels. Moreover, behind those channels, there are deep tidal basins which provide a large space for sediment deposition (accommodation space). Therefore,

velocity cannot reach the zero gradients between the deep sea (almost zero velocity), the shallow channels (high velocity), and the deep basins (almost zero velocity). Although the system strives to reach equilibrium (i.e., become a larger channel), it will never do so. Filling the basins with sediment is a process that is happening, but it takes geological timescales to completely fill the basin.

6.2 Model assumptions

The model results show that when the dams (barriers) are removed, the dominant process is the sudden erosion of the eastern channel. In this section various uncertainties and assumptions are described that may alter the results. The dominant phenomenon is tidal choking in the system, which is the main process responsible for erosion. The depth of the non-erodible layer, which is one of the assumptions in the model, is directly related to tidal choking. This parameter is very sensitive to changes, and it overrules all the other unknown settings in the model. Therefore, the largest uncertainty of the modelling exercise lies in the unknown non-erodible layers of the eastern channel. This layer completely steers the amount of erosion of the eastern channel. When the non-erodible layer is located close to the surface the erosion capability of the channel is limited, while it lies deep the channel will erode many meters.

- **Non-erodible layer:** During the test simulation, the model ran without a non-erodible limit on the eastern channel. After simulating morphodynamic development for half a year, it is observed that the channels eroded very quickly (~8 m). This is a questionable outcome since there is a reasonable chance that the bedrock layer is close to the surface of the channel. Therefore, an assumption should be made that the erosion capacity in the eastern channel is limited to a certain depth. After the test simulations, it is assumed that the non-erodible sediment layer is 3 m deep below the bottom, meaning no matter how much the model runs, the maximum erosion will be 3 m in the eastern channel.

Other assumption parameters are freshwater input, sediment properties, roughness, surge, and the depth of the Innerpollen, the westerly channel and the beach. These have a minor effect on the system relative to the effect of the non-erodible layer. The possible effects of unknown parameter settings can influence the time scale of erosion. Variations in these parameters can

cause erosion to occur faster or slower, meaning the timing of erosion and sedimentation may result in longer or shorter periods of time. It is not expected that these parameter settings change the outcomes of the study dramatically.

- **Freshwater input:** There is a small amount of freshwater input into the area, where the largest contribution comes from a pond, Keilvatnet (Fig. 36). Freshwater from Keilvatnet is discharged into Lauvåspollen under the bridge at Eggumsveien. Freshwater input is neglected in the model since it is assumed that it does not have a major effect on the system. However, it can affect the system in many ways i.e., salinity and fine sediment import, including effects on sediment grain size distributions, and sediment type. If the freshwater input has a large impact, salinity would be reduced in the basins and finer sediments would be transported in suspension and deposited further from the freshwater source. It is however expected that the fluvial sediment input is very limited.

Fig. 36. Location of the Keilvatnet indicated with the black rectangle.

- **Sediment properties:** The main source of sediments into the channels are the open sea beaches and shallow waters outside the tidal system. According to the sample analysis, sand is the predominant sediment type close to the channels. Therefore, all sediment is assumed to be sand in the model and other sediment types such as mud and silt are neglected. Sediment grain size in the model is assumed to be uniform and the model is run with a

constant grain size of 218 μm. This essentially controls the rate of erosion and the amount of sediment moving in and out of the system. Finer sediments can be eroded faster than coarser ones, and since they often move in suspension, longer-distance transport of finer grain sizes can potentially take place.

- **Roughness:** Roughness is another parameter that is assumed in the model. This parameter is related to the velocities of water and magnitudes of morphological changes. The larger roughness causes water to flow slower. This results in less erosion and deposition, but it also affects the tidal asymmetry. Roughness is one of the calibration parameters and the current value of roughness provide good results in the model. Therefore, this parameter is assumed to show agreement with the actual conditions.

- **Surge and wind waves:** Surge, which is a complex process of wind setup and air pressure effects, is included in the model by using the tide values calculated from Andenes. Besides, there are wind waves that might affect the basins. The wind waves can redistribute the sand along the coast onto the beach which is transported in the basin by the tidal currents.

- **Depth of Innerpollen:** Bathymetric mapping of Innerpollen was not undertaken, however, there are studies available (Waterborne Geophysics Ireland Limited, 2002). According to simulations with varying depths in Innerpollen, a change in the depth values does not affect the model results. This can be explained by the fact that the amplitude of the tide decreases (tidal choking) as it passes through each of the three basins in the system, and only minor variations can penetrate through the Innerpollen. Therefore, it is assumed that the entire basin has a single depth value, which is -30 m.

- **Depth of the Westerly channel and the beach:** The depth of the non-erodible bottom (bedrock) depth in the western channel and the beach is assumed to be limited directly on bedrock and 3 m deep, respectively, due to geological field evidence. Assuming the westerly channel is non-erodible would have large consequences if the channel consists of much erodible sand, but since the bedrock is located close to the surface by exposing in places, the assumption represents minor uncertainty.

6.3 Other effects of the removal of the dam

Removal of the dam has a major impact on the hydrodynamics and morphodynamics of the system, which will likely have some consequences in terms of the socio-economic values of the basins and the channels. Since the opening of the channel causes an increase in high water levels and a decrease in low water levels, it would create a risk of damage and flooding of low-lying structures. Buildings, agricultural lands on the seashore, especially the ones that are close to high watermarks, can be affected during flooding.

The ecosystem could also be affected. With the increase in water exchange between the sea and the basins, an increase in the salinity and oxygen levels in the basin is expected. Hence, biodiversity in the basins is expected to change with the varying conditions.

6.4 Present and Future sea-level changes

Another subject to be discussed is the relative sea-level (RSL) changes in the past, present, future and their possible effects on the study area. The global sea level in total has risen by 3.2 mm/yr from 1993 to the present (Simpson et al., 2015). Glacial isostatic adjustment (GIA) around the study area for the dates between 1960–2010 is recorded as 2.6 mm/yr (Richter et al., 2012). According to the NCCS report (Simpson et al., 2015), the mean relative sea level rose along the Norwegian coast by 1.9 mm and 2.4 mm, from 1960 to 2010 and from 1984 to 2014, respectively. However, due to vertical land motion, these relative sea levels are less pronounced in the study area. Average values of tide gauges around the study area (Harstad, Narvik, Kabelvåg, and Bodø) showed that the relative sea levels (without GIA correction) fell by -0.93 and -0.2 mm/yr over the periods of 1960-2010 and 1984-2014, respectively (Simpson et al., 2015). This reveals that the relative sea-level changes that have fallen show an increasing pattern towards the present (increased from -0.93 to -0.2 mm/yr).

The relative sea-level changes are projected along the Norwegian coast over the period 1986–2005 to 2081–2100 for three different emission scenarios (Simpson et al., 2015). According to studies based on different scenarios, relative sea levels in the Lofoten area are expected to increase by 0.3–

0.6 m over the period of 1986–2005 to 2081–2100. This means that by the end of 2100, the study area will experience 23.7–47.4 cm higher water levels.

The relationship between the past, present and future allows the water level of the study area to be reconstructed and predicted for the future (Fig. 37). Seawater was relatively higher during the last 1000 years. This is consistent with archaeological research in the area, such as studies showing the Viking longboats reaching the Innerpollen. In the current situation, the connection between the basins and the sea is very shallow due to continued glacio-isostatic uplift and a relative slow sea-level rise. The bedrock is directly exposed to the surface during low tide in areas such as Jellvollsstraumen and Evjestraumen. According to the future projections of the NCCS report (Simpson et al., 2015), the relative sea levels will increase during the 21st century. Therefore, the system is expected to be inundated more with faster-rising water levels during the 21st century, although the waters are not expected to be as deep as they were in the Viking times.

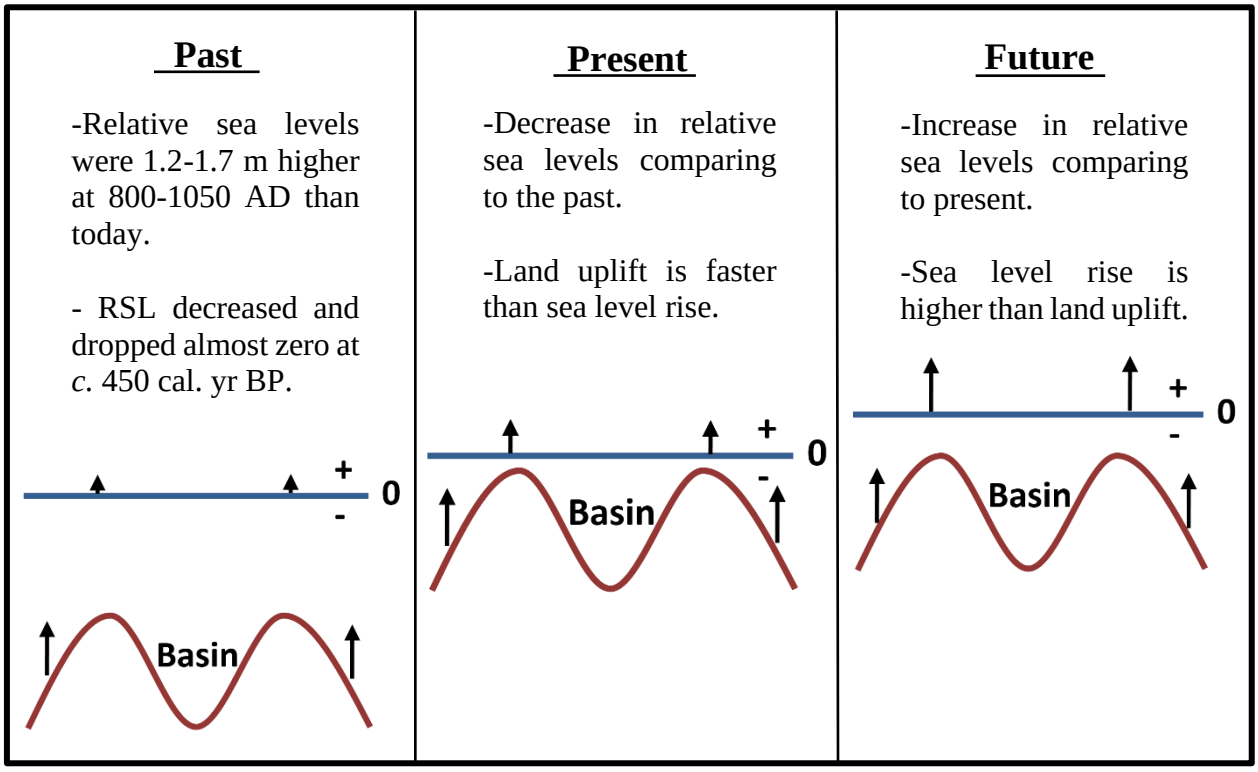

Fig. 37. Past (800-1050 AD), present and the future (21st century) sea-level changes relative to land.

7. Conclusion

In this study, the long-term morphological and sedimentological effects of the tides are modelled and explained with different scenarios on a glacially sculptured system. A combination of field and computational methods was used. The FINEL2d numerical model is used for decadal-scale modelling with two different channel condition scenarios.

- In the presence of barriers in the channel, tidal choking is a dominant phenomenon in the system as a result of the shallow channels and limited erosional capacity. Removing the barriers in the eastern channel leads to the rapid erosion of the sandy eastern channel, only limited by a non-erodible layer in the channel. Erosion decreases the amount of friction in the channel and results in less tidal choking, diminishing tidal asymmetry. This then leads to higher and lower tides in the system. The tidal choking is reduced from 79% to 29%, after the removal of the dams.

- The increase in the amount of water that goes in and out of the system due to the removal of the dams could potentially increase water circulation and affect water quality. Salinity is also expected to increase due to the increase of seawater that comes into the system.

- Relative sea levels were 1.2 m higher in Viking times than they are today. As relative sea levels are expected to rise by 0.3 – 0.5 m in the 21st century, the system is expected to be more inundated.

- There is significant uncertainty in the model regarding the depth of the bedrock in the channels. This factor dominates the amount of erosion in the eastern channel, and thus the change in tidal levels. Other sources of uncertainty mostly affect the erosion rate (time of erosion to occur), not if the eastern channel will erode. The presented model results are believed to be reliable, mainly based on the observations made when the channel was opened before and the logically explainable process of erosion of the eastern channel.

- This study can be used as a basis for future studies to be carried out on the same type of system. The results can be greatly improved by measuring the depth of bedrock in the channel, further examining the assumption factors, and computing the results with more calibration runs. Investigating areas with similar geological history and comparing the results would highly contribute to the understanding of glacially sculptured tidal systems.

8. Recommendations for future studies

Given the limited duration of the master's study, only certain goals can be achieved. However, if further studies should be undertaken in this field, the following points are recommended.

- Non-erodible layer measurements with ground-penetrating radar (GPR) (Collins et al., 1989) can be surveyed to provide a better estimate for the depth of the non-erodible layer. With such a non-erodible layer it is possible to make a better estimate of the future state of the system.
- Geomorphology of the other glacially sculptured tidal inlet system in the same area can be modelled, and results can be compared with the existing project to provide more insights.
- Pressure loggers can be deployed for a longer time to provide more data to compare and calibrate the model.
- The depths on the channels connecting the basins can be measured more precisely and the mapping can be done in the channels considering the mean sea level and the timing of the tides.
- Extreme flood levels meaning the conditions of high tide, high water level, low pressure, accompanied by weather conditions such as storms, high precipitation, can be modelled to see the effects of the extreme conditions in the study area.

9. References

Balascio, N. L., & Wickler, S. (2018). Human–environment dynamics during the Iron Age in the Lofoten Islands, Norway. *Norsk Geografisk Tidsskrift - Norwegian Journal of Geography*, *72*(3), 146–160. https://doi.org/10.1080/00291951.2018.1466831

Balascio, N. L., Wickler, S., Narmo, L. E., & Bradley, R. S. (2011). Distal cryptotephra found in a Viking boathouse: The potential for tephrochronology in reconstructing the Iron Age in Norway. *Journal of Archaeological Science*, *38*(4), 934–941. https://doi.org/10.1016/j.jas.2010.11.023

Blott, S. J., & Pye, K. (2001). Gradistat: A grain size distribution and statistics package for the analysis of unconsolidated sediments. *Earth Surface Processes and Landforms*, *26*(11), 1237–1248. https://doi.org/10.1002/esp.261

Bøe, R., Bjarnadóttir, L. R., Elvenes, S., Dolan, M., Bellec, V., Thorsnes, T., Lepland, A., & Longva, O. (2020). Revealing the secrets of Norway's seafloor – geological mapping within the MAREANO programme and in coastal areas. *Geological Society, London, Special Publications*, *June*. https://doi.org/10.1144/SP505-2019-82

Collins, M. E., Doolittle, J. A., & Rourke, R. V. (1989). Mapping depth to bedrock on a glaciated landscape with Ground-Penetrating Radar. *Soil Science Society of America Journal*, *53*(6), 1806–1812. https://doi.org/10.2136/sssaj1989.03615995005300060032x

D'Alpaos, A., Lanzoni, S., Marani, M., & Rinaldo, A. (2010). On the tidal prism-channel area relations. *Journal of Geophysical Research: Earth Surface*, *115*(1), 1–13. https://doi.org/10.1029/2008JF001243

Dam, G., Bliek, A. J., & Bruens, A. W. (2005). Band width analysis morphological predictions Haringvliet Estuary. *Proceedings of 4th IAHR Symposium of the River, Coastal and Estuarine Morphodynamics Conference*, 171–179. https://doi.org/10.1201/9781439833896.ch21

Dam, G., Bliek, A. J., Labeur, R. J., Ides, S. J., & Plancke, Y. M. G. (2007). Long term process-based morphological model of the Western Scheldt Estuary. *Proceedings of the 5th IAHR Symposium on River, Coastal and Estuarine Morphodynamics Conference*, 1077–1084. https://doi.org/10.1201/noe0415453639-c135

Dam, G., Bliek, A. J., & Nederbragt, G. (2009). High resolution long term morphological model of the northern part of the Holland Coast and Texel Inlet. *Proceedings of 5th IAHR Symposium of the River, Coastal and Estuarine Morphodynamics Conference*, 933–939.

Dam, G., van der Wegen, M., Labeur, R. J., & Roelvink, D. (2016). Modeling centuries of estuarine morphodynamics in the Western Scheldt estuary. *Geophysical Research Letters*, *43*, 3839–3847. https://doi.org/10.1002/2015GL066725

Dam, G., & Bliek, A. J. (2013). Using a sand-mud model to hindcast the morphology near Waarde, the Netherlands. *Maritime Engineering*, *166*(2), 63–75. https://doi.org/10.1680/maen.2011.43

Dam, G., van der Wegen, M., & Roelvink, D. (2013). Long-term performance of process-based models in estuaries. *Proceedings of Coastal Dynamics*, 409–420.

Dastgheib, A., Roelvink, J. A., & Wang, Z. B. (2008). Long-term process-based morphological modeling of the Marsdiep Tidal Basin. *Marine Geology*, *256*(1–4), 90–100. https://doi.org/10.1016/j.margeo.2008.10.003

de Swart, H. E., & Zimmerman, J. T. F. (2009). Morphodynamics of tidal inlet systems. *Annual Review of Fluid Mechanics*, *41*, 203–229. https://doi.org/10.1146/annurev.fluid.010908.165159

de Vriend, H. J. (1996). Mathematical modeling of Meso-tidal barrier island coasts. Part I: Empirical and Semi-Empirical Models. *Advances in Coastal and Ocean Engineering*, 115–149.

Dronkers, J. (1986). Tidal asymmetry and estuarine morphology. *Netherlands Journal of Sea Research*, *20*(2–3), 117–131. https://doi.org/10.1016/0077-7579(86)90036-0

Dybdedata. (n.d.). [The depth data to create the bottom file]. Retrieved October 20, 2020, from https://dybdedata.kartverket.no/DybdedataInnsyn/

Egbert, G. D., & Erofeeva, Y. S. (2002). Efficient inverse modeling of barotropic ocean tides. *Journal of Atmospheric and Oceanic Technology*, *19*(2), 183–204. https://doi.org/10.1175/1520-0426(2002)019<0183:EIMOBO>2.0.CO;2

Elias, E. (2006). *Morphodynamics of Texel Inlet*, [Delft University of Technology]. https://repository.tudelft.nl/islandora/object/uuid:92ad4ac0-9d54-4f5f-8536-80b7782a6aa6?collection=research

Elias, E., Stive, M., Bonekamp, H., & Cleveringa, J. (2003). Tidal inlet dynamics in response to human intervention. *Coastal Engineering Journal*, *45*(4), 629–658. https://doi.org/10.1142/S0578563403000932

Engelund, F., & Hansen, E. (1967). *Monograph on sediment transport in alluvial streams*. Teknik Forlag, Copenhagen.

FitzGerald, D. M., & Miner, M. D. (2013). Tidal Inlets and Lagoons along Siliciclastic Barrier Coasts. In John F. Shroder (Ed.), *Treatise on Geomorphology* (Vol. 10, pp. 149–165). Elsevier Ltd. https://doi.org/10.1016/B978-0-12-374739-6.00278-5

Fredin, O., Bergstrøm, B., Eilertsen, R., Hansen, L., Longva, O., Nesje, A., & Sveian, H. (2013). Glacial landforms and Quaternary landscape development in Norway. *Geological Survey of Norway. Special Publication*, *13*, 5–25.

Galappatti, G., & Vreugdenhil, C. B. (1985). A depth-integrated model for suspended sediment transport. *Journal of Hydraulic Research*, *23 (4)*, 359–377. https://doi.org/doi:10.1080/00221688509499345

Gao, S., & Collins, M. (1994). Tidal inlet stability in response to hydrodynamic and sediment dynamic conditions. *Coastal Engineering*, *23*(1–2), 61–80. https://doi.org/10.1016/0378-3839(94)90015-9

Glørstad, H., Gundersen, J., Kvalø, F., Nymoen, P., Simpson, D., & Skar, B. (2020). Norway: submerged stone age from a norwegian perspective. *Coastal Research Library*, *35*, 125–140. https://doi.org/10.1007/978-3-030-37367-2_6

Timelapse. (n.d.). [Geospatial analysis of the historical data]. Retrieved August 31, 2021, from https://earthengine.google.com/timelapse/

Gornitz, V. (2013). The Ever-Changing Ocean. In *Rising Seas : Past, Present, Future* (pp. 1–28). Columbia University Press.

Griffin, W. L., Taylor, P. N., Hakkinen, J. W., Heier, K. S., Iden, I. K., Krogh, E. J., Malm, O., Olsen, K. I., Ormaasen, D. E., & Tveten, E. (1978). Archaean and Proterozoic crustal evolution in Lofoten-Vesterålen, N Norway. *Journal of the Geological Society*, *135*, 629–647.

Guo, W., Wang, X. H., Ding, P., Ge, J., & Song, D. (2018). A system shift in tidal choking due to the construction of Yangshan Harbour, Shanghai, China. *Estuarine, Coastal and Shelf Science*, *206*, 49–60. https://doi.org/10.1016/j.ecss.2017.03.017

Haff, P. K. (1996). Limitations on predictive modeling in geomorphology. In T. Rhoads, B. & C. (Eds.), *The Scientific Nature of Geomorphology* (pp. 337–358). John Wiley & Sons Ltd.

Hafsten, U., & Tallantire, P. A. (1978). Palaeoecology and post- Weichselian shore-level changes on the coast of Møre, western Norway. *Boreas*, *7*. https://doi.org/https://doi.org/10.1111/j.1502-3885.1978.tb00269.x

Hafsten, U. (1960). Pollen-analytic investigations in South Norway. In O. Holtedahl (Ed.), *Norges geologiske undersøkelse (NGU)*, 434–462.

Hayes, M. O., & FitzGerald, D. M. (2013). Origin, Evolution, and Classification of Tidal Inlets. *Journal of Coastal Research*, *69*, 14–33. https://doi.org/10.2112/si_69_3

Høydedata. (n.d.). [The altitude data to create the bottom file]. Retrieved October 20, 2020, from https://hoydedata.no/LaserInnsyn/

Jia, J., & Gao, S. (2008). A sedimentological approach to P-A relationships for tidal inlet systems: An example from Yuehu Inlet, Shandong Peninsula, China. *Frontiers of Earth Science in China*, *2*(3), 262–268. https://doi.org/10.1007/s11707-008-0022-0

Johns, B., & Oguz, T. (1987). Turbulent energy closure schemes. *Coastal and Estuarine Sciences*, *4*, 17–39. https://doi.org/doi:10.1029/co004p0017

Kartverket. (n.d.-a). [Historical aerial image from 1985] Retrieved June 4, 2021, from https://www.kartverket.no/om-kartverket/historie/historiske-kart

Kartverket. (n.d.-b). [Tide level observations from Andenes]. Retrieved June 4, 2021, from https://www.kartverket.no/til-sjos/se-havniva

Kroon, A., Van Leeuwen, B., Waistra, D. J., & Loman, G. (2016). Dealing with uncertainties in long-term predictions of a coastal nourishment. *Coastal Management: Changing Coast, Changing Climate, Changing Minds - Proceedings of the International Conference*, 9–18. https://doi.org/10.1680/cm.61149.009

Mangerud, J., Gyllencreutz, R., Lohne, Ø., & Svendsen, J. I. (2011). Glacial history of Norway. In *Quaternary Glaciations - Extent and Chronology - A Closer Look* (Vol. 15, pp. 279–298). Developments in Quaternary Science. https://doi.org/10.1016/B978-0-444-53447-7.00022-2

Mangerud, J., Jansen, E., & Landvik, J. Y. (1996). Late cenozoic history of the Scandinavian and Barents Sea ice sheets. *Global and Planetary Change*, *12*(1–4), 11–26. https://doi.org/10.1016/0921-8181(95)00009-7

Marthinussen, M. (1962). C14-datings referring to shorelines, transgressions, and glacial substages in northern Norway. *Norsk Geologisk Undersøkelse*, *215*, 37–67.

Martin, F. V. (2009). Rías and tidal-sea estuaries. In Federico Ignacio Isla & Oscar Iribarne (Eds.), *Coastal Zones and Estuaries* (pp. 285–320). UNESCO, EOLSS.

Merckelbach, L. M. (2006). A model for high-frequency acoustic Doppler current profiler backscatter from suspended sediment in strong currents. *Continental Shelf Research*, *26*, 1316–1335. https://doi.org/10.1016/j.csr.2006.04.009

Mills, K., Mackay, A. W., Bradley, R. S., & Finney, B. (2009). Diatom and stable isotope records of late-Holocene lake ontogeny at Indrepollen, Lofoten, NW Norway: A response to glacio-isostasy and Neoglacial cooling. *Holocene*, *19*(2), 261–271. https://doi.org/10.1177/0959683608100571

Mokhtari, M., & Pegrum, R. M. (1992). Structure and evolution of the Lofoten continental margin, offshore Norway. *Norsk Geologisk Tidsskrift*, *72*(4), 339–355.

Møller, J. J. (1984). Holocene shore displacement at Nappstraumen, Lofoten, north Norway. *Norsk Geologisk Tidsskrift*, *64*(1), 1–5.

Møller, J. J. (1989). Geometric simulation and mapping of Holocene relative sea-level changes in northern Norway. *Journal of Coastal Research*, *5*(3), 403–417.

Møller, J. J. (1986). Holocene transgression maximum about 6000 years BP at Ramså, Vesterälen, North Norway. *Norsk Geografisk Tidsskrift - Norwegian Journal of Geography*, *40*(2), 77–84. https://doi.org/10.1080/00291958608552158

Nesje, A., & Whillans, I. M. (1994). Erosion of Sognefjord, Norway. *Geomorphology*, *9*, 33–45. https://doi.org/https://doi.org/10.1016/0169-555X(94)90029-9

NGU. (n.d.). [Superficial deposits-main classes of deposits around Vestvågøy]. Retrieved September 20, 2021, from https://geo.ngu.no/kart/geologiskarv_mobil/?lang=eng

Nygård, L., Sletten, K., & Eilertsen, R. S. (2019). Foreløpig Kvartærgeologisk kart, M 1:10 000, Saupstad, Vestvågøy kommune. *Norges Geologiske Undersøkelse (NGU)*.

Olesen, O., Bering, D., Brönner, M., Dalsegg, E., Fabian, K., Fredin, O., Gellein, J., Husteli, B., Magnus, C., Rønning, J.S., Solbakk, T., Tønnesen, J. F., & Øverland, J. A. (2012). *Tropical Weathering in Norway, TWIN Final Report*.

Olsen, L., Sveian, H., Bergstrøm, B., Ottesen, D., & Rise, L. (2013). Quaternary glaciations and their variations in Norway and on the Norwegian continental shelf. *Quaternary Geology of Norway, Geological Survey of Norway Special Publication*, *13*, 27–78.

Onset Computer Corporation. (n.d.). *HOBO U20L Water Level Logger (U20L-0x) Manual*. Retrieved July 2, 2021, from https://www.onsetcomp.com/files/manual_pdfs/17153-G U20L Manual.pdf

Ottesen, D., Dowdeswell, J. A., & Rise, L. (2005). Submarine landforms and the reconstruction of fast-flowing ice streams within a large Quaternary ice sheet: The 2500-km-long Norwegian-Svalbard margin (57°-80°N). *Bulletin of the Geological Society of America*, *117*, 1033–1050. https://doi.org/10.1130/B25577.1

Paola, C., & Voller, V. R. (2005). A generalized Exner equation for sediment mass balance. *Journal of Geophysical Research: Earth Surface*, *110*(4). https://doi.org/10.1029/2004JF000274

Ren, M., & Zhang, R. (1985). On tidal inlets of China. *Acta Oceanologica Sinica*, *4*(3), 423–432.

Richter, K., Nilsen, J. E. Ø., & Drange, H. (2012). Contributions to sea level variability along the Norwegian coast for 1960-2010. *Journal of Geophysical Research: Oceans*, *117*, 1–12. https://doi.org/10.1029/2011JC007826

Rise, L., Bøe, R., Riis, F., Bellec, V. K., Laberg, J. S., Eidvin, T., Elvenes, S., & Thorsnes, T. (2013). The Lofoten-Vesterålen continental margin, North Norway: Canyons and mass-

movement activity. *Marine and Petroleum Geology*, *45*, 134–149. https://doi.org/10.1016/j.marpetgeo.2013.04.021

Roelvink, J. A. (2006). Coastal morphodynamic evolution techniques. *Coastal Engineering*, *53*(2–3), 277–287. https://doi.org/10.1016/j.coastaleng.2005.10.015

Romundset, A., Bondevik, S., & Bennike, O. (2011). Postglacial uplift and relative sea level changes in Finnmark, northern Norway. *Quaternary Science Reviews*, *30*(19–20), 2398–2421. https://doi.org/10.1016/j.quascirev.2011.06.007

Simpson, M. J. R., Nilsen, J. E. Ø., Ravndal, O. R., Breili, K., Sande, H., Kierulf, H. P., Steffen, H., Jansen, E., Carson, M., & Vestøl, O. (2015). Sea level change for Norway: Past and present observations and projections to 2100. *Norwegian Centre for Climate Services Report*.

Svendsen, J. I., & Mangerud, J. (1987). Late Weichselian and Holocene sea-level history for a cross-section of western Norway. *Journal of Quaternary Science*, *2*, 113–132. https://doi.org/10.1002/jqs.3390020205

Tull, J. F. (1973). *The geology and structure of Vestvaagöy in Lofoten, North Norway*. Rice University.

van Rijn, L. C. (2010). Tidal phenomena in the Scheldt Estuary. *Deltares*. http://www.vliz.be/imisdocs/publications/214759.pdf

Vorren, K.-D., & Moe, D. (1986). The early Holocene climate and sea-level changes in Lofoten and Vesteralen, north Norway. *Norsk Geologisk Tidsskrift*, *66*, 135–143.

Vorren, T. O., Vorren, K.-D., Alm, T., Gulliksen, S., & Løvlie, R. (1988). The last deglaciation (20 000 to 11 000 B.P.) on Andøya, northern Norway. *Boreas*, *17*, 41–77. https://doi.org/10.1111/j.1651-2227.1971.tb07508.x

Vorren, T. O., Rydningen, T. A., Baeten, N. J., & Laberg, J. S. (2015). Chronology and extent of the Lofoten-Vesterålen sector of the Scandinavian Ice Sheet from 26 to 16 cal. ka BP. *Boreas*, *44*(3), 445–458. https://doi.org/10.1111/bor.12118

Vreugdenhil, C. B. (1994). Numerical methods for shallow-water flow. In *Water Science and Technology Library* (Vol. 13). Kluwer Academic Publishers. https://doi.org/10.1007/978-94-015-8354-1

Wahr, J. (1995). Earth tides. In T. J. Ahrens (Ed.), *Global Earth Physics. A Handbook of Physical Constants* (pp. 40–46). https://doi.org/https://doi.org/10.1029/RF001p0040

Waterborne Geophysics Ireland Limited. (2002). *Borg maritime landscape project, Inner Borgpollen, Borg, Lofoten Islands, Northern Norway. Waterborne geophysical surveys 2001*

and 2002, Operational report and results. Unpublished report prepared for Tromsø Museum / University of Tromsø.

Wickler, S. (2004). A maritime view of the past in North Norway. In: S. Wickler (Ed.). *Archaeology in North Norway. Tromsø Univeristy Museum*, 60–71.

Xie, D., Gao, S., & Pan, C. (2010). Process-based modeling of morphodynamics of a tidal inlet system. *Acta Oceanologica Sinica, 29*(6), 51–61. https://doi.org/10.1007/s13131-010-0076-1.

Appendix - **Single sample statistics**

SAMPLE STATISTICS

SAMPLE IDENTITY: **NER41** ANALYST & DATE: Nil, 8/12/2020

SAMPLE TYPE: Bimodal, Moderately Well Sorted TEXTURAL GROUP: Sand

SEDIMENT NAME: Moderately Well Sorted Medium Sand

	μm	ϕ
MODE 1:	327,5	1,616
MODE 2:	231,0	2,119
MODE 3:		
D_{10}:	183,3	1,093
MEDIAN or D_{50}:	303,5	1,720
D_{90}:	468,9	2,447
(D_{90} / D_{10}):	2,558	2,240
(D_{90} - D_{10}):	285,6	1,355
(D_{75} / D_{25}):	1,694	1,544
(D_{75} - D_{25}):	155,4	0,760

GRAIN SIZE DISTRIBUTION

GRAVEL:	0,0%	COARSE SAND:	7,7%
SAND:	100,0%	MEDIUM SAND:	56,6%
MUD:	0,0%	FINE SAND:	34,9%
		V FINE SAND:	0,8%
V COARSE GRAVEL:	0,0%	V COARSE SILT:	0,0%
COARSE GRAVEL:	0,0%	COARSE SILT:	0,0%
MEDIUM GRAVEL:	0,0%	MEDIUM SILT:	0,0%
FINE GRAVEL:	0,0%	FINE SILT:	0,0%
V FINE GRAVEL:	0,0%	V FINE SILT:	0,0%
V COARSE SAND:	0,0%	CLAY:	0,0%

	METHOD OF MOMENTS			FOLK & WARD METHOD		
	Arithmetic	Geometric	Logarithmic	Geometric	Logarithmic	Description
	μm	μm	ϕ	μm	ϕ	
MEAN ($\bar{x}$):	319,5	278,3	1,744	293,5	1,768	Medium Sand
SORTING (σ):	145,5	1,996	0,590	1,486	0,572	Moderately Well Sorted
SKEWNESS (Sk):	1,440	-5,390	-0,283	-0,021	0,021	Symmetrical
KURTOSIS (K):	5,648	45,10	3,601	1,103	1,103	Mesokurtic

GRAIN SIZE DISTRIBUTION

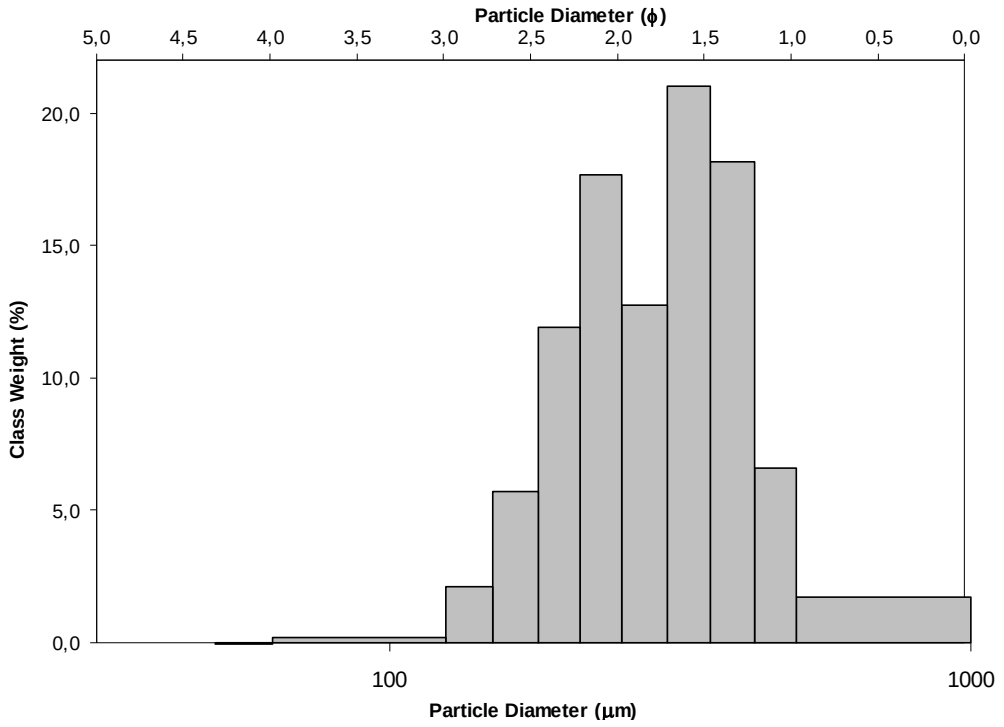

SAMPLE STATISTICS

SAMPLE IDENTITY: **NER49** ANALYST & DATE: Nil, 11/24/2020

SAMPLE TYPE: Unimodal, Moderately Well Sorted TEXTURAL GROUP: Sand

SEDIMENT NAME: Moderately Well Sorted Fine Sand

	μm	ϕ
MODE 1:	165,0	2,605
MODE 2:		
MODE 3:		
D_{10}:	140,3	1,462
MEDIAN or D_{50}:	197,1	2,343
D_{90}:	362,9	2,834
(D_{90} / D_{10}):	2,587	1,938
(D_{90} - D_{10}):	222,6	1,371
(D_{75} / D_{25}):	1,573	1,333
(D_{75} - D_{25}):	93,55	0,654

GRAIN SIZE DISTRIBUTION

GRAVEL:	0,0%	COARSE SAND:	3,8%
SAND:	100,0%	MEDIUM SAND:	22,8%
MUD:	0,0%	FINE SAND:	68,1%
		V FINE SAND:	5,3%
V COARSE GRAVEL:	0,0%	V COARSE SILT:	0,0%
COARSE GRAVEL:	0,0%	COARSE SILT:	0,0%
MEDIUM GRAVEL:	0,0%	MEDIUM SILT:	0,0%
FINE GRAVEL:	0,0%	FINE SILT:	0,0%
V FINE GRAVEL:	0,0%	V FINE SILT:	0,0%
V COARSE SAND:	0,0%	CLAY:	0,0%

	METHOD OF MOMENTS			FOLK & WARD METHOD		
	Arithmetic	Geometric	Logarithmic	Geometric	Logarithmic	Description
	μm	μm	ϕ	μm	ϕ	
MEAN ($\bar{x}$):	231,0	204,1	2,250	207,9	2,266	Fine Sand
SORTING (σ):	124,1	1,717	0,612	1,444	0,530	Moderately Well Sorted
SKEWNESS (Sk):	2,574	-3,755	-0,790	0,251	-0,251	Coarse Skewed
KURTOSIS (K):	10,98	42,11	4,619	1,205	1,205	Leptokurtic

GRAIN SIZE DISTRIBUTION

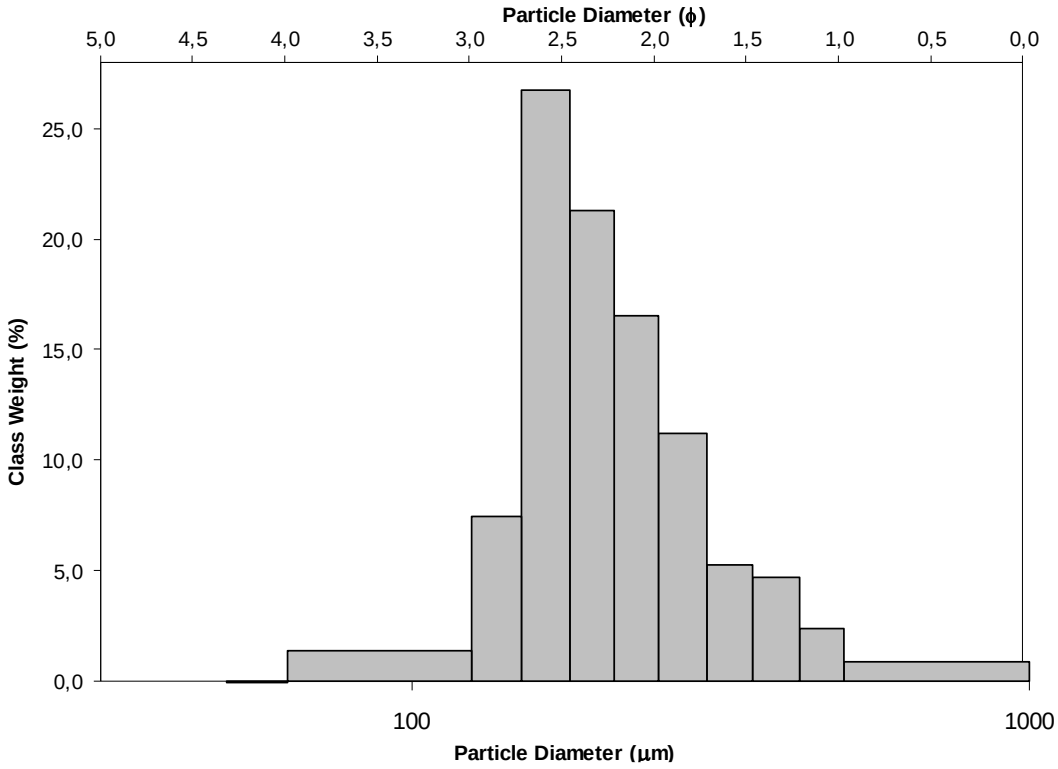

SAMPLE STATISTICS

SAMPLE IDENTITY: **NER37**

ANALYST & DATE: Nil, 11/24/2020

SAMPLE TYPE: Unimodal, Well Sorted

TEXTURAL GROUP: Sand

SEDIMENT NAME: Well Sorted Fine Sand

	μm	ϕ
MODE 1:	275,0	1,868
MODE 2:		
MODE 3:		
D_{10}:	163,9	1,570
MEDIAN or D_{50}:	244,9	2,030
D_{90}:	336,8	2,609
(D_{90} / D_{10}):	2,054	1,662
(D_{90} - D_{10}):	172,8	1,039
(D_{75} / D_{25}):	1,427	1,281
(D_{75} - D_{25}):	84,51	0,513

GRAIN SIZE DISTRIBUTION

GRAVEL:	0,0%	COARSE SAND:	1,9%
SAND:	100,0%	MEDIUM SAND:	45,6%
MUD:	0,0%	FINE SAND:	51,0%
		V FINE SAND:	1,5%
V COARSE GRAVEL:	0,0%	V COARSE SILT:	0,0%
COARSE GRAVEL:	0,0%	COARSE SILT:	0,0%
MEDIUM GRAVEL:	0,0%	MEDIUM SILT:	0,0%
FINE GRAVEL:	0,0%	FINE SILT:	0,0%
V FINE GRAVEL:	0,0%	V FINE SILT:	0,0%
V COARSE SAND:	0,0%	CLAY:	0,0%

	METHOD OF MOMENTS			FOLK & WARD METHOD		
	Arithmetic	Geometric	Logarithmic	Geometric	Logarithmic	Description
	μm	μm	ϕ	μm	ϕ	
MEAN ($\bar{x}$):	251,7	234,9	2,061	236,3	2,081	Fine Sand
SORTING (σ):	91,57	1,534	0,460	1,314	0,394	Well Sorted
SKEWNESS (Sk):	2,563	-5,953	-0,357	-0,117	0,117	Fine Skewed
KURTOSIS (K):	14,87	78,84	5,915	1,146	1,146	Leptokurtic

GRAIN SIZE DISTRIBUTION

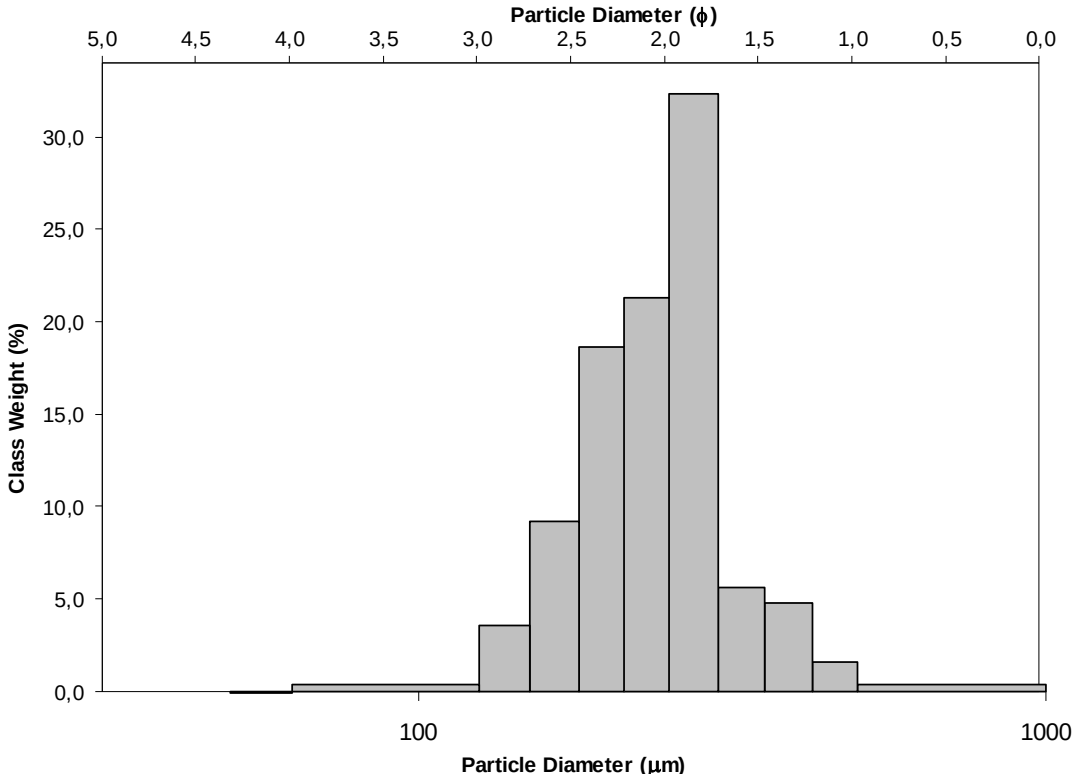

SAMPLE STATISTICS

SAMPLE IDENTITY: **NER48**

ANALYST & DATE: Nil, 8/12/2020

SAMPLE TYPE: Unimodal, Well Sorted

TEXTURAL GROUP: Sand

SEDIMENT NAME: Well Sorted Fine Sand

	μm	ϕ
MODE 1:	196,0	2,356
MODE 2:		
MODE 3:		
D_{10}:	158,7	1,556
MEDIAN or D_{50}:	220,0	2,184
D_{90}:	340,0	2,656
(D_{90} / D_{10}):	2,142	1,706
(D_{90} - D_{10}):	181,3	1,099
(D_{75} / D_{25}):	1,439	1,278
(D_{75} - D_{25}):	82,47	0,525

GRAIN SIZE DISTRIBUTION

GRAVEL:	0,0%	COARSE SAND:	1,9%
SAND:	99,9%	MEDIUM SAND:	29,3%
MUD:	0,1%	FINE SAND:	66,6%
		V FINE SAND:	2,2%
V COARSE GRAVEL:	0,0%	V COARSE SILT:	0,1%
COARSE GRAVEL:	0,0%	COARSE SILT:	0,0%
MEDIUM GRAVEL:	0,0%	MEDIUM SILT:	0,0%
FINE GRAVEL:	0,0%	FINE SILT:	0,0%
V FINE GRAVEL:	0,0%	V FINE SILT:	0,0%
V COARSE SAND:	0,0%	CLAY:	0,0%

	METHOD OF MOMENTS			FOLK & WARD METHOD		
	Arithmetic	Geometric	Logarithmic	Geometric	Logarithmic	Description
	μm	μm	ϕ	μm	ϕ	
MEAN ($\bar{x}$):	241,9	225,8	2,141	226,6	2,142	Fine Sand
SORTING (σ):	97,70	1,432	0,483	1,346	0,428	Well Sorted
SKEWNESS (Sk):	2,756	-1,827	-0,437	0,153	-0,153	Coarse Skewed
KURTOSIS (K):	14,37	36,55	5,384	1,169	1,169	Leptokurtic

GRAIN SIZE DISTRIBUTION

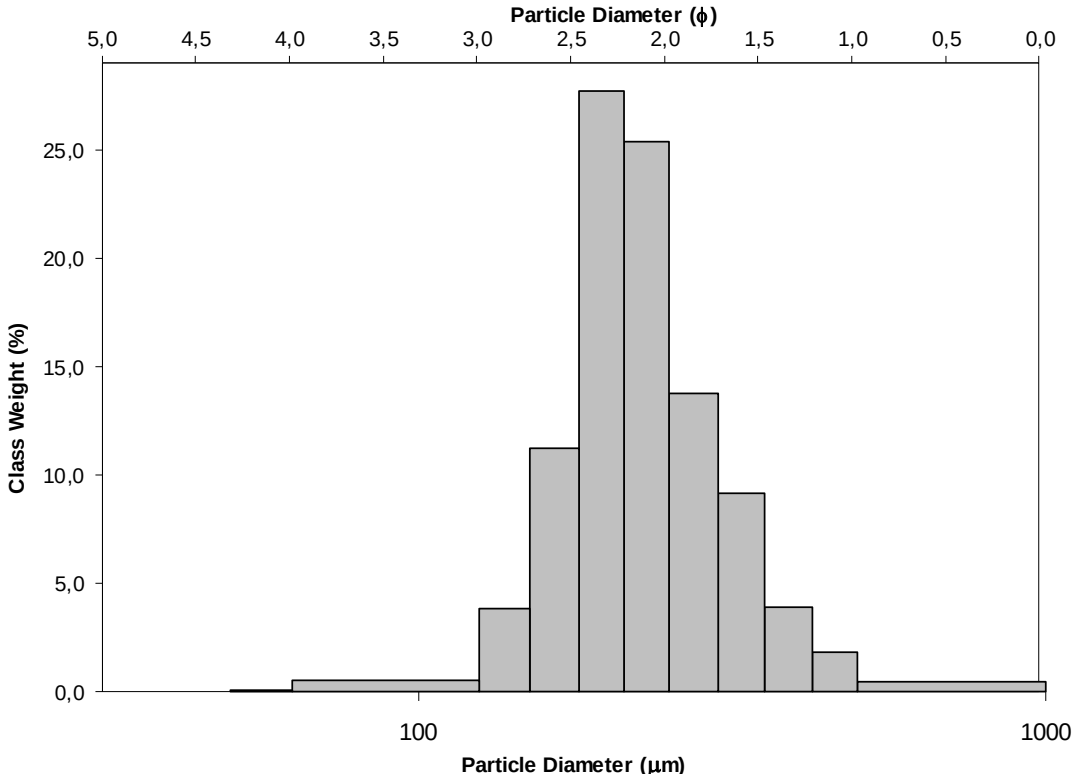

SAMPLE STATISTICS

SAMPLE IDENTITY: **NER35** ANALYST & DATE: Nil, 11/24/2020

SAMPLE TYPE: Unimodal, Moderately Well Sorted TEXTURAL GROUP: Sand

SEDIMENT NAME: Moderately Well Sorted Fine Sand

	μm	ϕ
MODE 1:	165,0	2,605
MODE 2:		
MODE 3:		
D_{10}:	103,8	1,915
MEDIAN or D_{50}:	168,1	2,572
D_{90}:	265,1	3,268
(D_{90} / D_{10}):	2,554	1,706
(D_{90} - D_{10}):	161,3	1,353
(D_{75} / D_{25}):	1,472	1,246
(D_{75} - D_{25}):	66,64	0,558

GRAIN SIZE DISTRIBUTION

GRAVEL:	0,0%	COARSE SAND:	0,6%
SAND:	99,7%	MEDIUM SAND:	12,0%
MUD:	0,3%	FINE SAND:	73,7%
		V FINE SAND:	13,4%
V COARSE GRAVEL:	0,0%	V COARSE SILT:	0,3%
COARSE GRAVEL:	0,0%	COARSE SILT:	0,0%
MEDIUM GRAVEL:	0,0%	MEDIUM SILT:	0,0%
FINE GRAVEL:	0,0%	FINE SILT:	0,0%
V FINE GRAVEL:	0,0%	V FINE SILT:	0,0%
V COARSE SAND:	0,0%	CLAY:	0,0%

	METHOD OF MOMENTS			FOLK & WARD METHOD		
	Arithmetic	Geometric	Logarithmic	Geometric	Logarithmic	Description
	μm	μm	ϕ	μm	ϕ	
MEAN ($\bar{x}$):	182,6	168,5	2,566	172,3	2,537	Fine Sand
SORTING (σ):	76,99	1,464	0,532	1,421	0,507	Moderately Well Sorted
SKEWNESS (Sk):	3,009	-0,758	-0,227	-0,007	0,007	Symmetrical
KURTOSIS (K):	20,18	16,25	4,236	1,384	1,384	Leptokurtic

GRAIN SIZE DISTRIBUTION

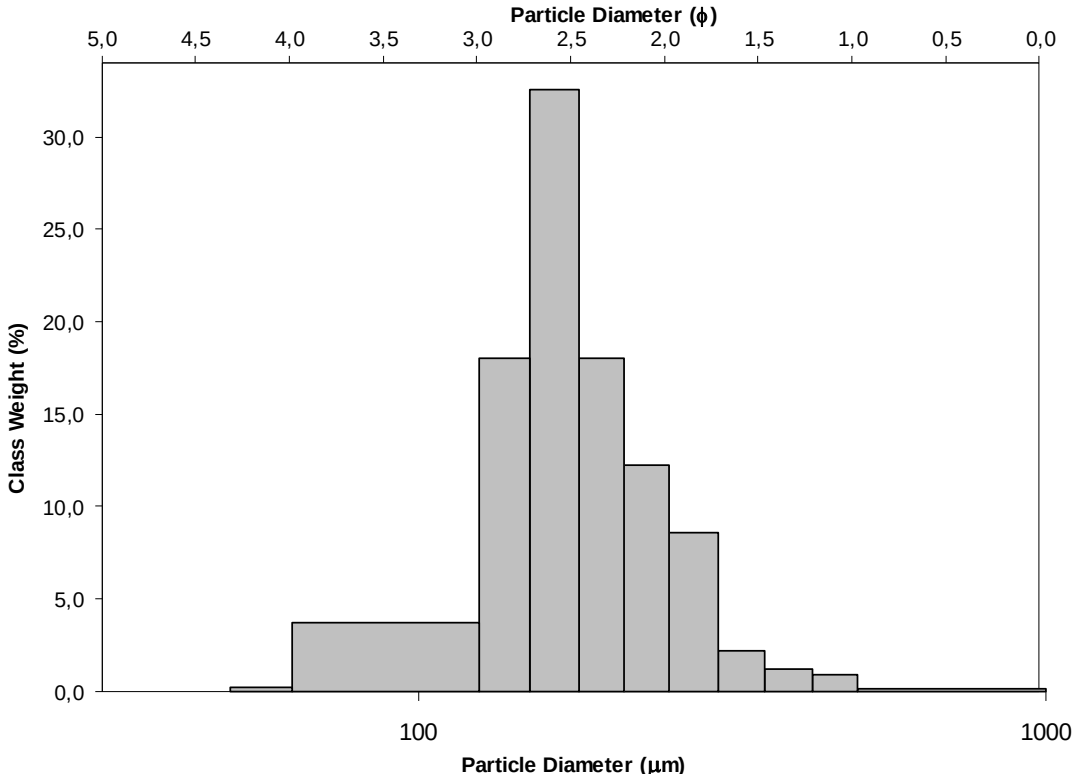

SAMPLE STATISTICS

SAMPLE IDENTITY: **NER50** ANALYST & DATE: Nil, 11/24/2020

SAMPLE TYPE: Unimodal, Well Sorted TEXTURAL GROUP: Sand

SEDIMENT NAME: Well Sorted Medium Sand

	μm	ϕ
MODE 1:	275,0	1,868
MODE 2:		
MODE 3:		
D_{10}:	201,8	1,143
MEDIAN or D_{50}:	287,3	1,799
D_{90}:	452,8	2,309
(D_{90} / D_{10}):	2,243	2,020
(D_{90} - D_{10}):	250,9	1,166
(D_{75} / D_{25}):	1,539	1,429
(D_{75} - D_{25}):	128,3	0,622

GRAIN SIZE DISTRIBUTION

GRAVEL:	0,0%	COARSE SAND:	5,7%
SAND:	100,0%	MEDIUM SAND:	63,9%
MUD:	0,0%	FINE SAND:	29,9%
		V FINE SAND:	0,5%
V COARSE GRAVEL:	0,0%	V COARSE SILT:	0,0%
COARSE GRAVEL:	0,0%	COARSE SILT:	0,0%
MEDIUM GRAVEL:	0,0%	MEDIUM SILT:	0,0%
FINE GRAVEL:	0,0%	FINE SILT:	0,0%
V FINE GRAVEL:	0,0%	V FINE SILT:	0,0%
V COARSE SAND:	0,0%	CLAY:	0,0%

	METHOD OF MOMENTS			FOLK & WARD METHOD		
	Arithmetic	Geometric	Logarithmic	Geometric	Logarithmic	Description
	μm	μm	ϕ	μm	ϕ	
MEAN ($\bar{x}$):	320,3	296,0	1,745	295,2	1,760	Medium Sand
SORTING (σ):	130,7	1,484	0,502	1,379	0,464	Well Sorted
SKEWNESS (Sk):	1,839	-3,097	-0,382	0,149	-0,149	Coarse Skewed
KURTOSIS (K):	6,927	50,98	4,109	1,040	1,040	Mesokurtic

GRAIN SIZE DISTRIBUTION

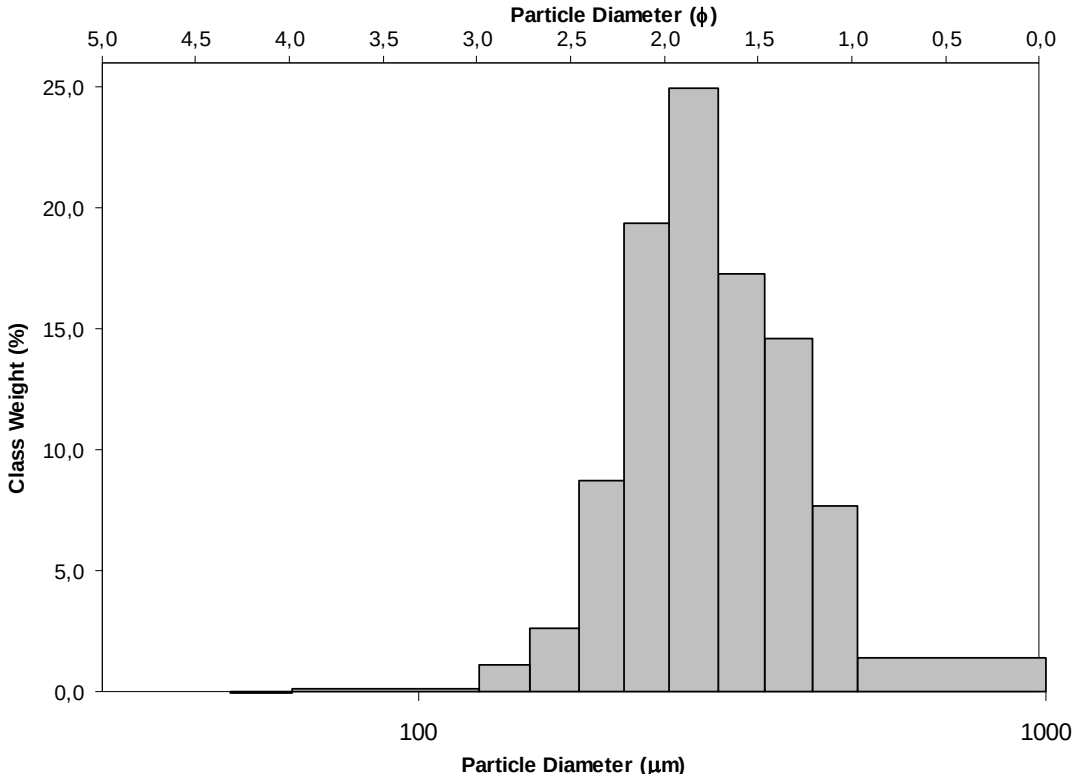

SAMPLE STATISTICS

SAMPLE IDENTITY: **NER2** ANALYST & DATE: Nil, 8/12/2020

SAMPLE TYPE: Unimodal, Moderately Well Sorted TEXTURAL GROUP: Sand

SEDIMENT NAME: Moderately Well Sorted Fine Sand

	μm	ϕ
MODE 1:	231,0	2,119
MODE 2:		
MODE 3:		
D_{10}:	156,5	1,208
MEDIAN or D_{50}:	238,0	2,071
D_{90}:	432,9	2,676
(D_{90} / D_{10}):	2,766	2,215
(D_{90} - D_{10}):	276,4	1,468
(D_{75} / D_{25}):	1,626	1,423
(D_{75} - D_{25}):	122,0	0,702

GRAIN SIZE DISTRIBUTION

GRAVEL:	0,0%	COARSE SAND:	6,3%
SAND:	99,9%	MEDIUM SAND:	36,6%
MUD:	0,1%	FINE SAND:	53,6%
		V FINE SAND:	3,4%
V COARSE GRAVEL:	0,0%	V COARSE SILT:	0,1%
COARSE GRAVEL:	0,0%	COARSE SILT:	0,0%
MEDIUM GRAVEL:	0,0%	MEDIUM SILT:	0,0%
FINE GRAVEL:	0,0%	FINE SILT:	0,0%
V FINE GRAVEL:	0,0%	V FINE SILT:	0,0%
V COARSE SAND:	0,0%	CLAY:	0,0%

	METHOD OF MOMENTS			FOLK & WARD METHOD		
	Arithmetic	Geometric	Logarithmic	Geometric	Logarithmic	Description
	μm	μm	ϕ	μm	ϕ	
MEAN ($\bar{x}$):	279,1	246,7	1,993	250,2	1,999	Medium Sand
SORTING (σ):	145,4	1,676	0,631	1,511	0,596	Moderately Well Sorted
SKEWNESS (Sk):	1,952	-2,968	-0,374	0,204	-0,204	Coarse Skewed
KURTOSIS (K):	6,983	36,18	3,841	1,239	1,239	Leptokurtic

GRAIN SIZE DISTRIBUTION

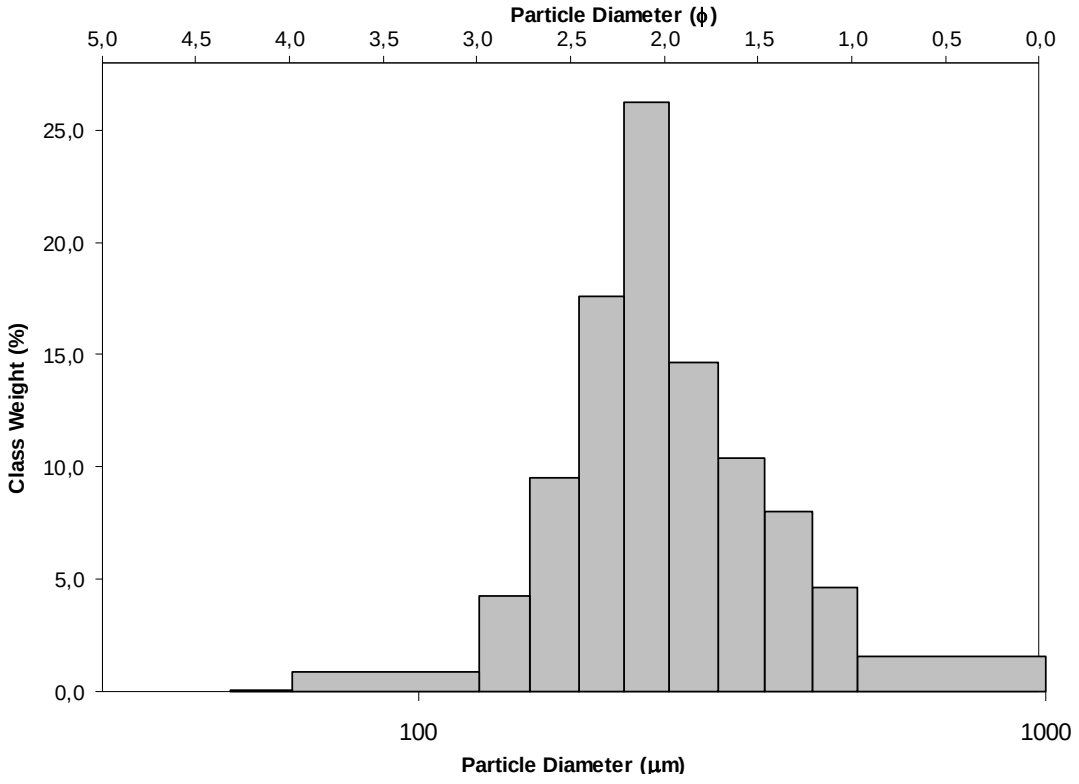

SAMPLE STATISTICS

SAMPLE IDENTITY: **NER10** ANALYST & DATE: Nil, 11/24/2020

SAMPLE TYPE: Unimodal, Moderately Well Sorted TEXTURAL GROUP: Sand

SEDIMENT NAME: Moderately Well Sorted Fine Sand

	μm	ϕ
MODE 1:	165,0	2,605
MODE 2:		
MODE 3:		
D_{10}:	100,8	1,636
MEDIAN or D_{50}:	173,4	2,528
D_{90}:	321,7	3,310
(D_{90} / D_{10}):	3,190	2,023
(D_{90} - D_{10}):	220,8	1,673
(D_{75} / D_{25}):	1,651	1,340
(D_{75} - D_{25}):	90,27	0,723

GRAIN SIZE DISTRIBUTION

GRAVEL:	0,0%	COARSE SAND:	3,7%
SAND:	99,8%	MEDIUM SAND:	14,9%
MUD:	0,2%	FINE SAND:	67,0%
		V FINE SAND:	14,3%
V COARSE GRAVEL:	0,0%	V COARSE SILT:	0,2%
COARSE GRAVEL:	0,0%	COARSE SILT:	0,0%
MEDIUM GRAVEL:	0,0%	MEDIUM SILT:	0,0%
FINE GRAVEL:	0,0%	FINE SILT:	0,0%
V FINE GRAVEL:	0,0%	V FINE SILT:	0,0%
V COARSE SAND:	0,0%	CLAY:	0,0%

	METHOD OF MOMENTS			FOLK & WARD METHOD		
	Arithmetic	Geometric	Logarithmic	Geometric	Logarithmic	Description
	μm	μm	ϕ	μm	ϕ	
MEAN ($\bar{x}$):	193,4	159,6	2,457	180,6	2,469	Fine Sand
SORTING (σ):	108,3	2,287	0,708	1,555	0,637	Moderately Well Sorted
SKEWNESS (Sk):	2,624	-4,229	-0,970	0,117	-0,117	Coarse Skewed
KURTOSIS (K):	13,57	27,29	4,988	1,375	1,375	Leptokurtic

GRAIN SIZE DISTRIBUTION

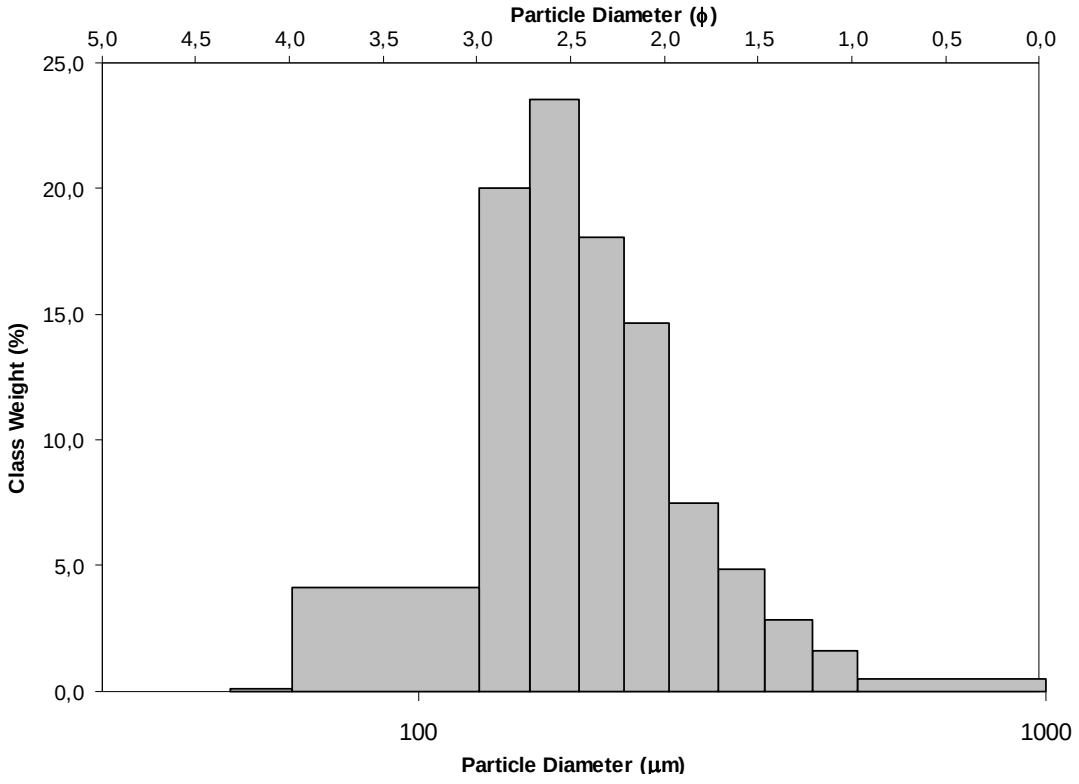

SAMPLE STATISTICS

SAMPLE IDENTITY: **NER40** ANALYST & DATE: Nil, 11/24/2020

SAMPLE TYPE: Bimodal, Well Sorted TEXTURAL GROUP: Sand

SEDIMENT NAME: Well Sorted Medium Sand

	μm	ϕ
MODE 1:	275,0	1,868
MODE 2:	196,0	2,356
MODE 3:		
D_{10}:	157,5	1,451
MEDIAN or D_{50}:	255,8	1,967
D_{90}:	365,9	2,666
(D_{90} / D_{10}):	2,322	1,838
(D_{90} - D_{10}):	208,3	1,216
(D_{75} / D_{25}):	1,514	1,337
(D_{75} - D_{25}):	99,19	0,598

GRAIN SIZE DISTRIBUTION

GRAVEL:	0,0%	COARSE SAND:	2,9%
SAND:	100,0%	MEDIUM SAND:	51,4%
MUD:	0,0%	FINE SAND:	44,1%
		V FINE SAND:	1,6%
V COARSE GRAVEL:	0,0%	V COARSE SILT:	0,0%
COARSE GRAVEL:	0,0%	COARSE SILT:	0,0%
MEDIUM GRAVEL:	0,0%	MEDIUM SILT:	0,0%
FINE GRAVEL:	0,0%	FINE SILT:	0,0%
V FINE GRAVEL:	0,0%	V FINE SILT:	0,0%
V COARSE SAND:	0,0%	CLAY:	0,0%

	METHOD OF MOMENTS			FOLK & WARD METHOD		
	Arithmetic	Geometric	Logarithmic	Geometric	Logarithmic	Description
	μm	μm	ϕ	μm	ϕ	
MEAN ($\bar{x}$):	262,0	240,1	2,026	242,5	2,044	Fine Sand
SORTING (σ):	108,8	1,600	0,521	1,388	0,473	Well Sorted
SKEWNESS (Sk):	2,282	-4,961	-0,338	-0,156	0,156	Fine Skewed
KURTOSIS (K):	11,20	60,92	4,686	1,113	1,113	Leptokurtic

GRAIN SIZE DISTRIBUTION

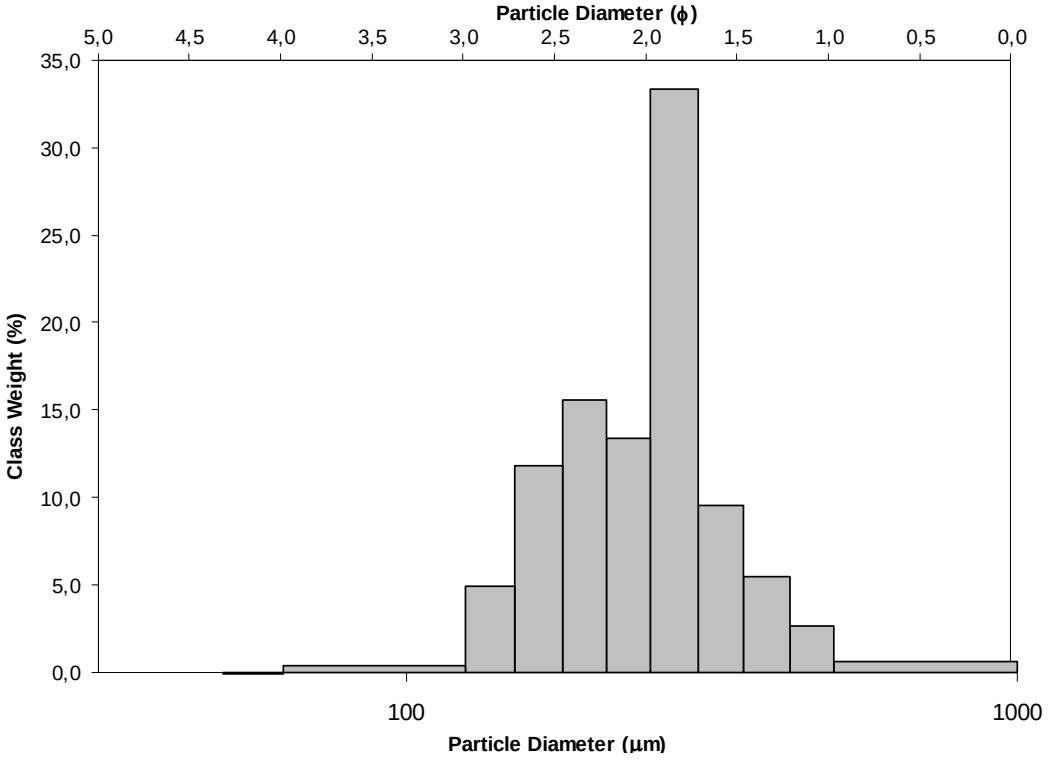

SAMPLE STATISTICS

SAMPLE IDENTITY: **NER30** ANALYST & DATE: Nil, 8/12/2020

SAMPLE TYPE: Unimodal, Moderately Sorted TEXTURAL GROUP: Sand

SEDIMENT NAME: Moderately Sorted Fine Sand

	μm	ϕ
MODE 1:	196,0	2,356
MODE 2:		
MODE 3:		
D_{10}:	155,1	0,962
MEDIAN or D_{50}:	240,0	2,059
D_{90}:	513,3	2,689
(D_{90} / D_{10}):	3,311	2,795
(D_{90} - D_{10}):	358,3	1,727
(D_{75} / D_{25}):	1,724	1,491
(D_{75} - D_{25}):	138,3	0,786

GRAIN SIZE DISTRIBUTION

GRAVEL:	0,0%	COARSE SAND:	10,2%
SAND:	99,4%	MEDIUM SAND:	35,6%
MUD:	0,6%	FINE SAND:	49,8%
		V FINE SAND:	3,8%
V COARSE GRAVEL:	0,0%	V COARSE SILT:	0,6%
COARSE GRAVEL:	0,0%	COARSE SILT:	0,0%
MEDIUM GRAVEL:	0,0%	MEDIUM SILT:	0,0%
FINE GRAVEL:	0,0%	FINE SILT:	0,0%
V FINE GRAVEL:	0,0%	V FINE SILT:	0,0%
V COARSE SAND:	0,0%	CLAY:	0,0%

	METHOD OF MOMENTS			FOLK & WARD METHOD		
	Arithmetic	Geometric	Logarithmic	Geometric	Logarithmic	Description
	μm	μm	ϕ	μm	ϕ	
MEAN ($\bar{x}$):	251,9	173,8	1,935	255,5	1,969	Medium Sand
SORTING (σ):	144,7	3,896	0,778	1,683	0,751	Moderately Sorted
SKEWNESS (Sk):	1,491	-3,142	-0,644	0,307	-0,307	Very Coarse Skewed
KURTOSIS (K):	6,839	12,31	3,990	1,543	1,543	Very Leptokurtic

GRAIN SIZE DISTRIBUTION

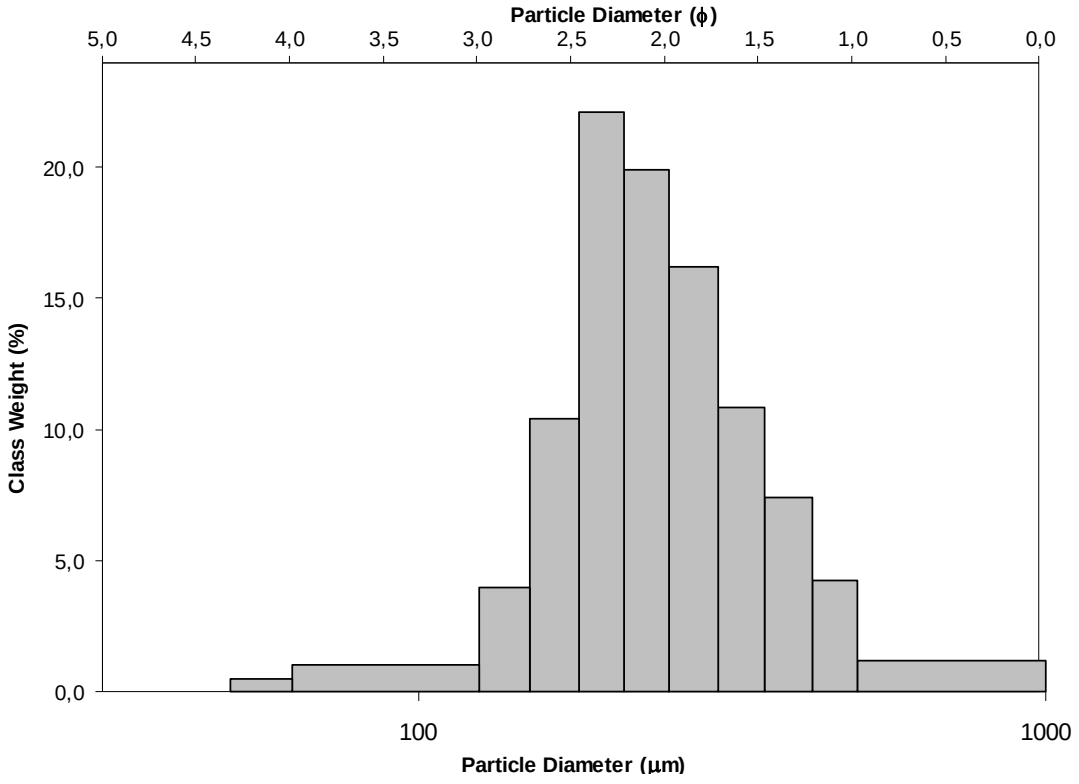

SAMPLE STATISTICS

SAMPLE IDENTITY: **NER39** ANALYST & DATE: Nil, 11/24/2020

SAMPLE TYPE: Unimodal, Moderately Well Sorted TEXTURAL GROUP: Sand

SEDIMENT NAME: Moderately Well Sorted Fine Sand

	μm	ϕ
MODE 1:	275,0	1,868
MODE 2:		
MODE 3:		
D_{10}:	155,1	1,305
MEDIAN or D_{50}:	245,6	2,026
D_{90}:	404,7	2,689
(D_{90} / D_{10}):	2,609	2,060
(D_{90} - D_{10}):	249,6	1,384
(D_{75} / D_{25}):	1,533	1,352
(D_{75} - D_{25}):	103,3	0,616

GRAIN SIZE DISTRIBUTION

GRAVEL:	0,0%	COARSE SAND:	5,7%
SAND:	99,9%	MEDIUM SAND:	42,2%
MUD:	0,1%	FINE SAND:	49,2%
		V FINE SAND:	2,7%
V COARSE GRAVEL:	0,0%	V COARSE SILT:	0,1%
COARSE GRAVEL:	0,0%	COARSE SILT:	0,0%
MEDIUM GRAVEL:	0,0%	MEDIUM SILT:	0,0%
FINE GRAVEL:	0,0%	FINE SILT:	0,0%
V FINE GRAVEL:	0,0%	V FINE SILT:	0,0%
V COARSE SAND:	0,0%	CLAY:	0,0%

	METHOD OF MOMENTS			FOLK & WARD METHOD		
	Arithmetic μm	Geometric μm	Logarithmic ϕ	Geometric μm	Logarithmic ϕ	Description
MEAN ($\bar{x}$):	272,2	241,7	2,009	244,1	2,034	Fine Sand
SORTING (σ):	136,7	1,708	0,603	1,469	0,555	Moderately Well Sorted
SKEWNESS (Sk):	2,150	-4,044	-0,417	0,059	-0,059	Symmetrical
KURTOSIS (K):	8,286	45,18	4,357	1,345	1,345	Leptokurtic

GRAIN SIZE DISTRIBUTION

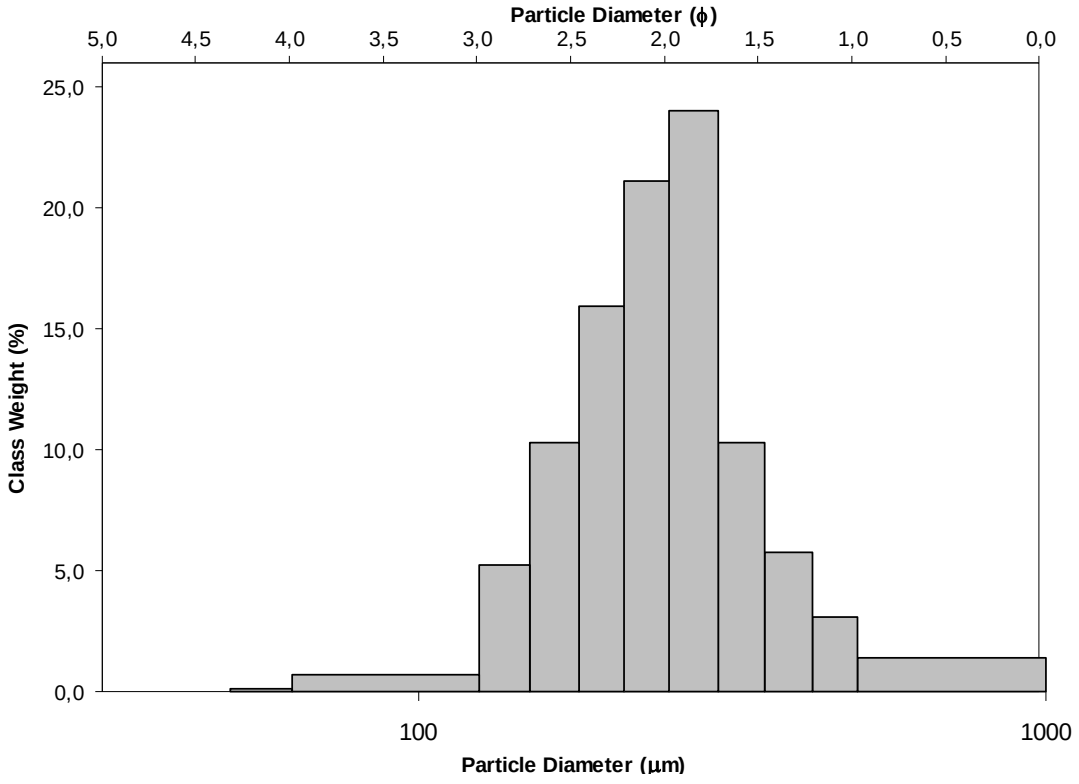

SAMPLE STATISTICS

SAMPLE IDENTITY: **NER28** ANALYST & DATE: Nil, 11/24/2020

SAMPLE TYPE: Unimodal, Moderately Sorted TEXTURAL GROUP: Sand

SEDIMENT NAME: Moderately Sorted Fine Sand

	μm	ϕ
MODE 1:	231,0	2,119
MODE 2:		
MODE 3:		
D_{10}:	135,7	1,027
MEDIAN or D_{50}:	231,2	2,113
D_{90}:	490,8	2,881
(D_{90} / D_{10}):	3,616	2,806
(D_{90} - D_{10}):	355,1	1,855
(D_{75} / D_{25}):	1,901	1,581
(D_{75} - D_{25}):	157,0	0,927

GRAIN SIZE DISTRIBUTION

GRAVEL:	0,0%	COARSE SAND:	9,5%
SAND:	99,1%	MEDIUM SAND:	32,7%
MUD:	0,9%	FINE SAND:	51,1%
		V FINE SAND:	5,9%
V COARSE GRAVEL:	0,0%	V COARSE SILT:	0,9%
COARSE GRAVEL:	0,0%	COARSE SILT:	0,0%
MEDIUM GRAVEL:	0,0%	MEDIUM SILT:	0,0%
FINE GRAVEL:	0,0%	FINE SILT:	0,0%
V FINE GRAVEL:	0,0%	V FINE SILT:	0,0%
V COARSE SAND:	0,0%	CLAY:	0,0%

	METHOD OF MOMENTS			FOLK & WARD METHOD		
	Arithmetic	Geometric	Logarithmic	Geometric	Logarithmic	Description
	μm	μm	ϕ	μm	ϕ	
MEAN ($\bar{x}$):	272,4	215,4	2,032	243,2	2,040	Fine Sand
SORTING (σ):	167,2	2,447	0,787	1,721	0,783	Moderately Sorted
SKEWNESS (Sk):	1,622	-3,837	-0,313	0,169	-0,169	Coarse Skewed
KURTOSIS (K):	5,487	24,27	3,338	1,273	1,273	Leptokurtic

GRAIN SIZE DISTRIBUTION

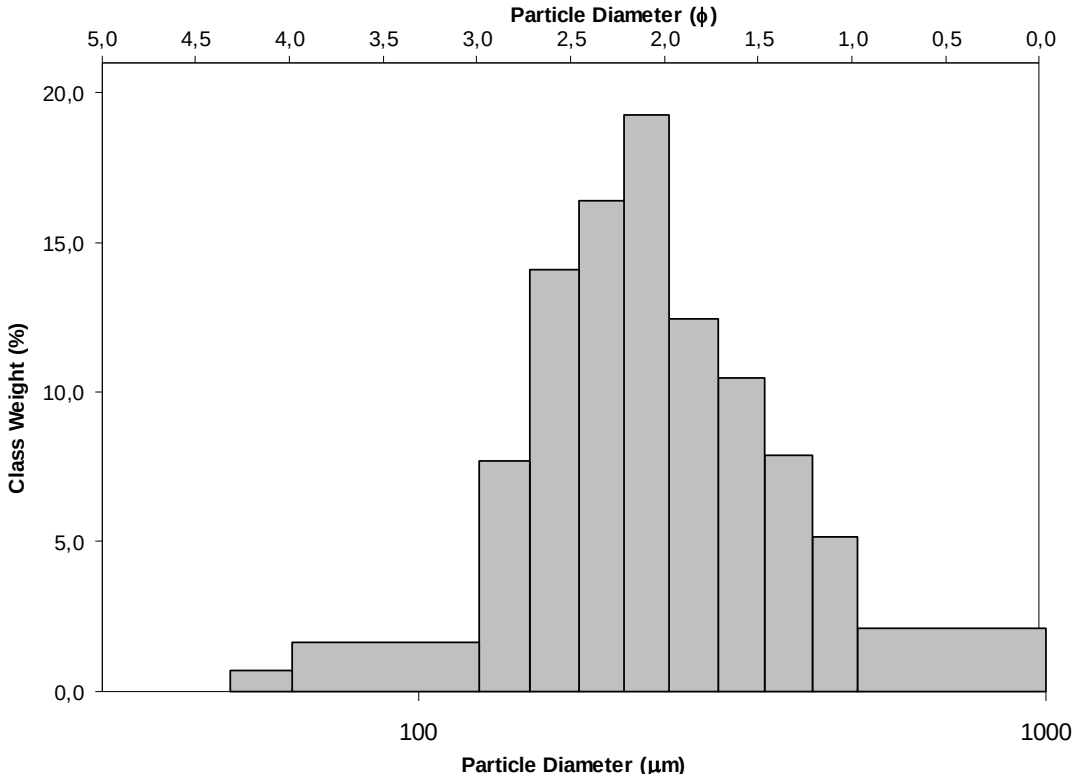

SAMPLE STATISTICS

SAMPLE IDENTITY: **NER16** ANALYST & DATE: Nil, 8/12/2020

SAMPLE TYPE: Unimodal, Moderately Well Sorted TEXTURAL GROUP: Sand

SEDIMENT NAME: Moderately Well Sorted Fine Sand

	μm	ϕ
MODE 1:	196,0	2,356
MODE 2:		
MODE 3:		
D_{10}:	124,0	1,723
MEDIAN or D_{50}:	191,2	2,387
D_{90}:	303,0	3,012
(D_{90} / D_{10}):	2,444	1,748
(D_{90} - D_{10}):	179,0	1,289
(D_{75} / D_{25}):	1,496	1,276
(D_{75} - D_{25}):	77,15	0,581

GRAIN SIZE DISTRIBUTION

GRAVEL:	0,0%	COARSE SAND:	2,1%
SAND:	98,3%	MEDIUM SAND:	16,7%
MUD:	1,7%	FINE SAND:	71,1%
		V FINE SAND:	8,4%
V COARSE GRAVEL:	0,0%	V COARSE SILT:	1,7%
COARSE GRAVEL:	0,0%	COARSE SILT:	0,0%
MEDIUM GRAVEL:	0,0%	MEDIUM SILT:	0,0%
FINE GRAVEL:	0,0%	FINE SILT:	0,0%
V FINE GRAVEL:	0,0%	V FINE SILT:	0,0%
V COARSE SAND:	0,0%	CLAY:	0,0%

	METHOD OF MOMENTS			FOLK & WARD METHOD		
	Arithmetic	Geometric	Logarithmic	Geometric	Logarithmic	Description
	μm	μm	ϕ	μm	ϕ	
MEAN ($\bar{x}$):	207,2	185,2	2,399	191,2	2,387	Fine Sand
SORTING (σ):	102,1	1,674	0,616	1,481	0,567	Moderately Well Sorted
SKEWNESS (Sk):	2,835	-3,468	-0,160	-0,060	0,060	Symmetrical
KURTOSIS (K):	15,29	37,80	5,022	1,535	1,535	Very Leptokurtic

GRAIN SIZE DISTRIBUTION

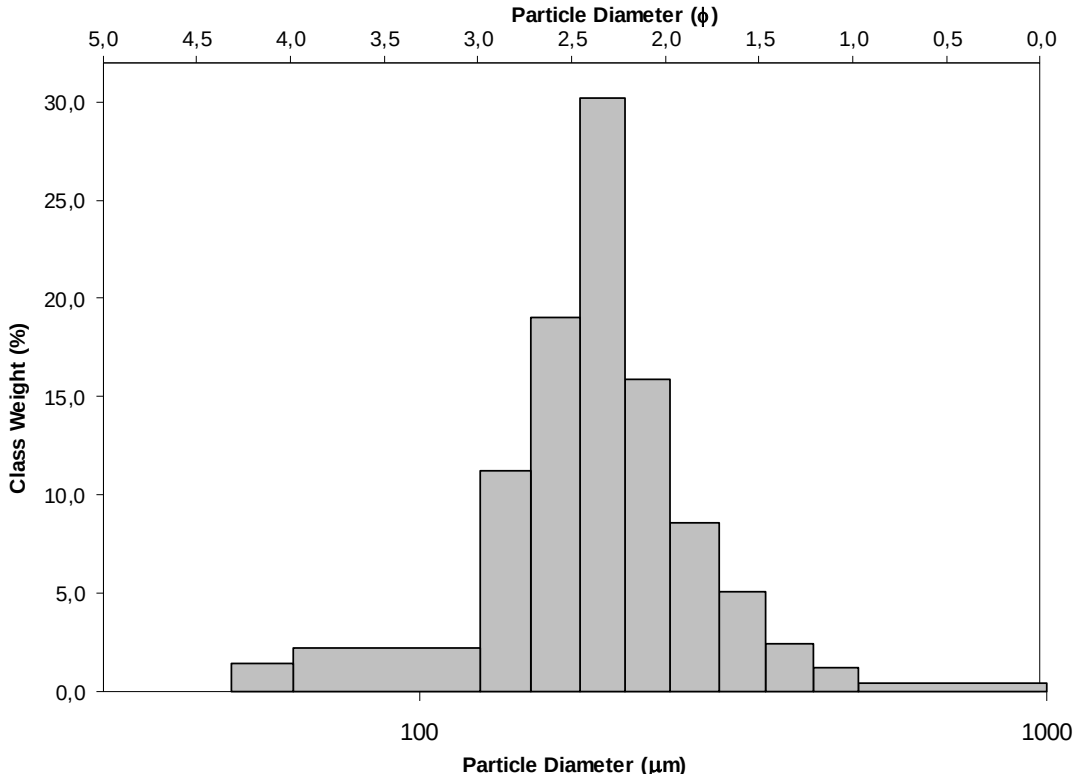

SAMPLE STATISTICS

SAMPLE IDENTITY: **NER19** ANALYST & DATE: Nil, 11/24/2020

SAMPLE TYPE: Bimodal, Moderately Well Sorted TEXTURAL GROUP: Sand

SEDIMENT NAME: Moderately Well Sorted Fine Sand

	μm	ϕ
MODE 1:	165,0	2,605
MODE 2:	275,0	1,868
MODE 3:		
D_{10}:	113,3	1,656
MEDIAN or D_{50}:	185,8	2,428
D_{90}:	317,3	3,142
(D_{90} / D_{10}):	2,801	1,897
(D_{90} - D_{10}):	204,0	1,486
(D_{75} / D_{25}):	1,656	1,365
(D_{75} - D_{25}):	99,55	0,728

GRAIN SIZE DISTRIBUTION

GRAVEL:	0,0%	COARSE SAND:	1,8%
SAND:	99,5%	MEDIUM SAND:	23,5%
MUD:	0,5%	FINE SAND:	63,0%
		V FINE SAND:	11,0%
V COARSE GRAVEL:	0,0%	V COARSE SILT:	0,5%
COARSE GRAVEL:	0,0%	COARSE SILT:	0,0%
MEDIUM GRAVEL:	0,0%	MEDIUM SILT:	0,0%
FINE GRAVEL:	0,0%	FINE SILT:	0,0%
V FINE GRAVEL:	0,0%	V FINE SILT:	0,0%
V COARSE SAND:	0,0%	CLAY:	0,0%

	METHOD OF MOMENTS			FOLK & WARD METHOD		
	Arithmetic	Geometric	Logarithmic	Geometric	Logarithmic	Description
	μm	μm	ϕ	μm	ϕ	
MEAN ($\bar{x}$):	210,5	187,6	2,391	191,5	2,385	Fine Sand
SORTING (σ):	104,8	1,644	0,631	1,526	0,610	Moderately Well Sorted
SKEWNESS (Sk):	2,448	-2,492	-0,242	0,042	-0,042	Symmetrical
KURTOSIS (K):	12,52	29,89	3,875	1,262	1,262	Leptokurtic

GRAIN SIZE DISTRIBUTION

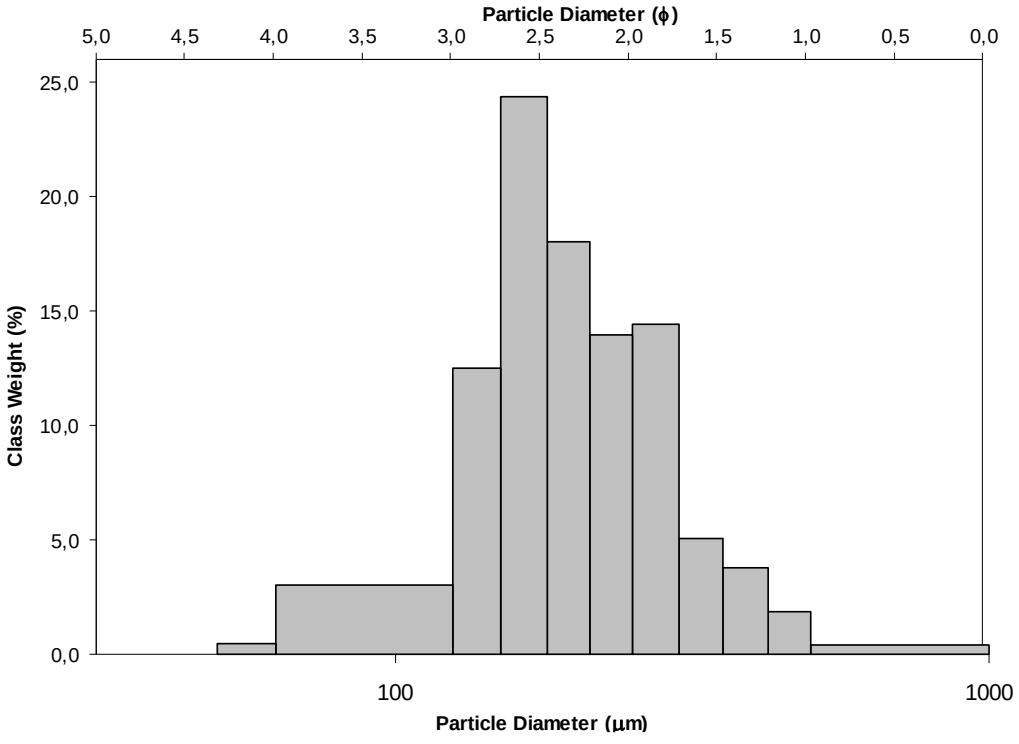

SAMPLE STATISTICS

SAMPLE IDENTITY: **NER25** ANALYST & DATE: Nil, 8/12/2020

SAMPLE TYPE: Unimodal, Moderately Well Sorted TEXTURAL GROUP: Sand

SEDIMENT NAME: Moderately Well Sorted Fine Sand

	μm	ϕ
MODE 1:	196,0	2,356
MODE 2:		
MODE 3:		
D_{10}:	125,5	1,815
MEDIAN or D_{50}:	191,4	2,385
D_{90}:	284,3	2,995
(D_{90} / D_{10}):	2,266	1,650
(D_{90} - D_{10}):	158,8	1,180
(D_{75} / D_{25}):	1,400	1,224
(D_{75} - D_{25}):	63,79	0,486

GRAIN SIZE DISTRIBUTION

GRAVEL:	0,0%	COARSE SAND:	2,1%
SAND:	99,7%	MEDIUM SAND:	12,6%
MUD:	0,3%	FINE SAND:	75,5%
		V FINE SAND:	9,6%
V COARSE GRAVEL:	0,0%	V COARSE SILT:	0,3%
COARSE GRAVEL:	0,0%	COARSE SILT:	0,0%
MEDIUM GRAVEL:	0,0%	MEDIUM SILT:	0,0%
FINE GRAVEL:	0,0%	FINE SILT:	0,0%
V FINE GRAVEL:	0,0%	V FINE SILT:	0,0%
V COARSE SAND:	0,0%	CLAY:	0,0%

	METHOD OF MOMENTS			FOLK & WARD METHOD		
	Arithmetic	Geometric	Logarithmic	Geometric	Logarithmic	Description
	μm	μm	ϕ	μm	ϕ	
MEAN ($\bar{x}$):	207,4	188,8	2,399	188,6	2,407	Fine Sand
SORTING (σ):	102,2	1,505	0,564	1,427	0,513	Moderately Well Sorted
SKEWNESS (Sk):	3,242	-0,869	-0,412	-0,078	0,078	Symmetrical
KURTOSIS (K):	17,10	19,81	5,203	1,749	1,749	Very Leptokurtic

GRAIN SIZE DISTRIBUTION

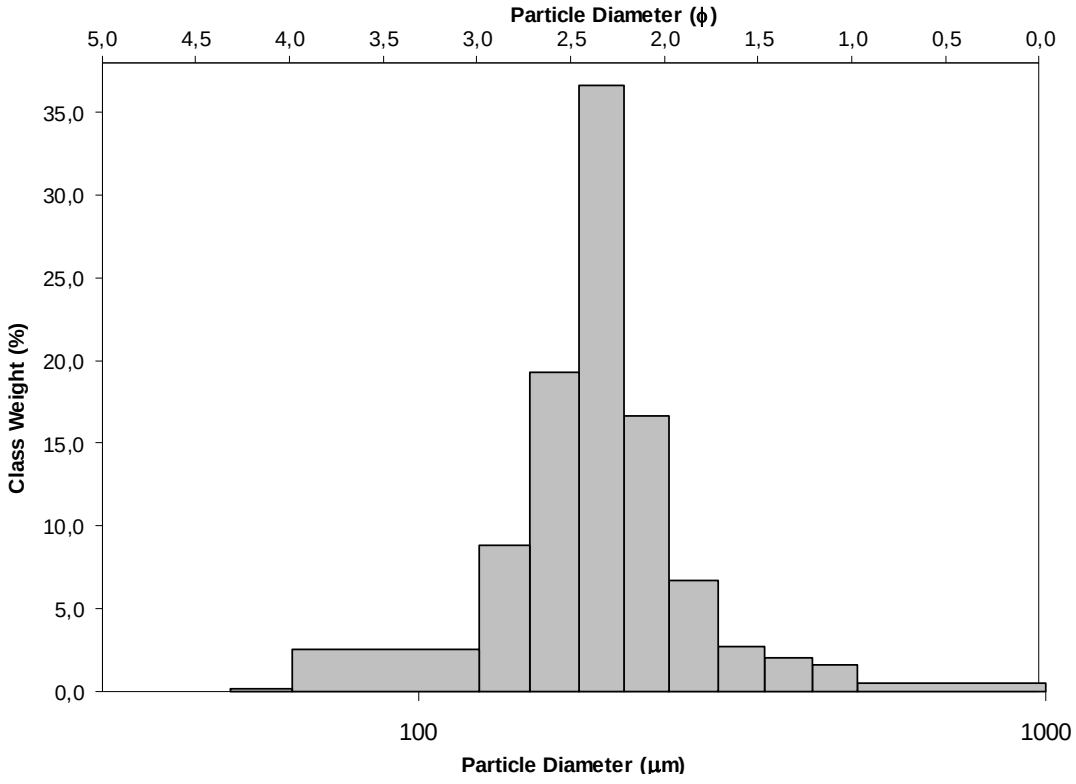

SAMPLE STATISTICS

SAMPLE IDENTITY: **NER21** ANALYST & DATE: Nil, 8/12/2020

SAMPLE TYPE: Unimodal, Moderately Well Sorted TEXTURAL GROUP: Sand

SEDIMENT NAME: Moderately Well Sorted Fine Sand

	μm	ϕ
MODE 1:	196,0	2,356
MODE 2:		
MODE 3:		
D_{10}:	106,5	1,566
MEDIAN or D_{50}:	186,2	2,425
D_{90}:	337,8	3,231
(D_{90} / D_{10}):	3,172	2,064
(D_{90} - D_{10}):	231,3	1,665
(D_{75} / D_{25}):	1,601	1,326
(D_{75} - D_{25}):	88,73	0,679

GRAIN SIZE DISTRIBUTION

GRAVEL:	0,0%	COARSE SAND:	3,2%
SAND:	99,6%	MEDIUM SAND:	16,8%
MUD:	0,4%	FINE SAND:	67,0%
		V FINE SAND:	12,5%
V COARSE GRAVEL:	0,0%	V COARSE SILT:	0,4%
COARSE GRAVEL:	0,0%	COARSE SILT:	0,0%
MEDIUM GRAVEL:	0,0%	MEDIUM SILT:	0,0%
FINE GRAVEL:	0,0%	FINE SILT:	0,0%
V FINE GRAVEL:	0,0%	V FINE SILT:	0,0%
V COARSE SAND:	0,0%	CLAY:	0,0%

	METHOD OF MOMENTS			FOLK & WARD METHOD		
	Arithmetic	Geometric	Logarithmic	Geometric	Logarithmic	Description
	μm	μm	ϕ	μm	ϕ	
MEAN ($\bar{x}$):	213,2	186,2	2,402	188,9	2,404	Fine Sand
SORTING (σ):	122,7	1,685	0,671	1,556	0,638	Moderately Well Sorted
SKEWNESS (Sk):	2,629	-1,947	-0,502	0,031	-0,031	Symmetrical
KURTOSIS (K):	11,60	25,33	4,006	1,457	1,457	Leptokurtic

GRAIN SIZE DISTRIBUTION

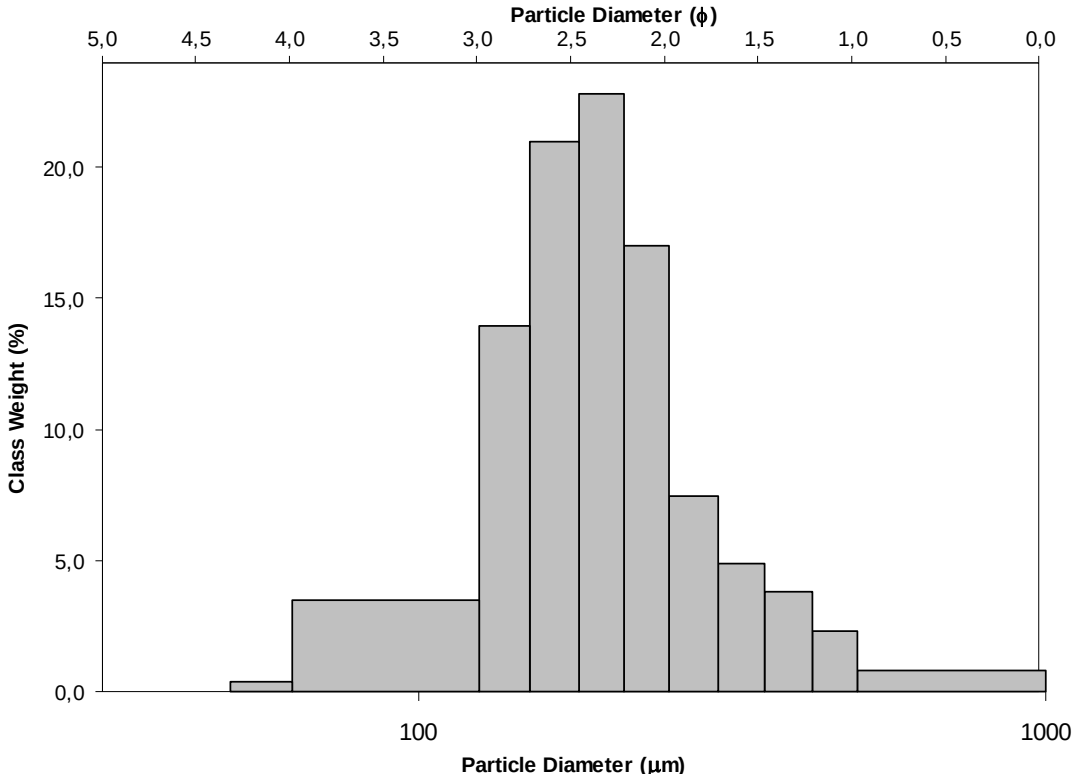

SAMPLE STATISTICS

SAMPLE IDENTITY: **NER24**

ANALYST & DATE: Nil, 11/24/2020

SAMPLE TYPE: Bimodal, Well Sorted

TEXTURAL GROUP: Sand

SEDIMENT NAME: Well Sorted Fine Sand

	μm	ϕ
MODE 1:	165,0	2,605
MODE 2:	275,0	1,868
MODE 3:		
D_{10}:	133,8	1,826
MEDIAN or D_{50}:	185,2	2,433
D_{90}:	282,0	2,902
(D_{90} / D_{10}):	2,108	1,589
(D_{90} - D_{10}):	148,2	1,076
(D_{75} / D_{25}):	1,500	1,281
(D_{75} - D_{25}):	78,89	0,585

GRAIN SIZE DISTRIBUTION

GRAVEL:	0,0%	COARSE SAND:	1,5%
SAND:	99,8%	MEDIUM SAND:	18,8%
MUD:	0,2%	FINE SAND:	73,6%
		V FINE SAND:	5,9%
V COARSE GRAVEL:	0,0%	V COARSE SILT:	0,2%
COARSE GRAVEL:	0,0%	COARSE SILT:	0,0%
MEDIUM GRAVEL:	0,0%	MEDIUM SILT:	0,0%
FINE GRAVEL:	0,0%	FINE SILT:	0,0%
V FINE GRAVEL:	0,0%	V FINE SILT:	0,0%
V COARSE SAND:	0,0%	CLAY:	0,0%

	METHOD OF MOMENTS			FOLK & WARD METHOD		
	Arithmetic	Geometric	Logarithmic	Geometric	Logarithmic	Description
	μm	μm	ϕ	μm	ϕ	
MEAN ($\bar{x}$):	205,1	190,3	2,389	193,2	2,371	Fine Sand
SORTING (σ):	89,16	1,445	0,504	1,342	0,424	Well Sorted
SKEWNESS (Sk):	3,499	-1,231	-0,442	0,092	-0,092	Symmetrical
KURTOSIS (K):	21,44	26,94	5,606	1,004	1,004	Mesokurtic

GRAIN SIZE DISTRIBUTION